A STUDY OF MESOSCALE ATMOSPHERIC CIRCULATIONS INDUCED BY LAND SURFACE HETEROGENEITY

by

JINGFENG WANG

BS, Peking University, China (1984)
MS, Peking University, China (1987)

Submitted to the Department of Civil and Environmental Engineering
in partial fulfillment of the requirements for the degree of

DOCTOR OF SCIENCE

at the

MASSACHUSETTS INSTITUTE OF TECHNOLOGY

February 1997

Author .....
Department of Civil and Environmental Engineering
January 17, 1997

Certified by .....
Rafael L. Bras, Bacardi and Stockholm Water Foundations Professor
Thesis Supervisor

Certified by .....
Elfatih A. B. Eltahir, Assistant Professor
Thesis Co-Supervisor

Accepted by .....
Professor Joseph M. Sussman
Chairman, Departmental Committee on Graduate Students

A STUDY OF MESOSCALE ATMOSPHERIC CIRCULATIONS INDUCED BY LAND SURFACE HETEROGENEITY

by

JINGFENG WANG

Submitted to the Department of Civil and Environmental Engineering
on January 17, 1997, in partial fulfillment of the
requirements for the degree of
DOCTOR OF SCIENCE

Abstract

Mesoscale circulations induced by complex land surface have been investigated using linear stochastic models and a nonlinear numerical model. Random distributions of differential surface heating and variable topography are described in terms of homogeneous random fields. Analytical solutions for the linear atmospheric systems under these random surface forcings have been obtained. The stochastic linear theory suggests that thermally induced flow is strongly inhibited in an environment of stable stratification and moderate synoptic wind. Numerical experiments indicate that mesoscale momentum fluxes are more important than turbulent fluxes and mesoscale heat fluxes are not significant in the thermally induced flow. The stochastic linear theory also shows that mountain waves over random topography are effective in inducing momentum fluxes, but not effective in inducing heat fluxes.

Thesis Supervisor: Rafael L. Bras
Title: Bacardi and Stockholm Water Foundations Professor

Thesis Co-Supervisor: Elfatih A. B. Eltahir
Title: Assistant Professor

To my parents

Acknowledgments

This work was supported by the National Science Foundation under grants EAR-9120386 and ATM-9020832. Our simulations were carried out on CRAY Y-MP8/864 machine at NCAR. We gratefully acknowledge NCAR's support of this project. Special thanks go to CLARK modelers, particularly to Ms. Janice Coen for her invaluable advice and constant assistance through out this work. We are grateful to Dr. Jeff Eidenshink who generously provided the software for processing the NDVI data.

I was so fortunate to work with Professor Rafael L. Bras, my major advisor, who provided me with precious financial and spiritual support during my stay at MIT. His constant inspiration and encouragement made this thesis possible. His praise, criticism and guidance will benefit my future career for many years to come.

I am indebted to Professor Elfatih A. B. Eltahir, my co-advisor, from whom I have learned so much about how to achieve excellence in research through our close interactions. Thanks are also due to my thesis committee members, Professors Dara Entekhabi and Daniele Veneziano for their insightful comments on each and every step that kept me on the right track. Working with them has been truly a pleasant and rewarding experience.

It is a great pleasure to express my appreciation to the assistance provided by my friend Huanzhang Luo, a talented mathematician who won a gold medal in the International Mathematics Olympic. His expertise made an important contribution to the derivation of the analytical solution presented in chapter 3. There is a list of people too long to name here who also provided invaluable assistance at different stages of my thesis work. I wish to thank all of them.

I would like express my gratitude to all my friends and colleagues in Parsons Lab. They all make Parsons a enjoyable place to work. Particularly, Elaine Healy and Pat Dixon deserve special thanks for their warmness to every Parsons family member. They made my student life at MIT much easier. I do not hesitate to say that these five years have been the happiest in my life.

My limited English does not allow me to fully express my deepest gratitude to the unselfish love and faithful support of my parents. They have been the steadfast source of my

strength during my life-long journey of pursuing higher goals. Any success I have achieved and will possibly achieve is theirs.

Contents

List of Figures

List of Tables

Chapter 1

Introduction

Complexity in atmospheric circulation at mesoscales results to a large extend from complexity in the surface forcing provided by differential heating or variable topography. Satisfactory prediction of mesoscale circulation critically relies on the realistic description of the surface forcings. Currently, a wide gap exists between the assumed land surface variability in the existing mesoscale circulation models and the observed variability of land surface in the nature.

The strength of the surface forcing is represented by the gradient of the spatial distributions of turbulent heat fluxes at the ground and topographic height. In the case of simple patterns, such as sharp contrast between land and water in coastal regions, observations have shown that the thermal gradient provides a strong thermal forcing leading to sea breezes, a typical example of mesoscale circulation. On the other hand, such a simple surface heating pattern is less common over continental regions where the thermal heterogeneity of the land surface is due to variable vegetation cover, soil properties and/or soil moisture distribution. Natural landscapes most often exhibit irregular or random patterns of the thermal properties. The gradual change of the thermal properties of land surface leads to a smaller gradient, hence a weaker thermal forcing of the atmosphere.

Isolated bell-shape mountains or continuous sinusoidal ridges are believed capable of causing gravity waves, another type of mesoscale circulation, when large scale airflows occur over these barriers. Such a simple topography, though, has never been encountered. Natural

terrain is usually covered by many adjacent mountains of irregular shapes with a wide range of scales and heights. Consequently, the deterministic description of this kind of complex topography is not sufficient to characterize the topographical forcing of the atmosphere.

Early efforts to understand the roles of differential heating and variable topography assumed over-simplified patterns of the surface forcing (e.g. Haurwitz 1947, Schemidt 1947, Defant 1950, Lyra 1940, Queney 1941, Scorer 1949). One of the main conclusions from these works was that the length scales of differential heating and topographic barrier are important in determining the fundamental behavior of the land surface heterogeneity induced mesoscale circulation.

In recent years, there has been increasing interest in the characterization of the impact of variability of land surface on the dynamics of the mesoscale circulation and the associated energy and mass transport in large-scale atmospheric models. Theoretical approaches for the thermally induced flow, e.g. Rotunno (1983), Dalu & Piekle (1989), Dalu et al. (1991), and numerical simulations, e.g. Avissar & Pielke (1989) and Avissar & Chen (1993) have suggested that the intensity of the mesoscale circulation induced by the thermal heterogeneity of the land surface could be as strong as the sea breeze and that the associated mesoscale heat flux can be as large as the turbulent heat flux. Hence mesoscale circulations could contribute significantly to the vertical transport of energy. Studies on topography induced flow have also revealed rich phenomena resulting from the mesoscale circulations caused by large scale airflow over mountain barriers (e.g. Atkinson 1981). This topographically induced mesoscale flow (frequently referred to as *mountain waves* in literature) is responsible for a number of atmospheric processes such as wave drag or vertical transport of horizontal momentum (Eliassen & Palm 1960, Blumen 1965a, Blumen 1965b, Bretherton 1969, Smith 1978, etc.). Therefore, both thermally induced flow and topographically induced flow have potentially important impact on the performance of large scale models.

The objective of this work is to bridge the gap between the over-simplified patterns of assumed land surface conditions in mesoscale models and the complex distributions of natural landscape by investigating the impact of differential heating and topography of random distribution on the mesoscale circulations. The basic idea is to adopt random functions

to describe the complex land surface properties. The statistical parameters of the random functions characterizing the complex land surface can be estimated from high resolution observations such as vegetation index and topographical maps.

The stochastic linear models are first used. The purpose of linear analysis is to derive analytical solutions linking the random surface forcing to the random wind field, pressure and temperature variables. Once the analytical solutions are obtained, the analysis of the effect of those parameters characterizing the variability and length scale of the surface forcing and synoptic environment on the mesoscale circulation and mesoscale fluxes is facilitated. The first step in the linear analysis is to formulate three-dimensional linearized dynamic systems for the atmosphere, that include the effects of uniform synoptic wind and stability, in terms of stochastic partial differential equations. The mesoscale flow systems are driven by either diabatic heating due to turbulent sensible heat flux or variable topographic height. The complex spatial distributions of sensible heat flux and topography over land surface are expressed in terms of 2D homogeneous random fields. Wind velocity components, pressure, temperature and moisture content vary randomly in space in response to these random surface forcings. These dependent variables can then also be modeled as homogeneous random fields. Spectral representations of homogeneous random fields will relate all random variables in the physical domain to the corresponding frequency domain where the analytical solutions are sought. Finally, the temporal and vertical distributions of the mesoscale circulation and the mesoscale fluxes are obtained using the analytical solutions of the stochastic partial differential equations relating the wind velocities, pressure, temperature and moisture content to the random surface forcing.

Nonlinear analysis of thermally induced flows are also conducted using numerical simulations. A general analytical approach for nonlinear analysis is not currently available. The accuracy of the linear theories in describing mesoscale circulation depends critically on relative magnitudes and the importance of omitted nonlinear components of the mesoscale systems. Previous research has suggested that nonlinear effects are important in mesoscale circulations.

The structure of the thesis follows this order. Chapter 2 gives quantitative descriptions

of natural land surface heterogeneity. Chapter 3 presents the stochastic linear theory for the thermally induced mesoscale circulation. Chapter 4 addresses the same issue but using a nonlinear numerical model. Chapter 5 is devoted to the stochastic linear model of topographically induced mesoscale circulation. The general conclusions will be highlighted in Chapter 6. A plan for the possible future research will also be given in Chapter 6.

All detailed mathematical derivations are put into the appendices to make this manuscript readable.

Chapter 2

Natural Variability of Land Surface

2.1 Thermal Variability of Land Surface

Thermal properties of land surface are commonly quantified by either surface temperature or surface sensible heat flux. Dry convection in the atmosphere is forced by the diabatic heating resulting from the *turbulent sensible heat flux* (**TSHF**) emitted from land surface. In this thesis work, the thermal variability of land surface refers to the spatial distribution of **TSHF**.

TSHF at land surface comes from the repartitioning of net solar radiation absorbed by the earth. Soil moisture, soil type, and canopy coverage play important roles in the energy balance of the land surface. In nature, these three things could vary significantly over a variety of scales, leading to spatial variation of **TSHF** over the land surface.

Several field experiments provide useful information about the spatial distribution of **TSHF** over mesoscale domains. In the region of *California Ozone Deposition Experiment* where the land was covered by crops and bare soil, more than 200 W m^{-2} difference in **TSHF** over a distance on the order of 10 km was evident from aircraft measurements (Sun & Mahrt, 1994). Satellite images (from 1KM AVHRR) of this region reveal the existence of similar land surface heterogeneity over a much larger surrounding area. At the site of the *Boardman Regional Flux Experiment* near Boardman, Oregon, where the experiment domain consists of mixed steppe and irrigated farm areas of irregular shapes, some 300 W m^{-2} variation in

TSHF with length scales of 10 km or more was documented by Doran et al (1995). Field data collected from HAPEX-MOBILHY (André et al, 1990) give an estimation of difference in **TSHF** of around 100 W m^{-2} across 30 km due to variation of canopy (Mahrt & Ek, 1993). Significant variability of **TSHF** has also been observed within the relatively small experiment area at the FIFE site (e.g. Desjardings et al, 1992).

However, these projects did not provide two-dimensional distribution of **TSHF** with sufficient spatial resolution and coverage suitable for the work conducted here. Direct measurement of **TSHF** over large areas with adequate space and time resolution requires high frequency sampling of temperature and vertical velocity profiles for a large number of locations within the region of interest. This direct measurement is difficult to obtain. As an alternative, a great deal of effort has been devoted to link **TSHF** to certain measured variables of the land surface and standard meteorological observations. For example, many empirical studies have shown that **TSHF** is closely related to the vegetation coverage and soil wetness. In this work vegetation index is selected as a proxy for **TSHF**.

2.1.1 Spatial Distribution of NDVI

NDVI, the *normalized difference of vegetation index*, is defined as the difference of the reflectance at the near-infrared region and visible region divided by the sum of the two

$$\mathrm{NDVI} = \frac{\mathrm{NIR} - \mathrm{VIS}}{\mathrm{NIR} + \mathrm{VIS}} \tag{2.1}$$

where NIR and VIS are near-infrared and visible reflectance, respectively. It characterizes greenness or biomass of the vegetation cover. The biomass in the canopy affects the energy balance at the surface-atmosphere interface through the evapotranspiration of plants. Previous studies (e.g. Sun & Mahrt, 1994) have shown that **NDVI** is highly correlated with the **TSHF** at the surface. Therefore, a linear regression relation can be established to estimate the variability and length scale of the **TSHF** based on **NDVI** measurements.

Data

The **NDVI** data used in this study was from the 1-kilometer advanced very high resolution radiometer (AVHRR) data acquired by the National Oceanic and Atmospheric Administration's (NOAA) Television Infrared Observation Satellite (TIROS). The **NDVI** is computed as the difference of channel 2 (near-infrared, 0.725 - 1.10 μm) and channel 1 (visible, 0.58 - 0.68 μm) reflectance values normalized over the sum of channels 1 and 2 (Eq. 2.1) with global coverage. The **NDVI** equation produces values in the range of -1.0 to 1.0, where increasing positive values indicate increasing green vegetation and negative values indicate non-vegetated surface features such as water, bare soil, and snow or clouds. The composite period is ten days. Figure 2-1 is an example of the spatial distribution of **NDVI** over a region in the US from 1km AVHRR observations.

NDVI data for four regions were initially selected:

1. **Rodonia Amazon** enclosed by (9.5S, 10.5S) and (62.5W, 61.5W).
2. **Central Amazon** enclosed by (3.7S, 4.9S) and (66.7W, 65.0W).
3. **Central US** enclosed by (38.8N, 40.0N) and (67.5W, 65.0W).
4. **Northern US** enclosed by (43.5N, 45.0N) and (105.7W, 104.0W).

A number of factors can affect the accuracy of the **NDVI** observations, hence the estimated statistics of the corresponding spatial distribution. Four principal atmospheric factors, water vapor, aerosols, ozone, and Rayleigh scattering, are considered to have the most impact. The effects of ozone and Rayleigh scattering have been corrected in the final AVHRR products used in this study, while the effects of water vapor and aerosol are not corrected due to lack of appropriate method. The basic problem is determination of the spatial and temporal variability of water vapor and aerosol concentrations.

Another important source of contamination in the **NDVI** observations comes from the presence of clouds. Identifying the types of surfaces (water, soil, vegetation, and cloud) based on **NDVI** criterion (e.g. Flasse and Verstraete 1994) is useful in evaluating the possible contamination of the estimated **NDVI** due to the presence of clouds. It has been

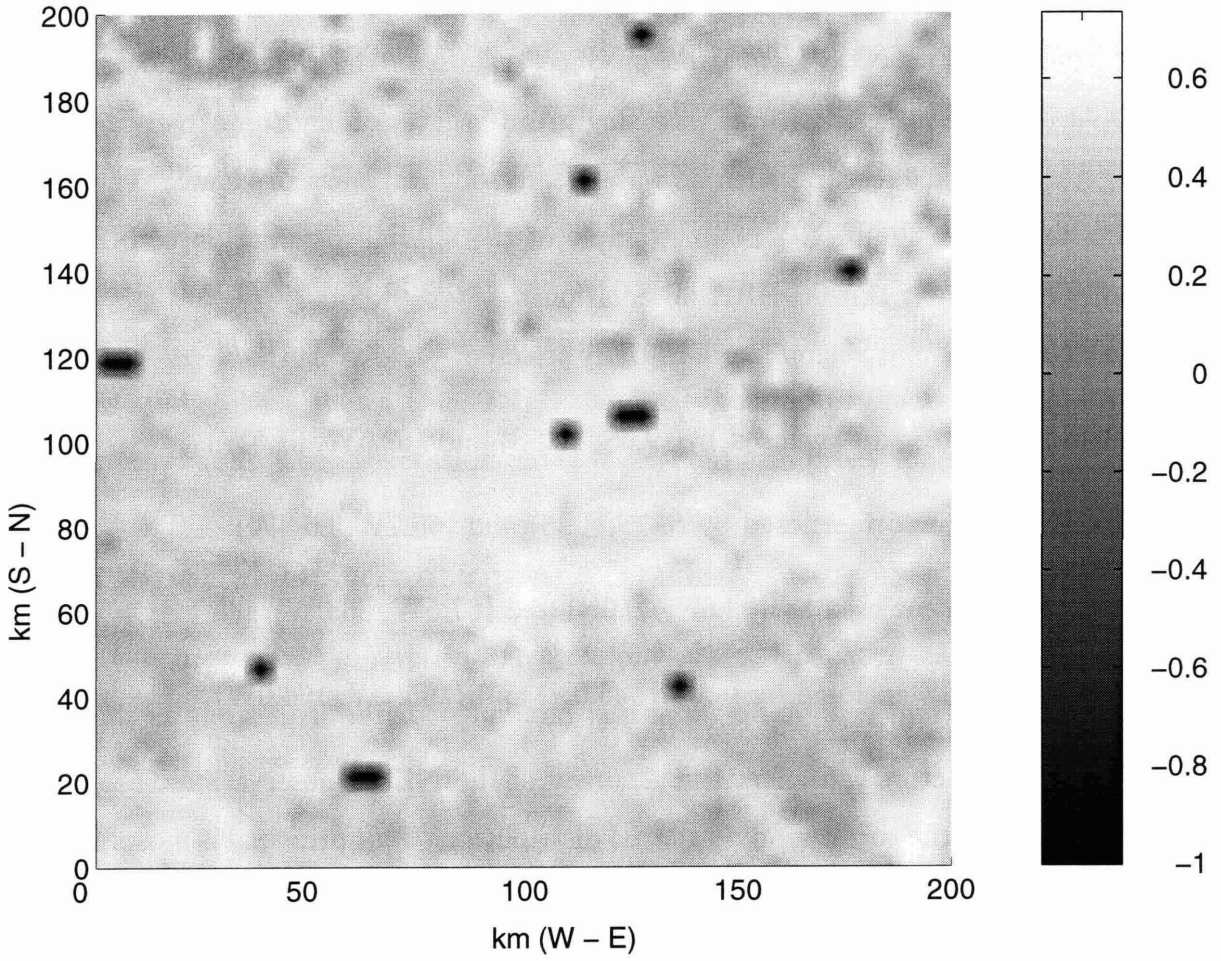

Figure 2-1: Vegetation index (**NDVI**) over central US (composite data of July 1 - 10, 1992) from 1KM AVRHH satellite observations. The image domain is centered at 37.3°N, 98.6°W.

shown that a value of **NDVI** close to 0 represents clouds, small but positive values ($\sim$ 0.0 to 0.1) correspond to soils, larger numbers ($\sim$ 0.2 to 0.6) indicate the presence of green plant materials, and negative values correspond to water.

Histograms of **NDVI** for the four areas studied are shown in Figure 2-2. The histograms for Rodonia Amazon, Central US, and Northern US clearly show that **NDVI** over these three areas have relatively large positive values, indicating that they are unlikely to be contaminated by the presence of clouds. Hence the estimated statistics of **NDVI** for these three areas are expected to be reasonably accurate. On the other hand, the estimation of **NDVI** over Central Amazon probably is contaminated by the clouds (Figure 2-2(b)) since significant portion of the estimated **NDVI** has values close to zero. Relatively small domain mean and large standard deviation of **NDVI** over Central Amazon reflect this kind of contamination. The **NDVI** data for Central Amazon is not appropriate for analyzing its spatial distribution because of the presence of clouds.

Variability and Length Scale of NDVI Distribution The *variability* of **NDVI** distribution can be defined as the standard deviation of **NDVI**, σ_N, over the entire horizontal mesoscale domain.

The *length scale* of **NDVI** distribution is inherent in the autocorrelation function of **NDVI**, $\rho(r)$, where r is the separation distance along certain direction in the horizontal domain. When the **NDVI** distribution is a horizontally homogeneous random field, its autocorrelation function will decay with increasing lag r. One of the measures of the length scale of the **NDVI** random field may be defined as the integration of the autocorrelation function over entire r.

Autocorrelation Functions of NDVI Distribution

NDVI (1km AVHRR) data collected at three locations, Rodonia Amazon, Central US, and Northern US, were used to compute two-dimensional correlation functions and corresponding variances.

The following functional form is found to be the best-fit of the two-dimensional autocor-

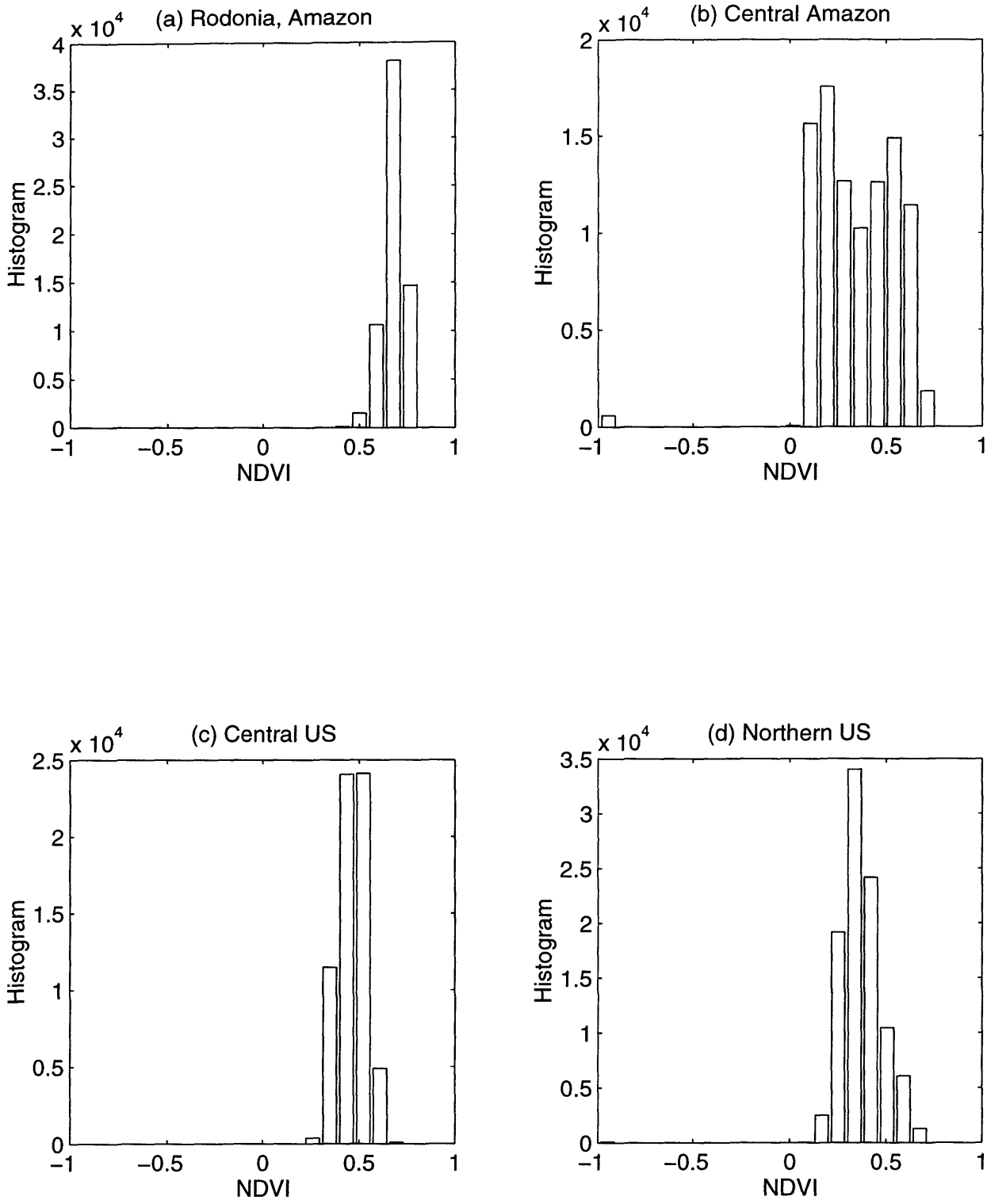

Figure 2-2: Histograms of **NDVI** over four regions from AVHRR observations.

Location	$\overline{NDVI}$	σ_N	L_x (km)	n_x	L_x^N (km)	L_y (km)	n_y	L_y^N (km)
Rodonia Amazon	0.69	0.047	31.9	0.37	133.5	15.9	0.51	30.7
Central US	0.48	0.066	13.8	0.41	42.9	8.9	0.66	12.0
Northern US	0.32	0.082	12.0	0.75	14.3	24.3	0.50	48.6

Table 2.1: Statistics of NDVI data from 1KM AVHRR observations.

relation function of **NDVI** at the above locations

$$\rho(r) = \exp\{-(\frac{r}{L_r})^{n_r}\} \tag{2.2}$$

where r is the radial distance. Parameter L_r is direction ($\vec{r} = (x, y)$) dependent and has a unit of length. The corresponding index n_r is a parameter ranging from 0 to 1. This form of function is a legitimate autocorrelation function (Yaglom, 1987).

The *length scale* of **NDVI**, L_r^N, can be defined as follows (e.g. Christakos, 1992):

$$L_r^N = \int_0^\infty \rho(r)dr \tag{2.3}$$

Use of the functional form of the auto-correlation function of **NDVI** given in Eq (2.2) leads to:

$$L_r^N = \frac{1}{n_r}\Gamma(\frac{1}{n_r})L_r \tag{2.4}$$

where Γ is the gamma function. The impact of parameter n_r on L_r^N is illustrated in Figure 2-3.

The estimated two-dimensional autocorrelation functions of **NDVI** for Rodonia Amazon, Central US, and Northern US are plotted in Figure 2-4(a), 2-5(a), 2-6(a), respectively. The corresponding one-dimensional autocorrelation functions along x-direction (longitudinal) and y-direction (latitudinal) are shown in Figure 2-4(b) (c), Figure 2-5(b) (c), and Figure 2-6(b) (c), respectively. The statistical properties (domain means, standard deviations, and correlation scales) for these three locations are summarized in Table 2.1.

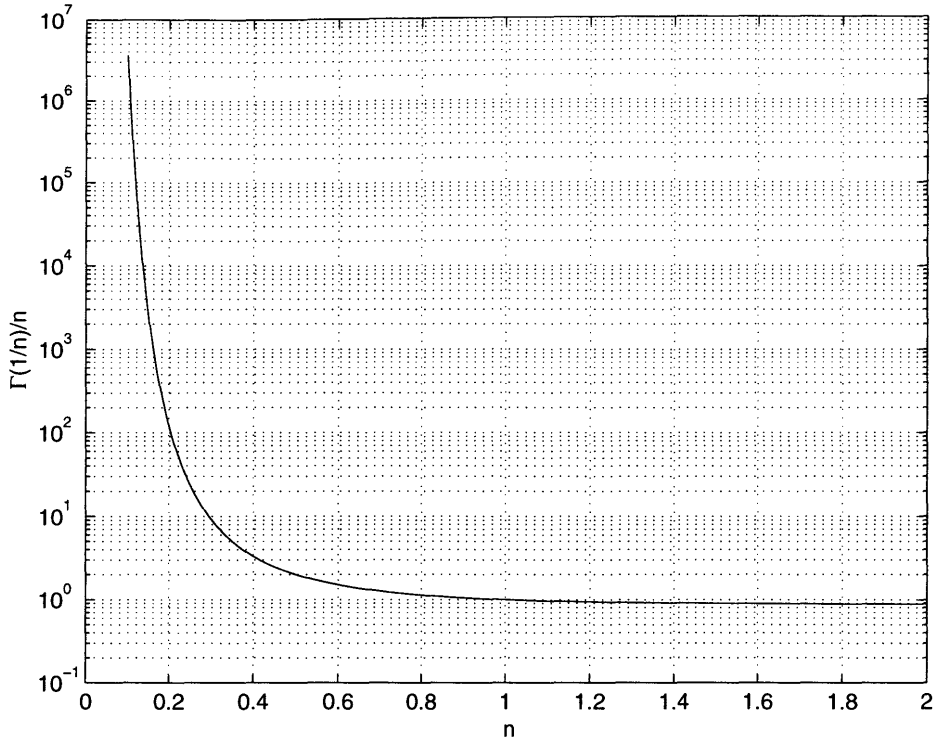

Figure 2-3: Function $\frac{1}{n}\Gamma(\frac{1}{n})$.

Comments

Table 2.1 shows that the standard deviations and length scales of **NDVI** distribution vary significantly from place to place. The domain means of **NDVI** range from 0.32 for Northern US to 0.69 for Rodonia Amazon. This large difference indicates that the vegetation in that part of Amazon basin is much denser than in northern US. The standard deviations of **NDVI** range from 0.047 for Rodonia Amazon to 0.082 for Northern US. The relatively small standard deviation of **NDVI** in Rodonia Amazon means that the canopy cover there is quite uniform.

The length scales of **NDVI** distribution also differ substantially depending on the location. Table 2.1 shows that the length scales range from some 10 to 100 km. Some anisotropy is evident over all areas studied.

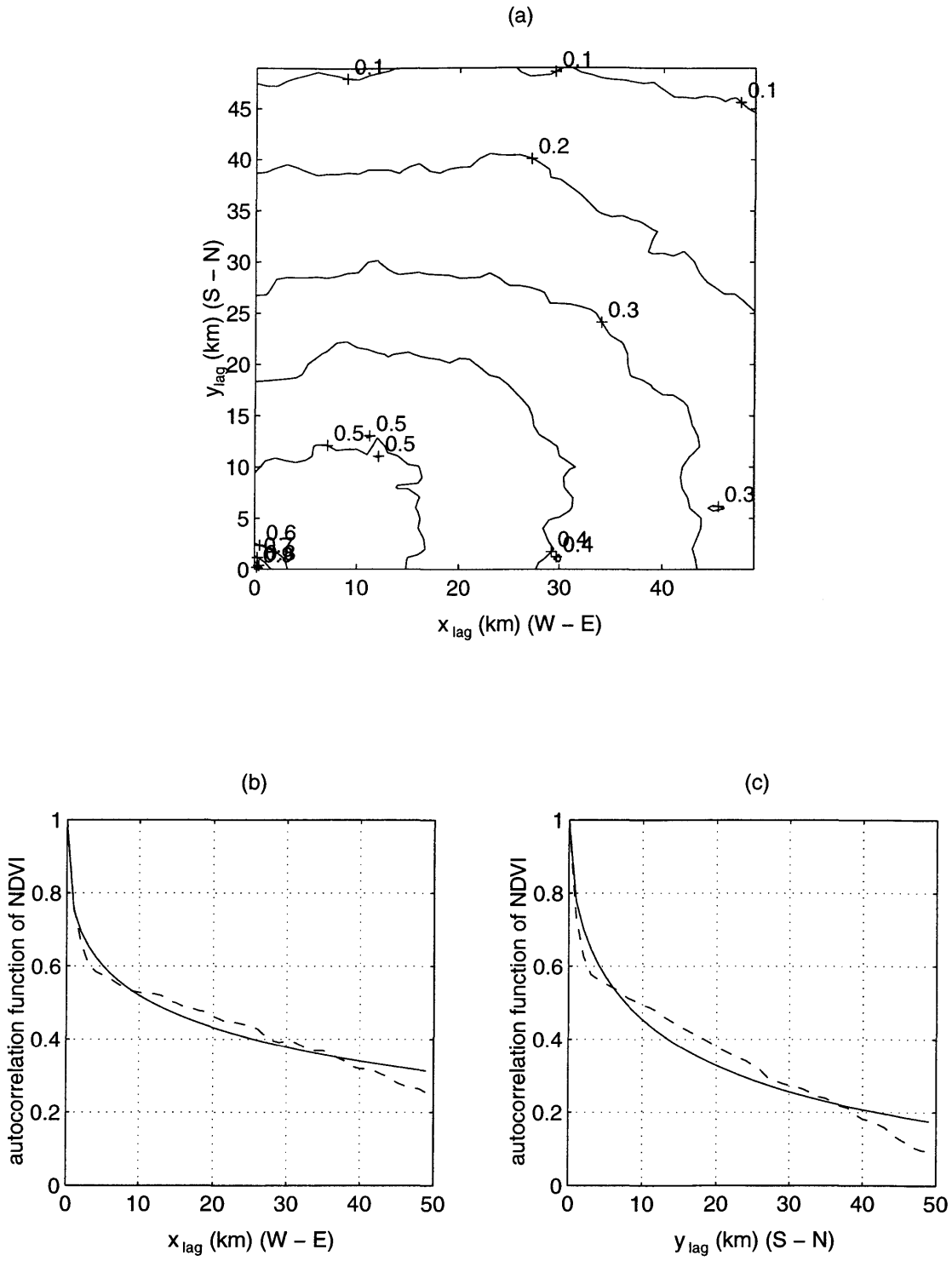

Figure 2-4: Autocorrelation function of **NDVI** for Rodonia, Amazon. (a) 2D autocorrelation function, (b) 1D autocorrelation function along W-E direction, (c) 1D autocorrelation function along S-N direction. Data (dashed line), fitted curve (solid line).

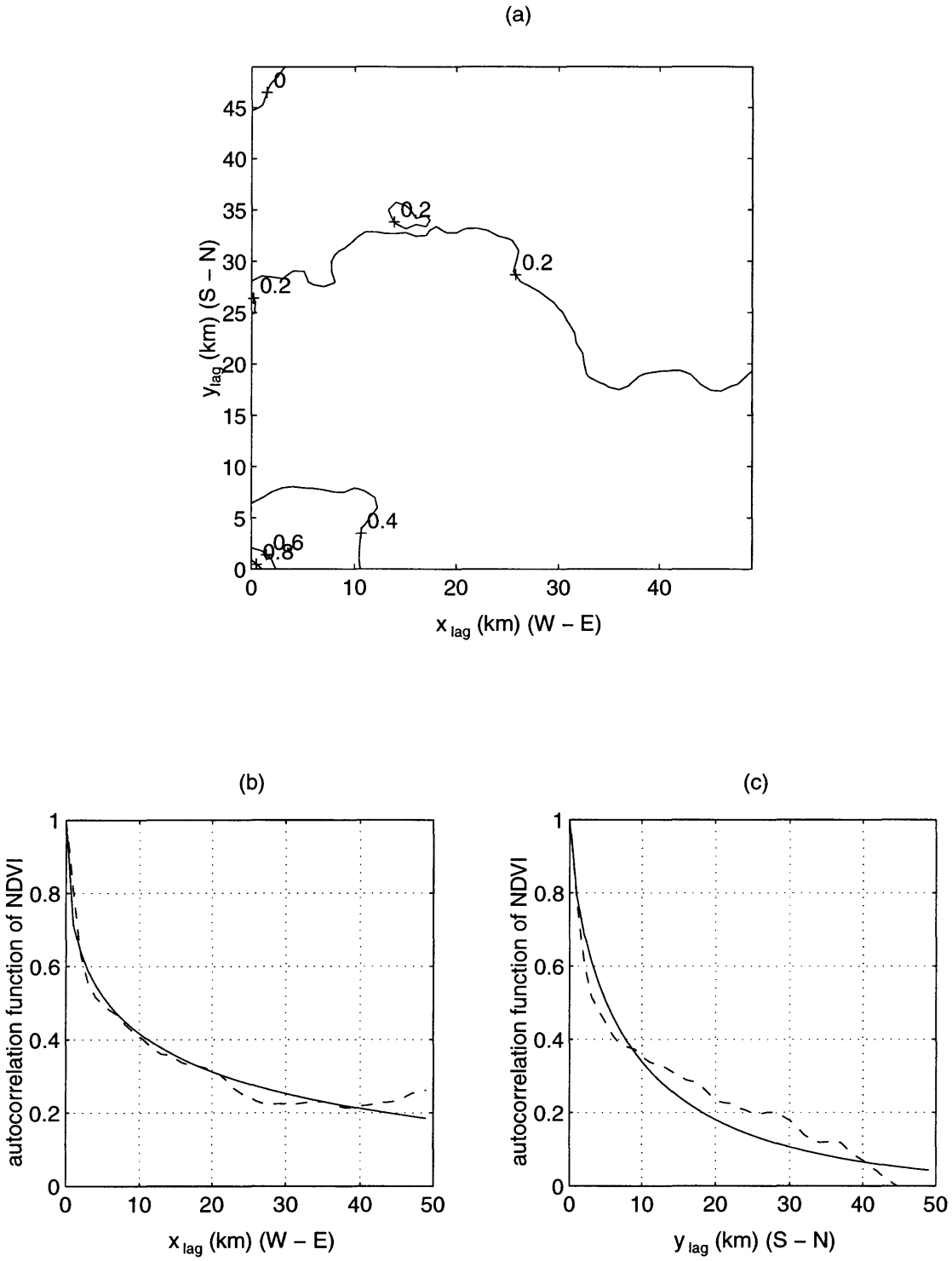

Figure 2-5: Autocorrelation function of **NDVI** for Central US. (a) 2D autocorrelation function, (b) 1D autocorrelation function along W-E direction, (c) 1D autocorrelation function along S-N direction.

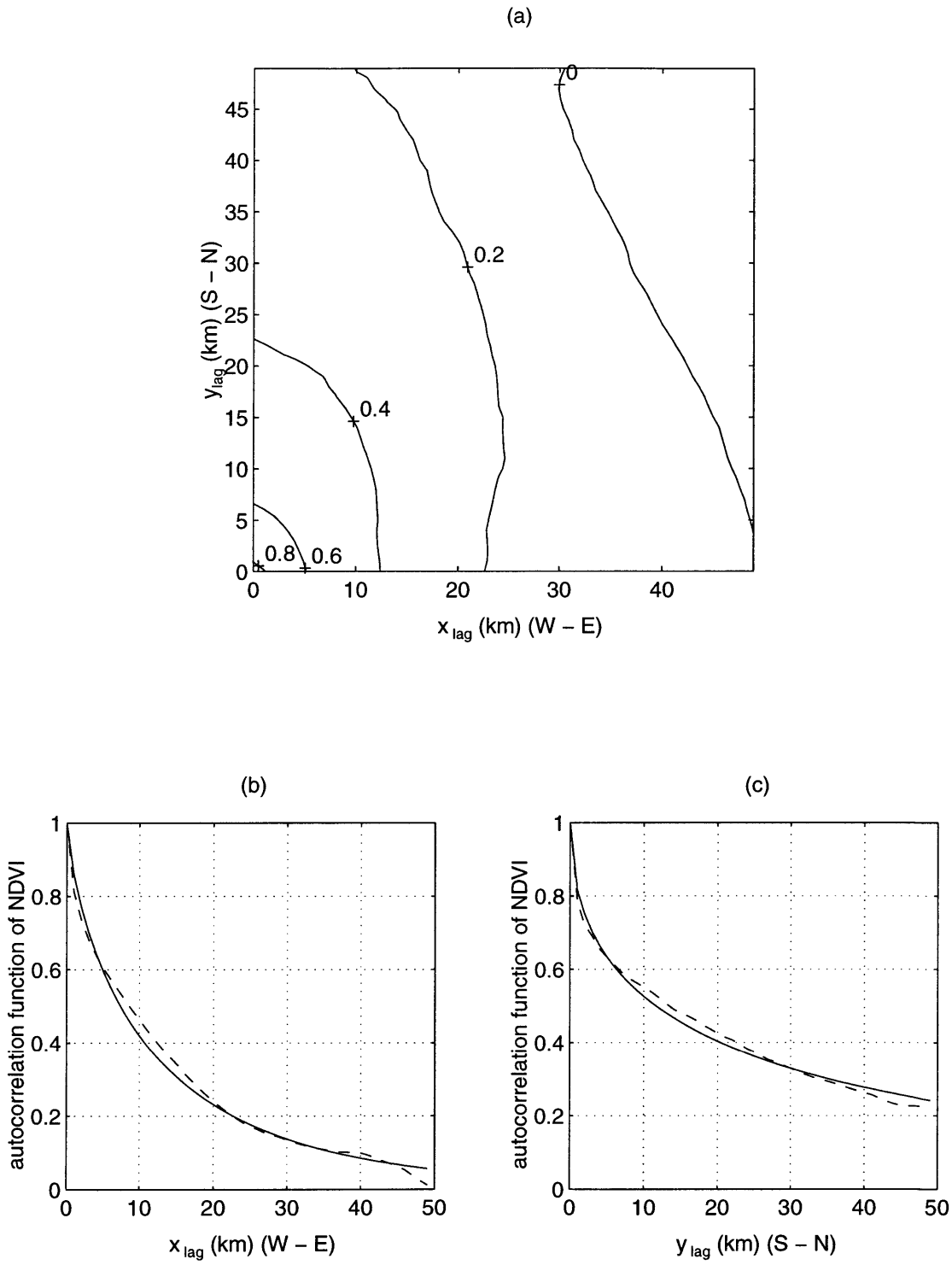

Figure 2-6: Autocorrelation function of **NDVI** for Northern US. (a) 2D autocorrelation function, (b) 1D autocorrelation function along W-E direction, (c) 1D autocorrelation function along S-N direction.

2.1.2 Spatial Distribution of TSHF

Sun & Mahrt (1994) show that **TSHF** is highly correlated with **NDVI**. A linear regression between **TSHF** at surface and **NDVI** is of the form

$$\mathbf{TSHF} = a \cdot \mathbf{NDVI} + b \tag{2.5}$$

where the regression coefficients a and b need to be calibrated using the **NDVI** measurements where the direct measurements of **TSHF** are available. This relationship can be used to retrieve the spatial distribution of **TSHF** from spatial distribution of **NDVI**.

For the purpose of estimating the realistic variability of **TSHF**, it would be reasonable to assume that **TSHF** corresponds to a maximum value $H_{\max}$ when **NDVI** equals to -1 and to a minimum value $H_{\min}$ when **NDVI** equals to $+1$. Consequently, Eq. (2.5) becomes

$$\mathbf{TSHF} = -\frac{1}{2}(H_{\max} - H_{\min}) \cdot \mathbf{NDVI} + \frac{1}{2}(H_{\max} + H_{\min}) \tag{2.6}$$

Eq. (2.6) leads to the following formula relating the standard deviation of **TSHF** at surface, σ_H, to that of **NDVI**, σ_N

$$\sigma_H = \frac{1}{2}(H_{\max} - H_{\min})\sigma_N. \tag{2.7}$$

σ_H is one of the key parameters in the stochastic linear model developed in the next chapter.

Representative values of $H_{\min}$ and $H_{\max}$ are used here to produce an estimate of σ_H. Two extreme cases of land surface conditions, i.e. zero and potential evaporation rate, will correspond to $H_{\min} \sim 0$ W m^{-2}, $H_{\max} \sim 500$ W m^{-2}. As shown in Table 2.1, $\sigma_N \sim 0.05-0.10$ estimated from the 1KM AVHRR datasets. Then σ_H is on the order of

$$\sigma_H \sim 10 - 25 \text{ W m}^{-2}$$

The linearity of Eq. (2.5) implies that the length scale properties of **TSHF** are the same as those of **NDVI**.

2.2 Topographical Variability of Land Surface

Natural topography over a mesoscale terrain is frequently irregular. Adequate characterization of this complex topography needs a random function description. In evaluating the impact of topography on the airflow over complex terrain in terms of second moments, the spectrum of topography is required.

Topographic data with different spatial coverage and resolutions have been analyzed to estimate the properties of its spectrum. Bretherton (1969) reported a power-law spectrum with an exponent -3/2 based upon the average of 90 East/West traverses across north Walse. He further suggested that in general a power-law spectrum with exponent somewhere between -1 and -2 was appropriate for mesoscale topography.

Young and Pielke (1983) used the **NOAA/EDIS/NGSDC** 30 s (of latitude and longitude, i.e. $\sim$ 900m resolution) average elevation data for a domain of some 300 km in side. A power-law line spectrum was identified with exponent -1.

Steyn and Ayotte (1985) estimated a 2D spectrum using **DEM** data. For the case of isotropic topography at St. Mary Lake, Canada, a power-law spectrum with exponent -5/2 was identified over a region of 20×30 km^2. For the anisotropic mountains in Blair's Mills, Pennsylvania, a power-law spectrum with exponent -2 was obtained along the direction of the major harmonics.

Bannon and Yuhas (1990) analyzed high-resolution topographic data for Appalachian Mountains of the northeast US. 1D W-E profiles of the topography over the region bounded by 84°W, 72°W, 37°N, 45°N were used to estimate the spectrum. A power-law with exponent -1.7 was identified.

In summary, observational studies have suggested that the spectrum of complex topography follows a power-law over a wide range of scales. For the power-law spectrum of complex mesoscale terrains, $S_h(k)$, the exponent was somewhere between -1 and -2.5:

$$S_h(k) \propto k^{-n}, \qquad 1 \leq n \leq 5/2$$

where k is the wave number. Typical value of the standard deviation of topography is on

the order of a few hundred meters for the mountains of moderate height.

2.3 Summary

Variability (standard deviation) and length scale are two important parameters for characterizing the spatial distribution of surface heating and topographical forcing for mesoscale circulation described by homogeneous random fields. The standard deviation of **TSHF** is found to be on the order of 30 W m^{-2}, and the corresponding length scales ranges from 10^1 to 10^2 km. The standard deviation of topography of moderate height ($< u_0/N \sim 10^3$ m for typical values of synoptic wind $u_0 \sim 10$ m s^{-1} and Brunt-Väisälä frequency $N \sim 10^{-2}$ s^{-1}) is on the order of 10^2 m. This variability of topography has been found to distribute over length scales on the order of $10^1 \sim 10^2$ km following a power law spectrum with exponent between -1 to -5/2. The surface forcings for mesoscale circulation used in the linear and nonlinear analysis conducted in the following chapters will be based on these values.

Chapter 3

Stochastic Linear Model of Thermally Induced Flow

3.1 Background and Motivation

The fundamental mechanism of differential heating induced flow has been known for many years. Artkinson (1981) provided an insightful outline of the theories for thermally induced mesoscale circulation in his monograph. However, classical results on this subject were obtained by assuming simple patterns of thermal heterogeneity, namely water-land contrast. One unanswered question is what if the thermal heterogeneity of the land surface has complex or random distributions rather than the simple distribution assumed in these early theoretical models.

Efforts have been on-going to investigate the impact of complex land surface heterogeneity on the mesoscale circulation, motivated by assessing the contribution of subgrid processes to the resolved processes in large scale atmospheric models. For example, Dalu & Pielke (1989, 1993) and Dalu *et al* (1991) extended Rotunno's work (1983) to study the effects of the non-periodic forcing on the thermally induced mesoscale flow. They found that the detailed distribution of the land surface heterogeneity plays an important role in determining the intensity of the flow. The thermal forcing driving the mesoscale circulation depends on the gradient of the variable surface heat flux. A smoother distribution of sensible heat flux

leads to a weaker forcing. When the spatial distribution of thermal heterogeneity of the land surface is modeled as a homogeneous random field, an important task is to quantify the corresponding gradient.

A stochastic linear theory is developed in this chapter to identify the conditions under which the thermally induced mesoscale circulation and the associated mesoscale fluxes are important, under random surface forcing.

The stochastic linear theory presented in this chapter improves previous work in three ways. First, a three-dimensional model is adopted. All the aforementioned theoretical studies utilize two-dimensional models. Second, the thermal inhomogeneity of land surface in our 3D model is characterized by a 2D random field that realistically represents the complexity of natural landscape. This is in contrast to the over simplified landscape patterns, in the form of periodic warm-cool stripes, that were assumed by previous studies. Third, the effects of synoptic wind are studied quantitatively.

3.2 Stochastic Modeling of 3D Atmospheric Flow

3.2.1 Governing Equations

The motion of a mesoscale system can be described by the eqautions of the following general form,

$$\frac{\partial u}{\partial t} + (u_0 + u)\frac{\partial u}{\partial x} + v\frac{\partial u}{\partial y} + w\frac{\partial u}{\partial z} - fv = -\frac{\partial \phi}{\partial x} + D_x \tag{3.1}$$

$$\frac{\partial v}{\partial t} + (u_0 + u)\frac{\partial v}{\partial x} + v\frac{\partial v}{\partial y} + w\frac{\partial v}{\partial z} + fu = -\frac{\partial \phi}{\partial y} + D_y \tag{3.2}$$

$$\frac{\partial w}{\partial t} + (u_0 + u)\frac{\partial w}{\partial x} + v\frac{\partial w}{\partial y} + w\frac{\partial w}{\partial z} - b = -\frac{\partial \phi}{\partial z} + D_z \tag{3.3}$$

$$\frac{\partial b}{\partial t} + (u_0 + u)\frac{\partial b}{\partial x} + v\frac{\partial b}{\partial y} + w\frac{\partial b}{\partial z} + N^2 w = Q(x, y, z, t) + D_b \tag{3.4}$$

$$\frac{\partial u}{\partial x} + \frac{\partial v}{\partial y} + \frac{\partial w}{\partial z} = 0 \tag{3.5}$$

where b is the buoyancy, ϕ is the geopotential; f is the Coriolis parameter; D_x, D_y, D_z and D_b represent dissipation of momentum and heat; $\alpha^{-1}(\sim \mathrm{O}(T_0)$; N is the Brunt-Väisälä frequency. Q is the buoyancy source (the time rate of change of the acceleration of parcel forced by the air density difference) due to the turbulent sensible heat flux, H_t,

$$Q = -\frac{g}{\rho C_P \theta_0}\frac{\partial H_t}{\partial z} \tag{3.6}$$

where ρ is the air density, θ_0 is the constant reference potential temperature, C_P is the heat capacity of the air at the constant pressure, and g is the gravitational acceleration.

Linearization Deriving an analytical solution of Eqs. (3.1) - (5.81) is formidably difficult, if not impossible. Linearizaion of the above equations requires neglecting all nonlinear advective terms and relating the dissipative terms to the corresponding dependent variables in a linear fashion. The momentum and heat dissipation can be modeled in terms of linear damping called Rayleigh friction (e.g. Hsu, 1987),

$$D_x = -\alpha u \tag{3.7}$$

$$D_y = -\alpha v \tag{3.8}$$

$$D_z = -\alpha w \tag{3.9}$$

$$D_b = -\alpha b \tag{3.10}$$

where $\alpha^{-1}(\sim \mathrm{O}(T_0)$, Dalu *et al*, 1989) is the damping time scale.

The three-dimensional linearized equations describing the flow driven by the gradients of diabatic heating caused by variability of the land surface can be formulated as

$$\frac{\partial u}{\partial t} + u_0\frac{\partial u}{\partial x} - fv = -\frac{\partial \phi}{\partial x} - \alpha u \tag{3.11}$$

$$\frac{\partial v}{\partial t} + u_0\frac{\partial v}{\partial x} + fu = -\frac{\partial \phi}{\partial y} - \alpha v \tag{3.12}$$

$$\frac{\partial w}{\partial t} + u_0\frac{\partial w}{\partial x} - b = -\frac{\partial \phi}{\partial z} - \alpha w \tag{3.13}$$

$$\frac{\partial b}{\partial t} + u_0\frac{\partial b}{\partial x} + N^2 w = Q(x,y,z,t) - \alpha b \tag{3.14}$$

$$\frac{\partial u}{\partial x} + \frac{\partial v}{\partial y} + \frac{\partial w}{\partial z} = 0 \tag{3.15}$$

3.2.2 Statistical Description of the Diabatic Heating

Consider a mesoscale domain covered by a variety of vegetation or wet and dry patches of irregular patterns whose dimensions are small relative to the domain size. This situation allows the turbulent sensible heat flux (diabatic heating), H_t, at the surface to be modeled as a two-dimensional homogeneous random field. H_t is further assumed to decay upward in an exponential fashion with a constant e-folding height h ($\sim$ 1km). This vertical profile of H_t has been also represented by others using a straight line within the convective boundary layer. The use of exponential function has advantages for the theoretical framework presented in this paper, while capturing the fundamental feature of the reality (turbulent sensible heat flux decaying upward with certain scale) and yet keeping the mathematical simplicity essential to the analytical solution without obfuscating the underlying physics. This exponential function has been used in the theoretical study by Rotunno (1983) and is qualitatively consistent with numerical simulations of turbulent heat flux, e.g. Avissar & Chen (1993) and Lynn *et al* (1995). It can be shown that the quantitative properties of the mesoscale circulation and fluxes do not sensitively depend on the shape of the vertical profile of H_t. H_t has a diurnal cycle following closely the insolation curve $I(t)$. This is due to the fact that the turbulent heat flux is almost in-phase with solar radiation as corroborated by many observational studies, e.g. Smith *et al* (1992). Therefore H_t is modeled as

$$H_t = \hat{H}(x, y) \exp(-\frac{z}{h}) I(t) \tag{3.16}$$

where $\hat{H}$ (W m^{-2}) is a random function characterizing the thermal variability of land surface that will be specified in section 3.3. Hence the buoyancy source Q due to H_t can be written in terms of,

$$Q = \hat{Q}(x, y) \exp(-\frac{z}{h}) I(t) \tag{3.17}$$

where $\hat{Q}$ (m s^{-3}) relates to $\hat{H}$ through

$$\hat{Q} = \frac{g}{\rho C_P \theta_0 h} \hat{H} \tag{3.18}$$

Assuming $\hat{H} \sim 10^2 \mathrm{Wm}^{-2}$, $\theta_0 \sim 300\mathrm{K}$ and $h \sim 10^3\mathrm{m}$ leads to $\hat{Q}$ being on the order of 10^{-5} m s^{-3}.

The insolation curve $I(t)$ is defined by

$$I(t) = \begin{cases} \sin(\Omega t) & , \quad 0 \leq t \leq T_0/2 \quad (\mathrm{day-time}) \\ 0 & , \quad T_0/2 < t \leq T_0 \quad (\mathrm{night}) \end{cases} \tag{3.19}$$

where Ω is the rotation rate of the Earth, and T_0 is one day.

3.3 Analytical Solution

3.3.1 Decomposition and the Spectral Representation

Randomness in the buoyancy source Q makes all dependent variables in Eqs. (3.11) through (3.15) random. Given the linearity of the governing equations it is safe to assume that if the external forcing of the flow is homogeneous horizontally so will the dependent variables.

The first step in the solution of the system of stochastic differential equations is to decompose the dependent variables and the buoyancy source into their horizontal domain mean and a perturbation around the mean:

$$u = \bar{u} + u' \tag{3.20}$$

$$v = \bar{v} + v' \tag{3.21}$$

$$w = \bar{w} + w' \tag{3.22}$$

$$\phi = \bar{\phi} + \phi' \tag{3.23}$$

$$b = \bar{b} + b' \tag{3.24}$$

$$\hat{Q} = \bar{\hat{Q}} + \hat{Q}' \tag{3.25}$$

The linear dynamic system for the state variables u, v, w, b and ϕ also implies that the perturbation terms $()'$ are decoupled from the mean $\bar{()}$. They both satisfy the governing Eqs. (3.11) through (3.15). From now on we focus only on the perturbation terms.

Using spectral representation, Yaglom (1987), the perturbation terms u', v', w', b', ϕ' and $\hat{Q}'$ can be expressed as

$$u' = \int_{-\infty}^{\infty}\int_{-\infty}^{\infty} e^{i(k_1 x + k_2 y)} dZ_u(k_1, k_2; z, t) \tag{3.26}$$

$$v' = \int_{-\infty}^{\infty}\int_{-\infty}^{\infty} e^{i(k_1 x + k_2 y)} dZ_v(k_1, k_2; z, t) \tag{3.27}$$

$$w' = \int_{-\infty}^{\infty}\int_{-\infty}^{\infty} e^{i(k_1 x + k_2 y)} dZ_w(k_1, k_2; z, t) \tag{3.28}$$

$$b' = \int_{-\infty}^{\infty}\int_{-\infty}^{\infty} e^{i(k_1 x + k_2 y)} dZ_b(k_1, k_2; z, t) \tag{3.29}$$

$$\phi' = \int_{-\infty}^{\infty}\int_{-\infty}^{\infty} e^{i(k_1 x + k_2 y)} dZ_\phi(k_1, k_2; z, t) \tag{3.30}$$

$$\hat{Q}' = \int_{-\infty}^{\infty}\int_{-\infty}^{\infty} e^{i(k_1 x + k_2 y)} dZ_Q(k_1, k_2) \tag{3.31}$$

where dZ_u, dZ_v, dZ_w, dZ_b, dZ_ϕ and dZ_Q are the random variables in the frequency domain (k_1, k_2) corresponding to u', v', w', b', ϕ' and $\hat{Q}'$ in the physical domain (x, y). dZ_Q has a prescribed spectral density function, $S_Q(k_1, k_2)$, characterizing the thermal variability of the land surface

$$\sigma_Q^2 S_Q(k_1, k_2) = \frac{\mathrm{E}[\mid dZ_Q(k_1, k_2) \mid^2]}{dk_1 dk_2} \tag{3.32}$$

where σ_Q is proportional to σ_H according to (3.18). σ_H is the standard deviation of the turbulent heat flux into the atmosphere at the time of maximum solar radiation at the ground. It is a measure of the variability in the turbulent sensible heat flux from the land surface.

3.3.2 Governing Equations in the Frequency Domain

The governing equations for dZ's can be readily derived by substituting Eqs. (3.26) through (3.31) into Eqs. (3.11) through (3.15), resulting in

$$(\frac{\partial}{\partial t} + \alpha + ik_1u_0)(dZ_u) - f(dZ_v) = -ik_1(dZ_\phi) \tag{3.33}$$

$$(\frac{\partial}{\partial t} + \alpha + ik_1u_0)(dZ_v) + f(dZ_u) = -ik_2(dZ_\phi) \tag{3.34}$$

$$(\frac{\partial}{\partial t} + \alpha + ik_1u_0)(dZ_w) - (dZ_b) = -\frac{\partial}{\partial z}(dZ_\phi) \tag{3.35}$$

$$(\frac{\partial}{\partial t} + \alpha + ik_1u_0)(dZ_b) + N^2(dZ_w) = I(t)\exp(-\frac{z}{h})(dZ_Q) \tag{3.36}$$

$$ik_1(dZ_u) + ik_2(dZ_v) + \frac{\partial}{\partial z}(dZ_w) = 0 \tag{3.37}$$

3.3.3 Solution for the dZ's

The analytical solution of the Eqs. (3.33) through (3.37) with the proper initial and boundary conditions is shown below while the detailed derivation is given in Appendix B.

a) when $N \neq f$

$$dZ_u = i\{\frac{fk_2h}{f^2 - k^2h^2N^2}[\exp(-\frac{z}{h}) - \frac{N}{f}kh\exp(-\frac{N}{f}kz)]I_0(t;u_0,\alpha) - \frac{2}{\pi}\frac{kh}{1-k^2h^2} \int_a^b \cos(zkG(\xi))G(\xi)\frac{\xi k_1hI_s(t,\xi;u_0,\alpha) - fk_2hI_c(t,\xi;u_0,\alpha)}{(\Lambda^2-\xi^2)\xi}d\xi\}dZ_Q \tag{3.38}$$

$$dZ_v = -i\{\frac{fk_1h}{f^2 - k^2h^2N^2}[\exp(-\frac{z}{h}) - \frac{N}{f}kh\exp(-\frac{N}{f}kz)]I_0(t;u_0,\alpha) + \frac{2}{\pi}\frac{kh}{1-k^2h^2} \int_a^b \cos(zkG(\xi))G(\xi)\frac{\xi k_2hI_s(t,\xi;u_0,\alpha) + fk_1hI_c(t,\xi;u_0,\alpha)}{(\Lambda^2-\xi^2)\xi}d\xi\}dZ_Q \tag{3.39}$$

$$dZ_w = -\{\frac{2}{\pi}\frac{k^2h^2}{1-k^2h^2}\int_a^b \sin(zkG(\xi))\frac{I_s(t,\xi;u_0,\alpha)}{\Lambda^2-\xi^2}d\xi\}dZ_Q \tag{3.40}$$

$$dZ_b = \{[\exp(-\frac{z}{h}) + \frac{k^2h^2N^2}{f^2-k^2h^2N^2}(\exp(-\frac{z}{h}) - \exp(-\frac{N}{f}kz))]I_0(t;u_0,\alpha)$$

$$-\frac{2}{\pi}\frac{k^2h^2N^2}{1-k^2h^2}\int_a^b \sin(zkG(\xi))\frac{I_c(t,\xi;u_0,\alpha)}{(\Lambda^2-\xi^2)\xi}d\xi\}dZ_Q \tag{3.41}$$

$$\begin{aligned} dZ_\phi &= h\{\frac{-f^2}{f^2-k^2h^2N^2}[\exp(-\frac{z}{h})-\frac{N}{f}kh\exp(-\frac{N}{f}kz)]I_0(t;u_0,\alpha)+ \\ &\quad \frac{2}{\pi}\frac{kh}{1-k^2h^2}\int_a^b \cos(zkG(\xi))G(\xi)\frac{\xi^2-f^2}{\Lambda^2-\xi^2}\frac{I_c(t,\xi;u_0,\alpha)}{\xi}d\xi\}dZ_Q \end{aligned} \tag{3.42}$$

b) when $N = f$

$$\begin{aligned} dZ_u &= \frac{i}{f(1-k^2h^2)}\{\exp(-\frac{z}{h})-kh\exp(-zk)\} \\ &\quad \{k_1hI_s(t,f;u_0,\alpha)+k_2h[I_0(t;u_0,\alpha)-I_c(t,f;u_0,\alpha)]\}dZ_Q \end{aligned} \tag{3.43}$$

$$\begin{aligned} dZ_v &= \frac{i}{f(1-k^2h^2)}\{\exp(-\frac{z}{h})-kh\exp(-zk)\} \\ &\quad \{k_2hI_s(t,f;u_0,\alpha)-k_1h[I_0(t;u_0,\alpha)-I_c(t,f;u_0,\alpha)]\}dZ_Q \end{aligned} \tag{3.44}$$

$$dZ_w = -\frac{k^2h^2}{f(1-k^2h^2)}\{\exp(-\frac{z}{h})-\exp(-kz)\}I_s(t,f;u_0,\alpha)dZ_Q \tag{3.45}$$

$$\begin{aligned} dZ_b &= \{\exp(-\frac{z}{h})I_0(t;u_0,\alpha)+\frac{k^2h^2}{1-k^2h^2}[\exp(-\frac{z}{h})-\exp(-zk)] \\ &\quad [I_0(t;u_0,\alpha)-I_c(t,f;u_0,\alpha)]\}dZ_Q \end{aligned} \tag{3.46}$$

$$dZ_\phi = -\frac{h}{1-k^2h^2}\{\exp(-\frac{z}{h})-kh\exp(-zk)\}I_0(t;u_0,\alpha)dZ_Q \tag{3.47}$$

where

$$[a,b] = [\min\{f,N\},\max\{f,N\}] \tag{3.48}$$

$$\Lambda^2 = \frac{f^2-k^2h^2N^2}{1-k^2h^2} \tag{3.49}$$

$$G(\xi) = \left| \frac{N^2 - \xi^2}{f^2 - \xi^2} \right|^{\frac{1}{2}} \tag{3.50}$$

$$I_0(t; u_0, \alpha) = \int_0^t I(\tau) \exp\left[-(\alpha + ik_1 u_0)(t - \tau)\right] d\tau \tag{3.51}$$

$$I_s(t, \xi; u_0, \alpha) = \int_0^t I(\tau) \sin\left[\xi(t - \tau)\right] \exp\left[-(\alpha + ik_1 u_0)(t - \tau)\right] d\tau \tag{3.52}$$

$$I_c(t, \xi; u_0, \alpha) = \int_0^t I(\tau) \cos\left[\xi(t - \tau)\right] \exp\left[-(\alpha + ik_1 u_0)(t - \tau)\right] d\tau \tag{3.53}$$

ξ is a dummy integration variable, and $I(t)$ given in (3.19). The other symbols are specified in Appendix A.

For the sake of brevity, we rewrite the solution given in (3.38) through (3.47) as

$$dZ_u = \Pi_u(k_1, k_2; z, t) dZ_Q \tag{3.54}$$

$$dZ_v = \Pi_v(k_1, k_2; z, t) dZ_Q \tag{3.55}$$

$$dZ_w = \Pi_w(k_1, k_2; z, t) dZ_Q \tag{3.56}$$

$$dZ_b = \Pi_b(k_1, k_2; z, t) dZ_Q \tag{3.57}$$

$$dZ_\phi = \Pi_\phi(k_1, k_2; z, t) dZ_Q \tag{3.58}$$

3.4 Statistics of the Mesoscale Circulation

In the framework of stochastic analysis the intensity of the mesoscale circulation can be quantified by the standard deviation (square root of the variance) σ_u, σ_v and σ_w of the wind velocities u, v and w, respectively. They characterize the magnitude of the perturbation in wind velocities. The horizontal distribution of the mesoscale circulation can be characterized by the length scales. For instance, the length scale of vertical velocity w provides a measure of the size of a typical circulation cell. In the frequency domain these length scales correspond to wave numbers around which a large portion of the variance concentrates. The length scale L is equal to the inverse of the wave number k multiplied by 2π.

3.4.1 Properties of σ_i

The flow intensity is basically determined by the parameters characterizing the synoptic environment and the thermal properties of the landscape. Significant land breeze circulation is expected to be associated with a sufficiently large thermal gradient. Atmospheric stability provides a resistance against the upward motion of the air forced by diabatic heating. Strong synoptic wind tends to smooth out the locally generated flow structures. The analytical solution in the previous section enables us to investigate the effects of these parameters quantitatively.

The variances can be computed from Eqs. (3.54) through (3.56) as

$$\begin{aligned} \sigma_i^2(z,t) &= \int_{-\infty}^{\infty}\int_{-\infty}^{\infty} \mathrm{E}[\mid dZ_i \mid^2] dk_1 dk_2 \\ &= \int_{-\infty}^{\infty}\int_{-\infty}^{\infty} \mid \Pi_i(k_1,k_2;z,t) \mid^2 \sigma_Q^2 S_Q(k_1,k_2) dk_1 dk_2 \end{aligned} \tag{3.59}$$

where the index i represents u, v, w. This equation predicts a linear relationship between the flow intensity σ_i and the thermal gradient σ_Q or σ_H. In the following analysis it is convenient to normalize σ_i by σ_H.

To compute σ_i using (3.59), the functional form of $S_Q(k_1,k_2)$ needs to be specified. In principle $S_Q(k_1,k_2)$ must be estimated from the measurement of sensible heat flux at the surface over the region of interest. For the purpose of illustration we may use a hypothetical S_Q function of uniform distribution over a finite frequency domain. The study by André *et al* (1990) showed that nonhomogeneous landscape with characteristic horizontal scale smaller than 10km induces no apparent coherent atmospheric response. This result suggests a higher wavenumber cutoff in S_Q. The lower wavenumber cutoff should correspond to a length scale not too large compared to the mesoscale domain size ($\sim$ 500km). Otherwise the the assumption of homogeneity of the random field of surface heating could be invalid. Based on the above considerations the thermal variability is assumed to have the length scale ranging from 20km to 50km, imposing a high and a low wave number cut-off in (k_1,k_2) domain.

First we investigate the role of synoptic wind u_0 on σ_i under the conditions of neutral

stratification ($N = 0$). Vertical distributions of σ_u, σ_v and σ_w are plotted in Figure 3-1. Their time-behavior is illustrated in Figure 3-2. Comparing σ_i with $u_0 = 0$ in Figure 3-1 with that with $u_0 = 5$ m s^{-1} in Figure 3-3, we see the presence of the synoptic wind strongly inhibits the development of the flow. σ_i decreases by a factor of 30 as the synoptic wind u_0 increases from 0 to 5m s^{-1}. Hence, in an environment with moderate to strong synoptic wind the mesoscale circulation driven by the differential surface heating is very weak.

Stable stratification of the atmosphere affects not only the flow intensity but also the height below which the thermally-induced air flow is active. Figure 3-4 shows that σ_u and σ_v decrease by a factor of 10 as N increases from 0 to 10^{-2}s^{-1}. At the same time σ_w decreases by a factor of 200! Also the height of $\sigma_w^{\max}$ moves from 1800m down to about 200m. The flow in such an environment is constrained within a shallow layer near the surface. The stable atmosphere substantially reduces the intensity and the vertical range of the mesoscale circulation. Consequently, the associated mesoscale fluxes of momentum, heat and moisture are also suppressed.

Rayleigh friction affects both intensity and structure of the mesoscale circulation. As α decreases from 1.2Ω to zero, the intensity of the flow will increase by a factor of three. Without the dissipation ($\alpha = 0$) our results show a non-physical second circulation peak during the night time when there is no solar radiation. These results are not presented.

Comparing Figure 3-1, Figure 3-2 and Figure 3-3 with Fig. 3 and Fig. 8 in Avissar & Chen (1993), we find that general features of the distributions of the horizontal mean mesoscale kinetic energy per unit mass (MKE), $(\sigma_u^2 + \sigma_v^2)/2$, predicted by this stochastic linear theory are consistent with those obtained using the sophisticated mesoscale numerical model. For example, their numerical simulations show that the peak MKE occurs at about 3:00pm. Our theory (see Figure 3-2) gives the same result. We note that MKE is zero at $z = 0$ in the numerical simulations while non-zero from our theory. This difference is caused by the boundary conditions. In the turbulent atmospheric circulation model wind speed at the ground usually is set to be zero because of viscosity. In our linear theory the effect of viscosity is neglected.

We conclude that stability N and synoptic wind u_0 significantly inhibit the development

of the mesoscale circulation caused by the thermal inhomogeneity of the landscape. The flow will not develop to a significant level except in a synoptic environment characterized by a neutral stratification and weak synoptic wind.

3.4.2 Properties of the Spatial Length Scale

The length scale of the thermally induced mesoscale circulation will be studied by analyzing the frequency response function (a term borrowed from *system analysis*) Π_i in Eq. (3.54) - (3.56). The frequency response function fully characterizes the input-output relation of a linear dynamic system when the power is decomposed over frequencies. For the case of zero synoptic wind Π_w depends only on the radius wave number k, implying an isotropic field of vertical velocity w. Hence the scale analysis of the flow is facilitated by studying the properties of Π_w for $u_0 = 0$.

A common feature of Π_w for all altitudes is that it goes to zero as wave number k goes to zero (Figure 3-5). This means the thermal heterogeneity with sufficiently large scale L (very small thermal gradient) is inefficient in driving the land-breeze type flow in the three-dimensional domain. On the other hand, Π_w behaves differently as a function of wave number k at different altitudes. At low altitude, for example $z = 0.1$km, Π_w (Figure 3-5) initially increases with the wave number k, then saturates at $k \simeq 50$, corresponding to a length scale $L \simeq 0.1$km. At $z = 1$km, Π_w behaves similarly but the saturation point moves from $k \simeq 50$ down to $k \simeq 5$. Consequently the corresponding length scale L increases from 0.1km to about 1km. Hence at relatively low altitude the atmosphere has little response to the thermal forcing with large length scales. However at higher altitudes, Π_w reaches a maximum at certain finite wave number, $k_{\max}$. With increasing altitude, the peak of Π_w becomes sharper, and $k_{\max}$ becomes smaller. The atmosphere is most sensitive to the thermal forcing at this particular wave number $k_{\max}$. This behavior could be interpreted as a resonance phenomenon in many dynamic systems. Mesoscale circulation is likely to be observed when the length scale of the forcing is close to the inherent length scale of the mesoscale system. Due to the rapid decay of diabatic heating upward, the forcing needs to be more concentrated around this inherent scale of the mesoscale system so that the mesoscale

flow can be driven to a deeper depth. The graph in Figure 3-5(b) shows the dependence of $k_{\max}$ on altitude z. The $L_{\max} - z$ relation is plotted in Figure 3-6.

The dependence of Π_u, Π_v and Π_b on k turns out to be similar to that of Π_w except they vanish as k goes to infinity. There exist certain wavenumbers (or length scales) at which these $\mid \Pi \mid$ functions have peaks. This property implies that the land surface heterogeneity at certain scales is most effective in driving the mesoscale circulation and fluxes. Influences of landscape variability at very large as well as very small scales on the mesoscale circulation are minimum according to our stochastic linear theory.

In summary, the atmosphere at lower altitude responds to the thermal forcing with small length scales, while at higher altitude it tends to be driven by the forcing with large length scale.

3.5 Water Balance in the Atmosphere

3.5.1 Governing Equations

As a first order approximation we ignore the effect of the latent heat released by the condensation of the water vapor on the atmospheric flow. Thus moisture is assumed to be a passive tracer. The water balance in the atmosphere without precipitation simply states that the total water content q (kg kg^{-1}) is conserved following the flow.

$$\frac{\partial q}{\partial t} + \frac{\partial}{\partial x}(uq) + \frac{\partial}{\partial y}(vq) + \frac{\partial}{\partial z}(wq) = 0 \tag{3.60}$$

where u, v and w are the 3D wind velocities described by Eqs. (3.11) through (3.15).

Using the same arguments as for u, v, w, b and ϕ, the random field q is assumed homogeneous horizontally. As we did in section 3.3.1, q is decomposed into the domain mean $\bar{q}$ and the perturbation term q'

$$q = \bar{q} + q' \tag{3.61}$$

where q' is expressed with the aid of the spectral representation of homogeneous random

field as

$$q' = \int_{-\infty}^{\infty}\int_{-\infty}^{\infty} e^{i(k_1 x + k_2 y)} dZ_q(k_1, k_2; z, t) \tag{3.62}$$

The governing equation for q' can be derived by linearizing Eq. (3.60). The detailed derivation is shown in Appendix C. We have

$$\frac{\partial q'}{\partial t} + u_0 \frac{\partial q'}{\partial x} + w' \frac{d\bar{q}}{dz} = 0 \tag{3.63}$$

where $\bar{q}$ is the mean vertical profile of the moisture in the atmosphere.

The governing equation for dZ_q in the frequency domain is obtained by substituting (3.62) into (3.63),

$$\frac{\partial}{\partial t}(dZ_q) + ik_1 u_0 (dZ_q) = -\frac{d\bar{q}(z)}{dz} dZ_w \tag{3.64}$$

3.5.2 Analytical Solution

Analogous to the procedure used in Appendix B for the solution of dZ_u, dZ_v, dZ_w, dZ_b and dZ_ϕ, the analytical solution of dZ_q can be shown to be

a) when $N \neq f$

$$\begin{aligned} dZ_q \;=\; & \frac{d\bar{q}(z)}{dz}\{\frac{k^2h^2}{(f^2+\alpha^2) - k^2h^2(N^2+\alpha^2)}[\exp(-\frac{z}{h}) - \\ & \exp(-kz(N^2+\alpha^2)^{\frac{1}{2}}(f^2+\alpha^2)^{-\frac{1}{2}})]I_0(t;u_0,0) - \frac{2}{\pi}\frac{k^2h^2}{1-k^2h^2} \\ & \int_a^b \sin(zkG(\xi))\frac{\xi I_c(t,\xi;u_0,\alpha) + \alpha I_s(t,\xi;u_0,\alpha)}{(\Lambda^2-\xi^2)(\xi^2+\alpha^2)}d\xi\}dZ_Q \end{aligned} \tag{3.65}$$

b) when $N = f$

$$dZ_q = \frac{d\bar{q}(z)}{dz}\{\frac{k^2h^2}{(f^2+\alpha^2)(1-k^2h^2)}[\exp(-\frac{z}{h}) - \exp(-zk)] \\ [I_0(t;u_0,0) - I_c(t,f;u_0,\alpha) - \frac{\alpha}{f}I_s(t,f;u_0,\alpha)]\}dZ_Q \quad (3.66)$$

Again, we write (3.65) and (3.66) in a short form

$$dZ_q = \frac{d\bar{q}(z)}{dz}\Pi_q(k_1,k_2;z,t)dZ_Q \quad (3.67)$$

3.6 Mesoscale Fluxes

Many recent numerical studies have argued that heat fluxes associated the thermally induced flow may be comparable to the turbulent heat fluxes under the same synoptic conditions. Next we attempt to study the intensity and the spatial-temporal patterns of the mesoscale fluxes of momentum, heat and moisture using the analytical solutions obtained in the previous section.

Mesoscale vertical fluxes of momentum M_m^x and M_m^y, sensible heat H_m and moisture E_m are defined by Avissar & Chen (1993) and Lynn *et al* (1995) as

$$M_m^x = \overline{w'u'} \quad (3.68)$$

$$M_m^y = \overline{w'v'} \quad (3.69)$$

$$H_m = \overline{w'\theta'} \quad (3.70)$$

$$E_m = \overline{w'q'} \quad (3.71)$$

where the over-bar represents (horizontal) domain average, and θ' is related to buoyancy b' in the following way

$$\theta' = \frac{\theta_0}{g}b'$$

In the frequency domain, this relation is

$$dZ_\theta = \frac{\theta_0}{g} dZ_b$$

Using the analytical solution of dZ's given in section 3.3.3, these domain averaged primed terms can be replaced by the ensemble mean in the frequency domain (k_1, k_2) using Eqs. (3.54) through (3.57),

$$\begin{aligned} M_m^x(z,t) &= \int_{-\infty}^{\infty}\int_{-\infty}^{\infty} \mathrm{E}[dZ_w(k_1,k_2;z,t)dZ_u^*(k_1,k_2;z,t)] \\ &= \int_{-\infty}^{\infty}\int_{-\infty}^{\infty} \mid \Pi_w(k_1,k_2;z,t)\Pi_u^*(k_1,k_2;z,t) \mid \sigma_Q^2 S_Q(k_1,k_2)dk_1dk_2 \end{aligned} \tag{3.72}$$

$$\begin{aligned} M_m^y(z,t) &= \int_{-\infty}^{\infty}\int_{-\infty}^{\infty} \mathrm{E}[dZ_w(k_1,k_2;z,t)dZ_v^*(k_1,k_2;z,t)] \\ &= \int_{-\infty}^{\infty}\int_{-\infty}^{\infty} \mid \Pi_w(k_1,k_2;z,t)\Pi_v^*(k_1,k_2;z,t) \mid \sigma_Q^2 S_Q(k_1,k_2)dk_1dk_2 \end{aligned} \tag{3.73}$$

$$\begin{aligned} H_m(z,t) &= \int_{-\infty}^{\infty}\int_{-\infty}^{\infty} \mathrm{E}[dZ_w(k_1,k_2;z,t)dZ_\theta^*(k_1,k_2;z,t)] \\ &= \int_{-\infty}^{\infty}\int_{-\infty}^{\infty} \mid \Pi_w(k_1,k_2;z,t)\Pi_\theta^*(k_1,k_2;z,t) \mid \sigma_Q^2 S_Q(k_1,k_2)dk_1dk_2 \end{aligned} \tag{3.74}$$

$$\begin{aligned} E_m(z,t) &= \int_{-\infty}^{\infty}\int_{-\infty}^{\infty} \mathrm{E}[dZ_w(k_1,k_2;z,t)dZ_q^*(k_1,k_2;z,t)] \\ &= \{\int_{-\infty}^{\infty}\int_{-\infty}^{\infty} \mid \Pi_w(k_1,k_2;z,t)\Pi_q^*(k_1,k_2;z,t) \mid \sigma_Q^2 S_Q(k_1,k_2)dk_1dk_2\}\frac{d\bar{q}(z)}{dz} \end{aligned} \tag{3.75}$$

3.6.1 Momentum Fluxes

It has already been found using a 2D model, Dalu & Pielke (1993), that mesoscale momentum flux is zero in the absence of synoptic wind. Our 3D linear stochastic model also predicts a zero momentum flux in absence of synoptic wind. However, in a presence of the moderate synoptic wind u_0 our 3D model predicts that the mesoscale scale momentum fluxes will no longer be zero. The vertical structure of the momentum fluxes M_m^x and M_m^y in the neutral atmosphere ($N = 0$) are computed from Eq. (3.72) and (3.73) and plotted in Figure 3-

7(a). We note that the momentum flux associated with the horizontal wind in the direction of synoptic wind u_0 is zero. The non-zero momentum flux is due to the horizontal wind perpendicular to the direction of the synoptic wind. This property of momentum flux is fundamentally different from that of momentum flux (if any) predicted by 2D models. Given a reasonable value of $\sigma_H \simeq 50$ W m^{-2} (see Figure 4 of Lynn *et al*, 1995), M_m^y is on the order of 0.2 m^2 s^{-2} $= 8 \times 10^{-5} \times 50^2$, considerably larger than the typical value of the turbulent momentum flux (0.05 m^2 s^{-2}) according to Stull (1988). This significant difference between the mesoscale momentum flux and the turbulent momentum flux indicates that the transport of momentum from the synoptic flow to the locally generated mesoscale flow could be much stronger than that due to the surface friction. The evident mesoscale momentum flux also sheds some light on the interaction between the circulation at large scale and the organized flow at mesoscale. Figure 3-7(b) shows that the strongest mesoscale momentum transport occurs in the afternoon, about 9 hrs after sunrise. In the lower atmosphere, the momentum flux is downward (negative) while above certain altitude it becomes upward (positive) as shown in Figure 3-7.

Based on the previous discussion, strong synoptic wind will eventually eliminate the flow structure, and consequently the momentum flux. Therefore we expect the maximum momentum flux should be associate with a moderate value of the synoptic wind. The dependence of M_m^y on u_0 is plotted in Figure 3-8. M_m^y increases with the synoptic wind up to $u_0 \simeq 0.5$ m s^{-1}, then decreases at a slower rate.

Prediction of the momentum flux demonstrates one of the advantages of the 3D model. The existing 2D linear models may not be able to predict the existence of the momentum flux even when the synoptic wind factor is included in the governing equations because the momentum flux is caused by the wind component perpendicular to the synoptic wind. Another implication of this behavior is that prediction of momentum flux (if any) by 2D models may result from the assumption of 2D flow configuration (always 3D in the real world), rather than from the underlying physical mechanism of the processes.

3.6.2 Heat Flux

The vertical distribution of the mesoscale heat flux H_m is plotted in Figure 3-9(a) in the case of neutral stability and zero-synoptic wind. It can be seen that H_m could be as large as the turbulent heat flux H_t at the surface. Using the same value of σ_H as above, the maximum mesoscale heat flux H_m from Figure 3-9(b) is about 150 W m^{-2} = $50^2 \times 0.06$ which is comparable to the typical turbulent heat flux in the boundary layer. Figure 3-9(b) shows that the maximum H_m occurs at 3:00pm.

Synoptic wind strongly inhibits the mesoscale transport of heat away from the surface. Under the condition of slight synoptic wind ($u_0 = 1$ m s^{-1}) H_m will decrease by a factor of ten (see Figure 3-11(a)). Friction plays a key role in determining the structure and timing of H_m. Without friction H_m will be positive (upward transport of heat) until 9:00pm. Then H_m becomes negative up to 6:00am (sunrise) the next day. During this period of time, a downward transport of heat (non-physical) is associated with the flow. This is due to the fact that there is no heat sink in the atmosphere so that the heat released from the surface accumulates.

The qualitative properties of H_m are also consistent with the numerical simulations of Lynn *et al* (1995) such as the timing of the peak H_m and the altitude at which H_m reaches maximum. It should not be surprising to see the discrepancies in the magnitude of H_m because different land surface conditions and different parameters, such as Rayleigh friction coefficient α, are used.

3.6.3 Moisture Flux

Equating the expression within the brackets on the right hand side of (3.75) to the mesoscale moisture diffusion coefficient $-D_m(z,t)$, the mesoscale moisture flux E_m can be expressed as

$$E_m = -D_m(z,t)\frac{d\bar{q}(z)}{dz} \tag{3.76}$$

Our 3D linear theory predicts that the mesoscale moisture flux is proportional to the gradient of the mean moisture distribution. This expression is formally similar to the turbulent

moisture flux where the diffusion coefficient is due to the turbulent nature of the flow. However, the turbulent diffusion coefficient has to be determined from either measurements or numerical simulations because no analytical solution of turbulent flow has been found so far. The mesoscale moisture diffusion coefficient D_m is obtained analytically under the linearity assumption.

The vertical structure and the $z-t$ distribution of D_m is computed under the conditions of neutral stratification, zero-synoptic wind are illustrated in Figure 3-10(a) and Figure 3-10(b), respectively. The impact of synoptic wind on D_m is even stronger than that on H_m discussed previously. As the synoptic wind u_0 increases from 0 to 1 m s^{-1}, D_m is reduced by a factor of 25 (see Figure 3-11(b)). Notice that the maximum D_m occurs at a level which is the same as that of vertical velocity (Figure 3-1(c)), but different from that of H_m (Figure 3-9(a)). This is due to the fact that water vapor in our linear theory is a passive tracer. Hence water vapor basically follows the circulation patterns characterized by the distribution of vertical velocity, σ_w. On the other hand, vertical transport of heat is determined jointly by the diabatic heating source Q and the vertical velocity w. That is why the structures of vertical transport of heat and moisture are not identical. H_m depends in a nonlinear way on the mean potential temperature profile characterized by N, while D_m is independent of the mean profile of moisture, $\bar{q}(z)$, shown in Eq.(3.76).

Two main assumptions are inherent in deriving E_m in Eq.(3.76): no source of moisture (e.g. soil evaporation) in the atmosphere and no precipitation by condensation. Both of them are the direct consequences of the linearization of the water balance described by Eq. (3.60). Therefore this linear theory is unable to deal with the formation of cloud and rainfall which inevitably involves nonlinear analysis.

3.7 Summary

In this chapter a three dimensional stochastic linear theory of mesoscale circulation induced by thermal heterogeneity of the land surface is developed. The equations of atmospheric flow are formulated as a set of linear stochastic partial differential equations (SPDE's) driven by

randomly variable diabatic heating due to turbulent sensible heat flux from the surface. The SPDE's have been solved analytically. The major results are summarized as follows.

- The intensity of the thermally-induced mesoscale circulation is shown to be proportional to the standard deviation of the turbulent sensible heat flux at the surface. In the lower atmosphere the thermal variability of landscape at smaller length scales is more efficient in triggering convection, while at higher altitudes the atmospheric dynamics are more sensitive to thermal forcing at longer length scales. The atmosphere from bottom to top behaves as a low pass filter to the thermal variability of the landscape.

- Mesoscale fluxes of momentum, heat and moisture are found to be proportional to the variance of the turbulent sensible heat flux at the surface.

- The mesoscale momentum flux is insignificant in the absence of synoptic wind. A non-zero momentum flux is associated with the presence of synoptic wind. It increases as the synoptic wind goes from zero up to a rather small value (~ 0.5 m s^{-1}), and then decreases at a slower rate. Only the flow perpendicular the direction of synoptic wind contributes to this momentum flux. This is the reason why 2D linear models may not be able to predict a mesoscale momentum flux.

- That mesoscale heat flux, according to this linear theory, could be comparable to the surface turbulent sensible flux under conditions of small synoptic wind and neutral stratification.

- The moisture flux predicted by this 3D linear model is proportional to the vertical gradient of mean moisture profile. The mesoscale diffusion coefficient follows the structure of flow closely since the moisture is treated as a passive tracer.

- Stable stratification and synoptic wind strongly inhibit the development of the thermally-induced mesoscale circulation, hence reduce drastically the associated mesoscale transport of momentum, heat and moisture. Our results indicate that mesoscale fluxes, in this linear framework, are important only in the environments with neutral stratification and very weak synoptic wind.

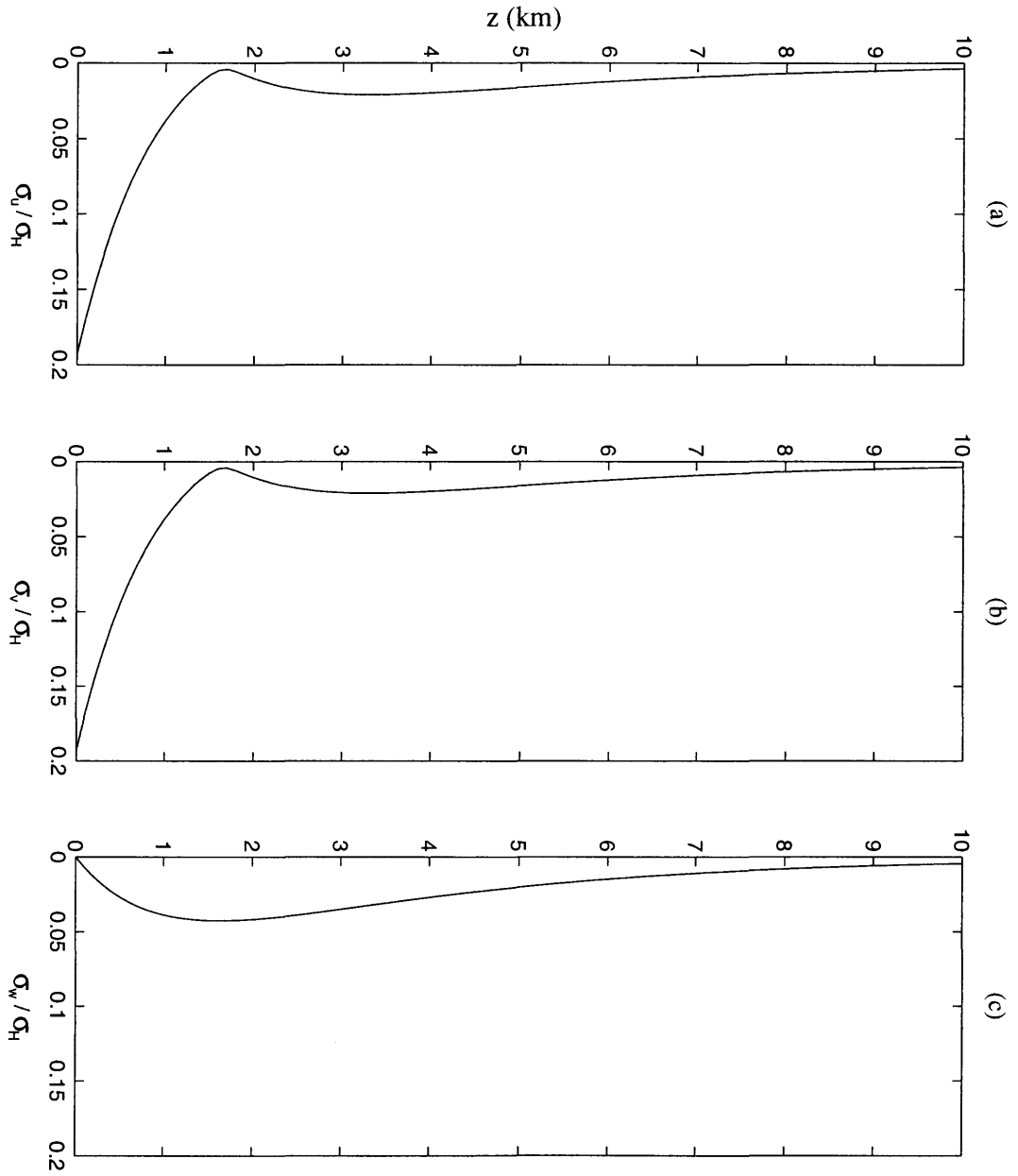

Figure 3-1: Vertical profiles of standard deviation of wind velocities (a) σ_u, (b) σ_v, and (c) σ_w (m s^{-1}) normalized by σ_H (W m^{-2}) in the case of $N = 0$, $u_0 = 0$ and $\alpha = 1.2\Omega$ at t=3:00pm local time.

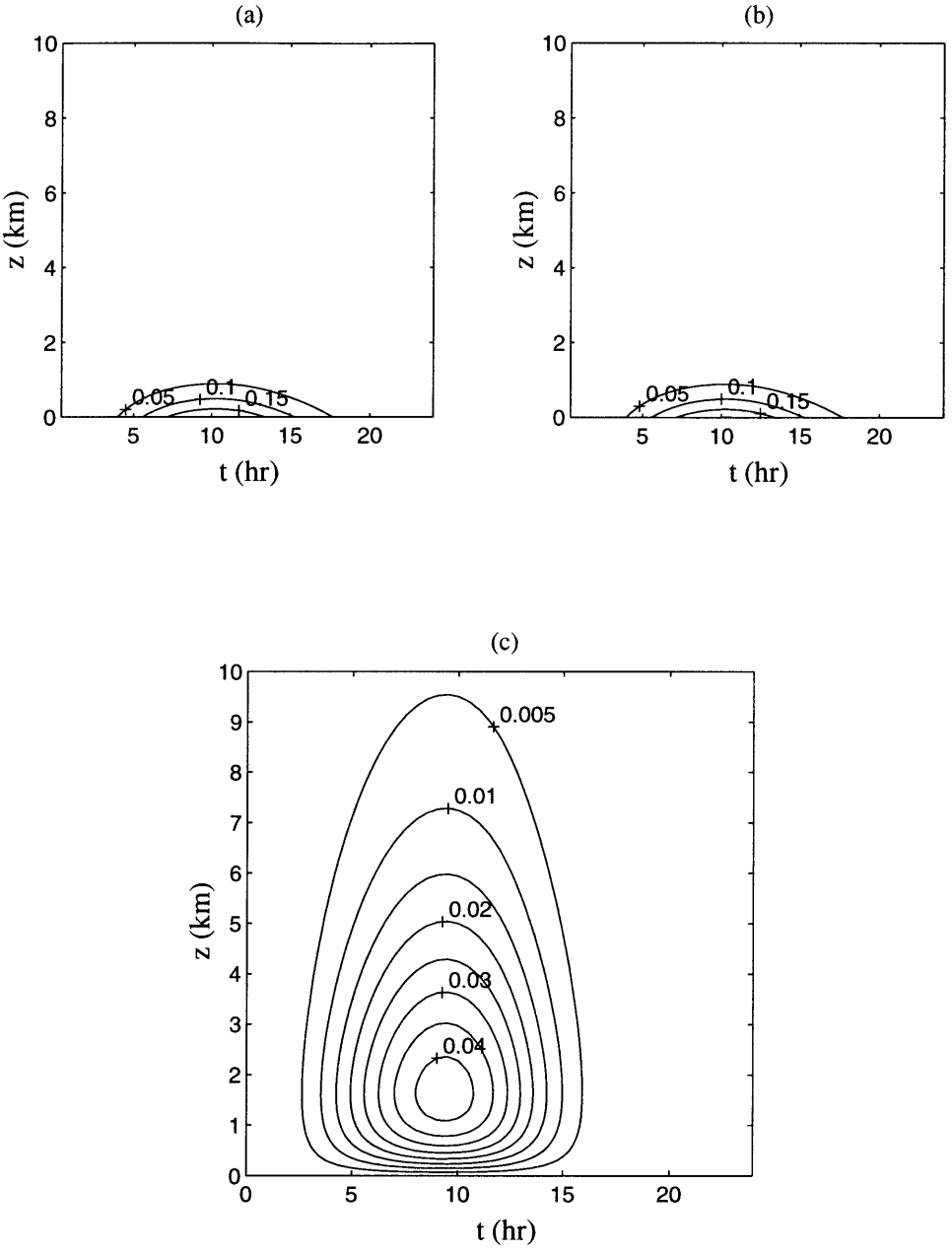

Figure 3-2: z - t distribution of (a) σ_u/σ_H, (b) σ_v/σ_H, and (c) σ_w/σ_H with $N = 0$, $u_0 = 0$ and $\alpha = 1.2\Omega$. t is the time after sunrise.

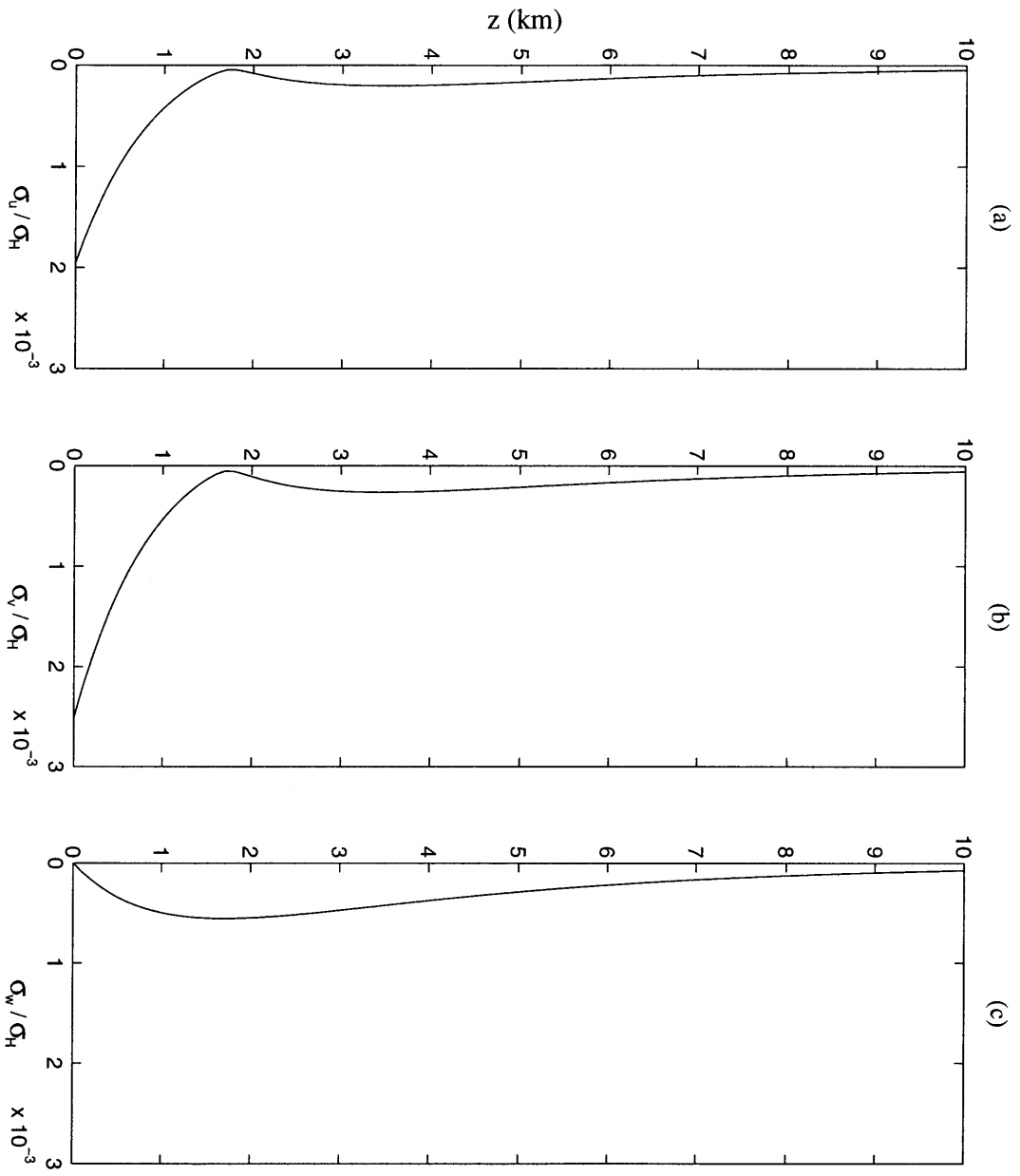

Figure 3-3: Same as Figure 3-1 except $u_0 = 5$ m s^{-1}

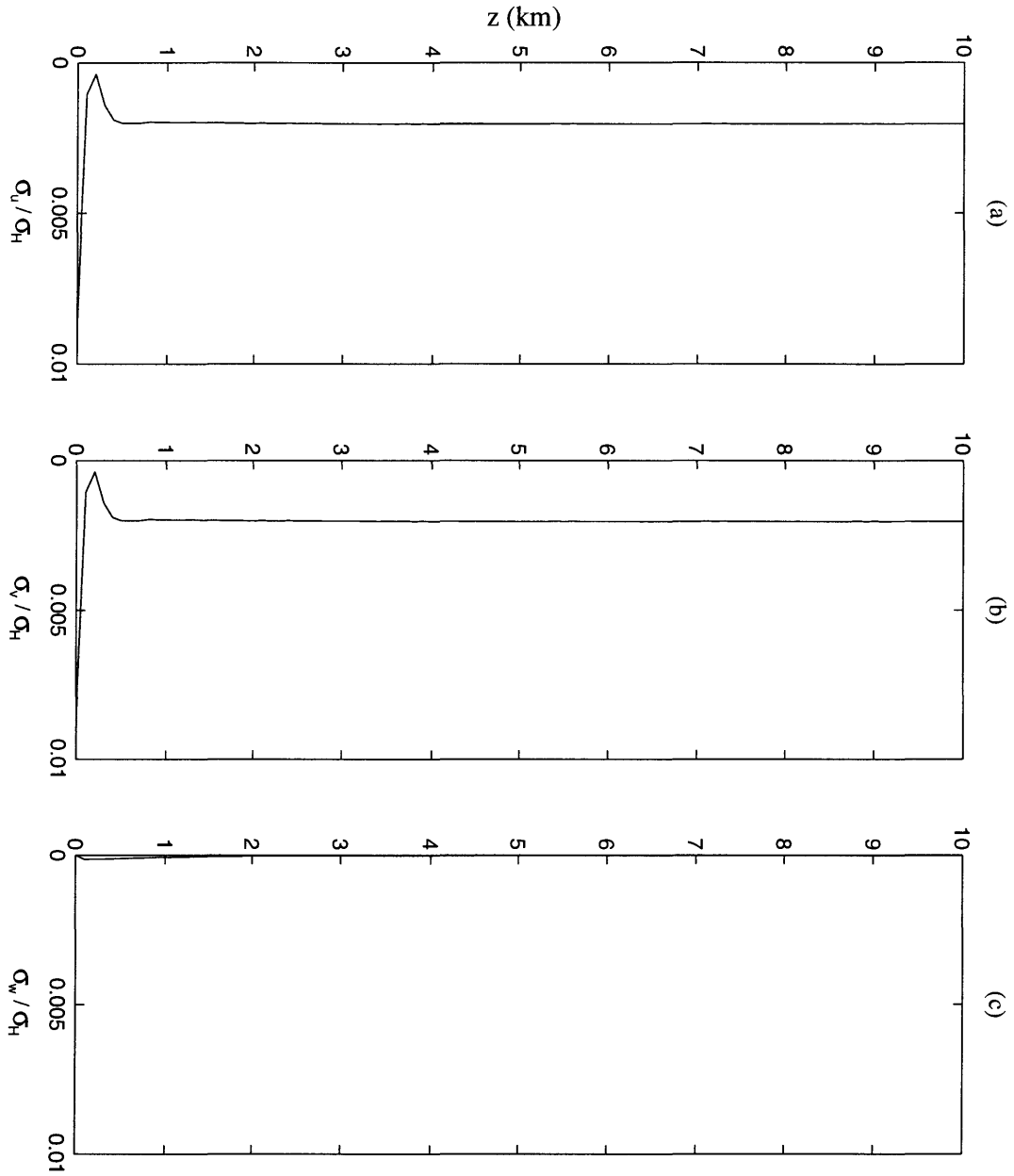

Figure 3-4: Same as Figure 3-1 except $N = 10^{-2}\mathrm{s}^{-1}$

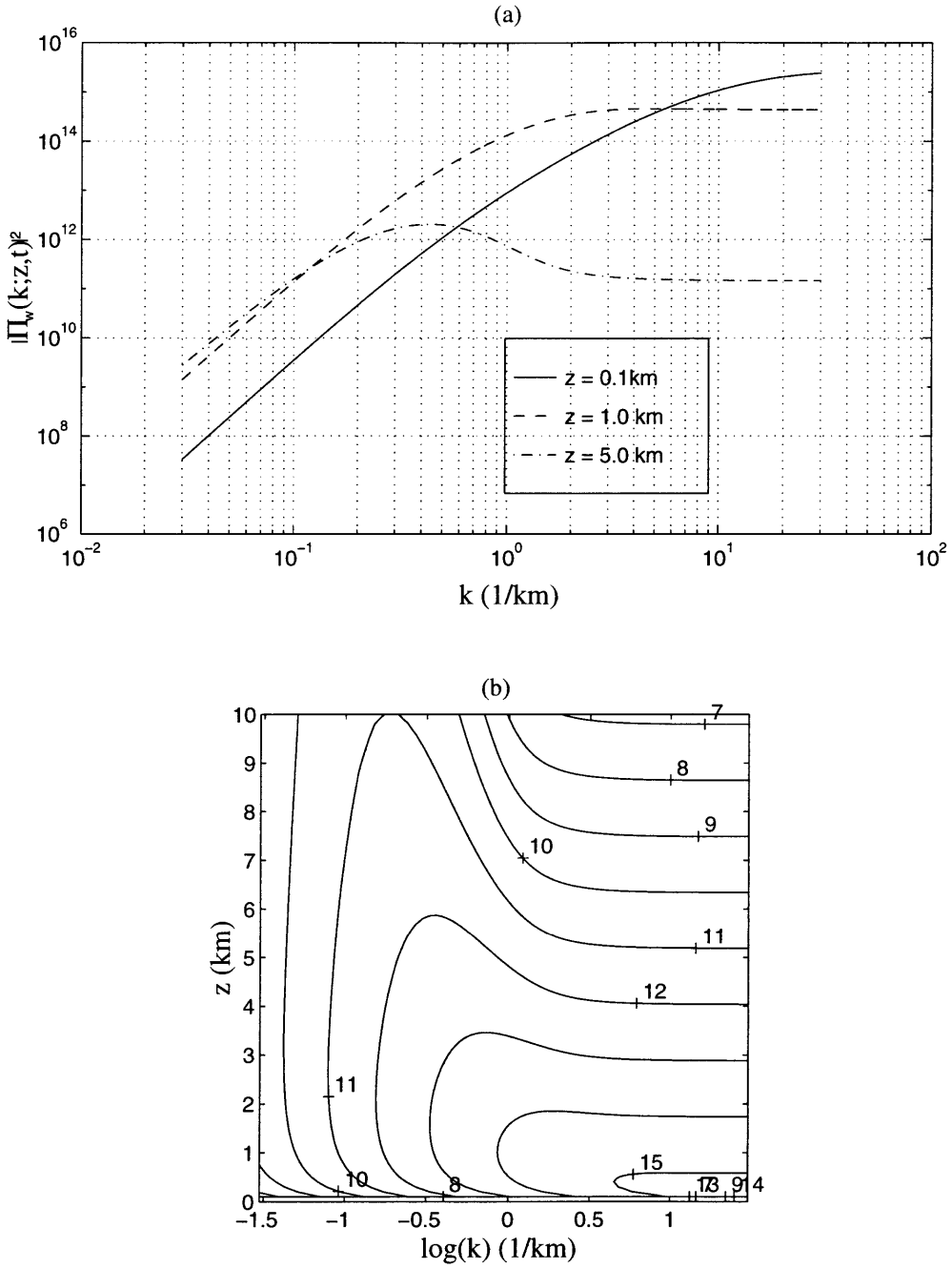

Figure 3-5: (a) k dependence of $\mid \Pi_w(k;z,t) \mid^2$ at z = 0.1, 1.0, and 5.0 km altitude, (b) $z - \log k$ distribution of $\log(\mid \Pi_w \mid^2)$, for $N = 0$, $u_0 = 0$ and $\alpha = 1.2\Omega$ at t=3:00pm.

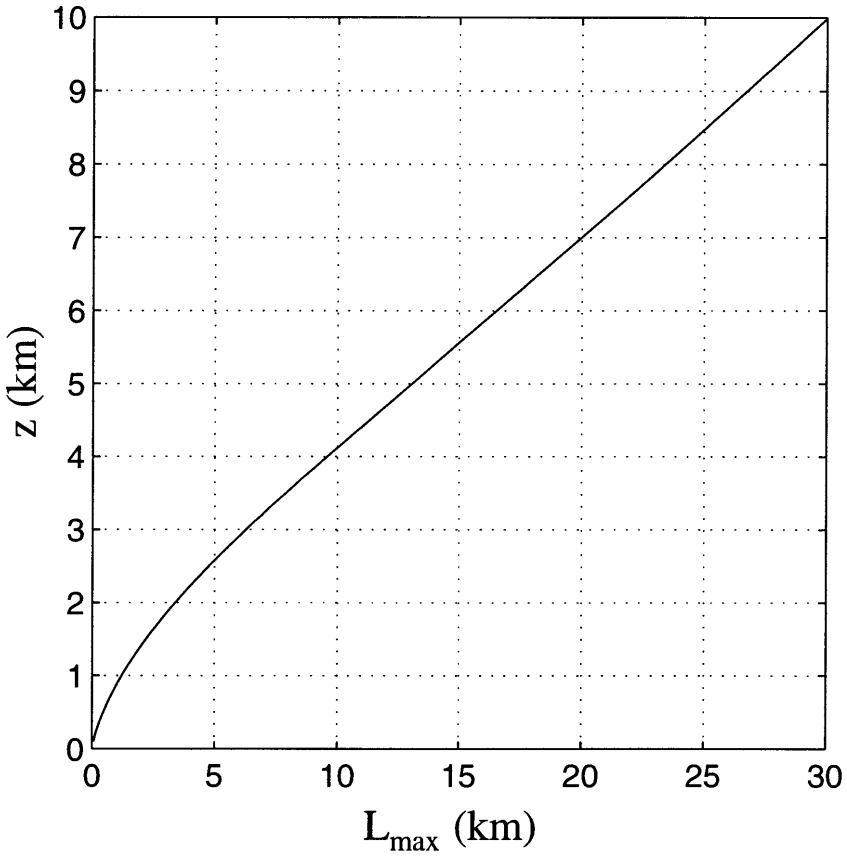

Figure 3-6: $L_{max} = 2\pi/k_{max}$, where k_{max} is the wave number at which $\mid \Pi_w \mid^2$ in Figure 3-5 reaches the maximum.

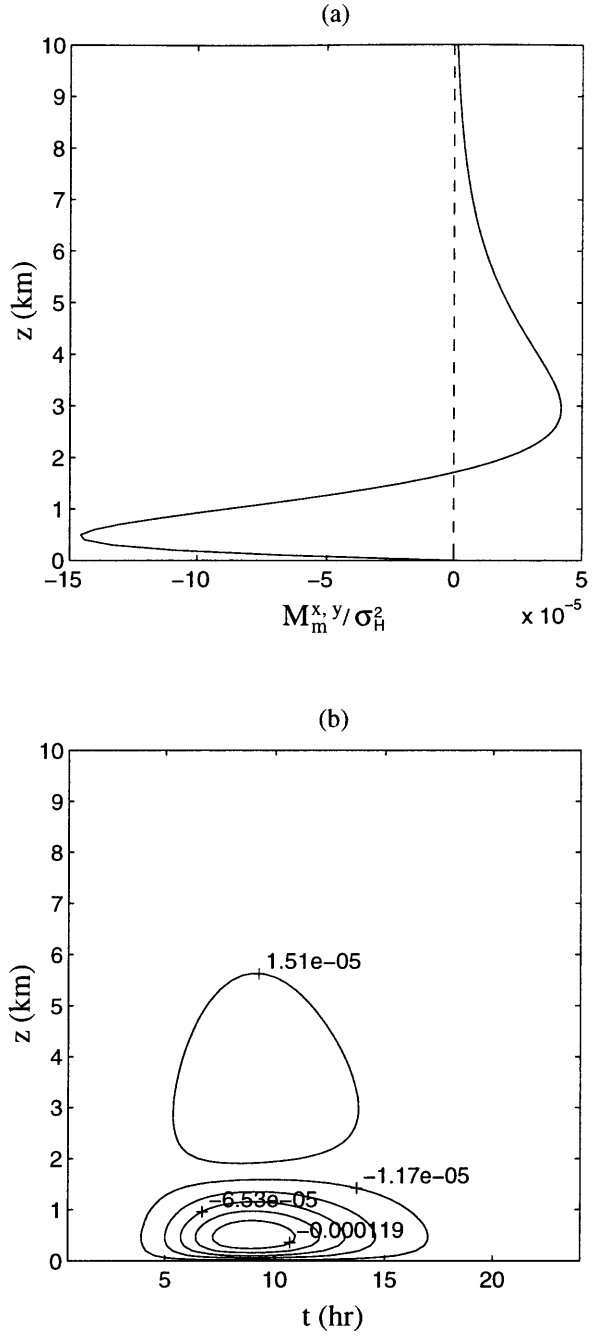

Figure 3-7: (a) Vertical profiles of Momentum fluxes M_m^x/σ_H^2 (dash-line) and M_m^y/σ_H^2 (solid-line) at t=3:00pm, (b) z - t distribution of M_m^y/σ_H^2 with $u_0 = 1$ m s^{-1}, and $\alpha = 1.2\Omega$. t is the time after sunrise (6:00am).

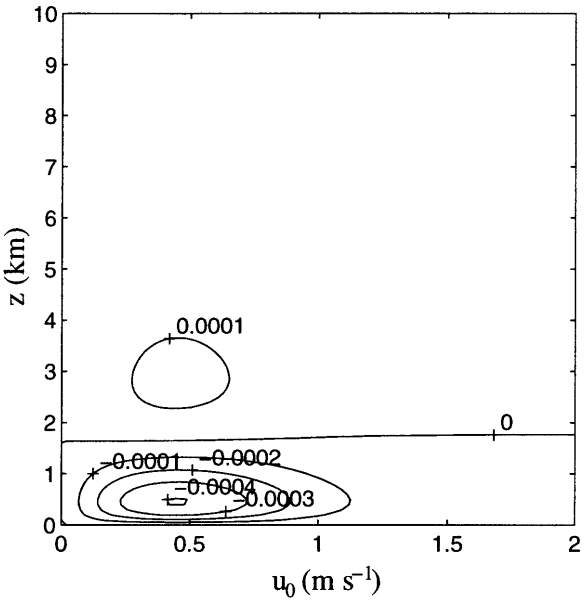

Figure 3-8: Vertical distribution of momentum flux M_m^y/σ_H^2 varying with synoptic wind u_0 where $N = 0, \alpha = 1.2\Omega$ at 3:00pm, or 9 hrs after sunrise.

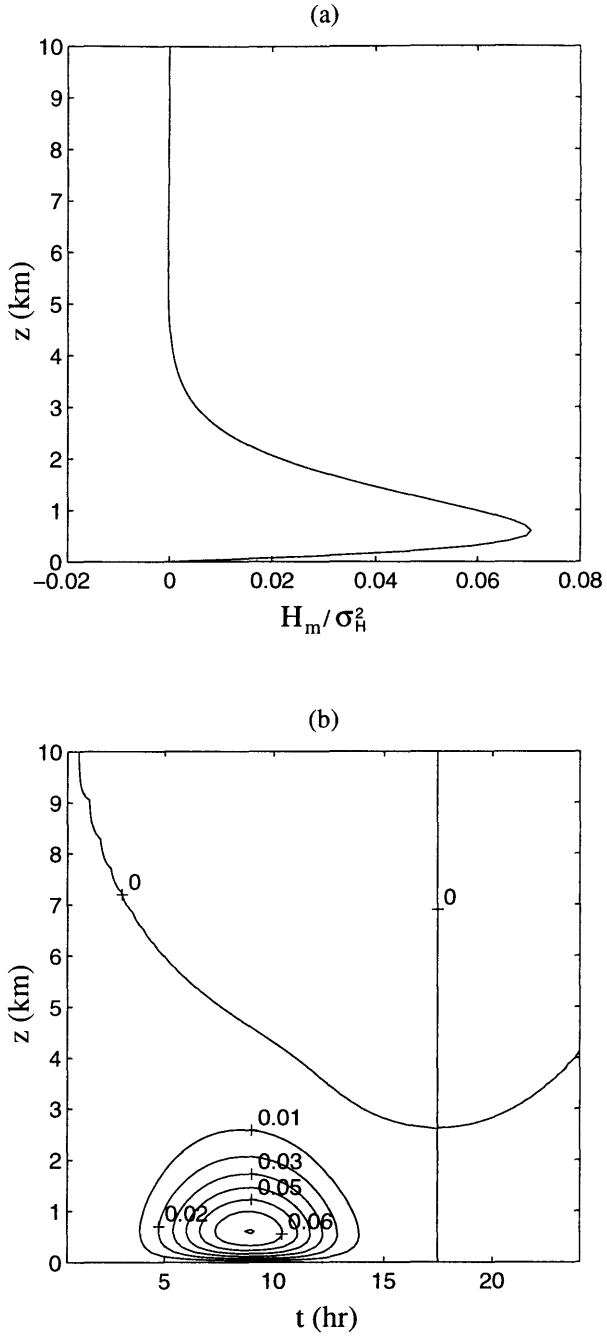

Figure 3-9: (a) Vertical profile of heat flux H_m/σ_H^2 at t=3:00pm, (b) z - t distribution of H_m/σ_H^2 in the case of $N = 0$, $u_0 = 0$ and $\alpha = 1.2\Omega$. t is the time after sunrise (6:00am).

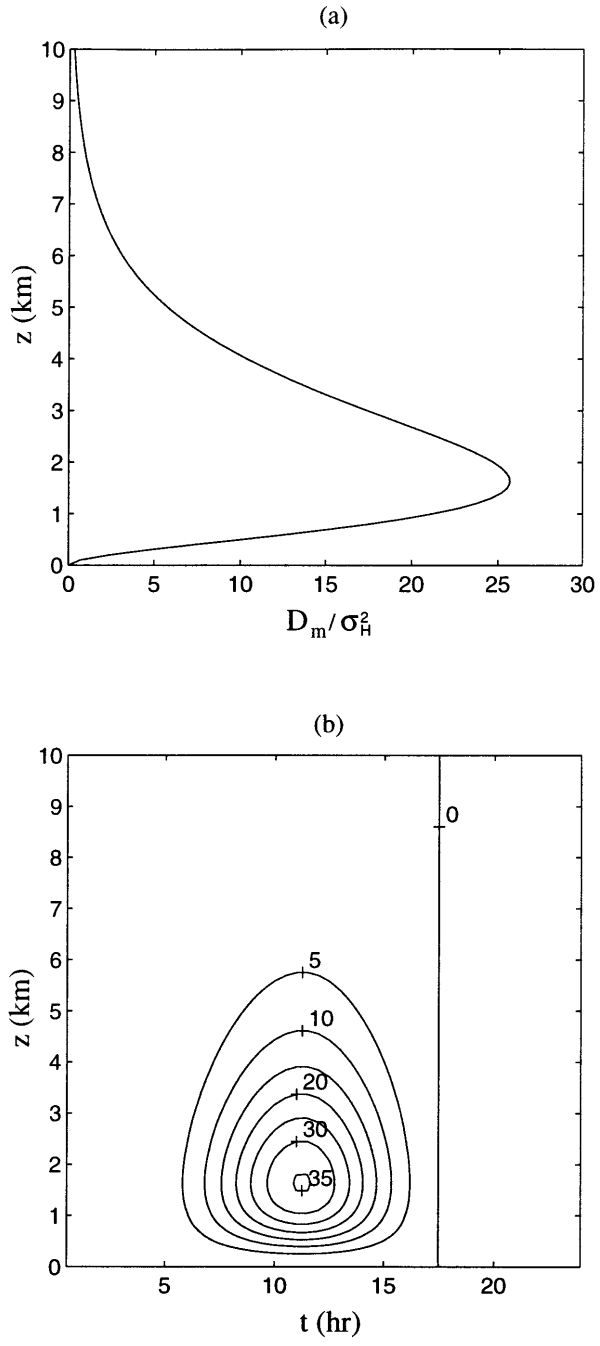

Figure 3-10: (a) Vertical profile of the mesoscale diffusion coefficient D_m/σ_H^2 at t=3:00pm, (b) z - t distribution of D_m/σ_H^2 in the case of $N = 0$, $u_0 = 0$ and $\alpha = 1.2\Omega$. t is the time after sunrise (6:00am).

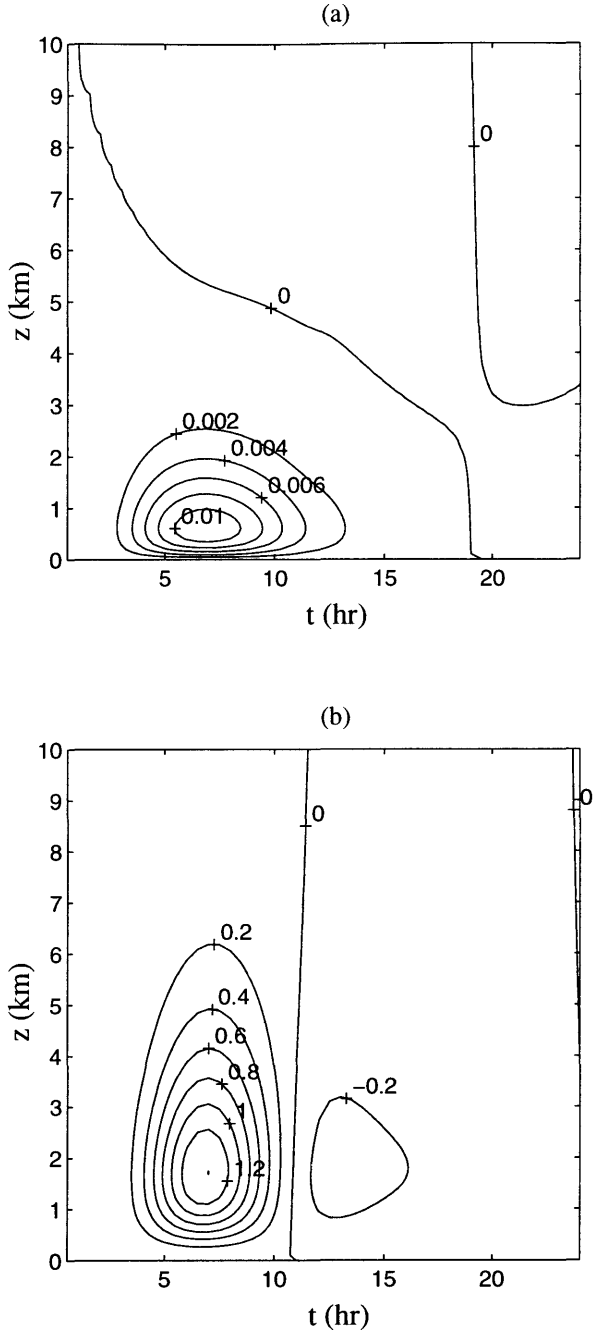

Figure 3-11: (a) Same as Figure 3-9(b) except $u_0 = 1$ m s^{-1}, (b) Same as Figure 3-10(b) except $u_0 = 1$ m s^{-1}

Chapter 4

Numerical Simulations of Thermally Induced Flow

4.1 Motivation

In Chapter 3, a stochastic linear model has been developed for the mesoscale circulation induced by the land surface thermal heterogeneity of random distribution. The accuracy of this linear theory in describing mesoscale circulation depends critically on relative magnitudes and the importance of omitted nonlinear components of the mesoscale system. Unfortunately, a general analytical approach for nonlinear analysis is not currently available. To further assess the importance of mesoscale circulation under the same random forcing, numerical simulations have been conducted using a nonlinear numerical mesoscale model.

An overview of the earlier works on this topic will be given first. Revisiting these previous results is helpful in highlighting the contribution of this work to the improvement of our knowledge on this topic.

4.2 A Brief Review

Voluminous literature has been devoted to the numerical modeling of the mesoscale atmospheric flow. A good source of references on this topic can be found in a monograph by

Pielke (1984). This short review only covers the numerical studies on the role of variable surface properties in the thermally induced mesoscale circulations in the last two decades.

Sea breeze is probably the strongest mesoscale atmospheric motion that differential heating can produce at a daily time scale. Huss & Feliks (1981) used a 2D model to study sea breeze driven by land-sea contrast under the condition of zero synoptic wind and stable stratification. Their simulations produce a maximum horizontal wind of 6 m s^{-1}, and a maximum vertical velocity of 5 cm s^{-1} over land. Ookouchi et al (1984) investigated the land breeze caused by soil moisture contrast using a 2D model. The environment is characterized by a slight synoptic wind of 0.5 m s^{-1} and a non-uniform stability (N being zero within the lowest layer of 1 km and $\sim 10^{-2}$ s^{-1} above). The maximum horizontal wind of 5 m s^{-1}, and maximum vertical speed of 20 cm s^{-1} were induced by 13°C temperature difference between the wet and dry land. Segal et al (1986) evaluate the impact of cloud shading (reducing solar radiation) on the thermally induced flow under weak synoptic wind of 0.5 m s^{-1} and stable stratification of N equal to $10^{-2}s^{-1}$. For a sensible heat flux difference of about 250 W m^{-2} over the land surface, significant flow with maximum horizontal wind of 4 m s^{-1}, and maximum vertical wind of 30 cm s^{-1} are observed in their 2D simulations.

During the last decade, increasing attention has been paid to the role of soil and vegetation over land on the development of mesoscale circulations. Mahfouf et al (1987) carried out 2D simulations of the flow induced by contrast in soil type and vegetation cover under a stable ($N \sim 10^{-2}$ s^{-1}) and zero synoptic wind condition. The sand-clay contrast in their simulation results in a maximum sensible heat flux difference of 400 W m^{-2}, leading to a maximum horizontal wind of 5 m s^{-1} and the maximum vertical wind of 10 cm s^{-1}. The bare soil-grass case produces a maximum sensible heat flux difference of 200 W m^{-2} that results in a maximum horizontal wind of 2.5 m s^{-1} and maximum vertical wind of 4 cm s^{-1}. Yan & Anthes (1988) performed a 2D numerical simulation of the mesoscale circulation induced by variable soil moisture assuming an alternating wet-dry strips. They simulate a horizontal wind as large as 10 m s^{-1} for the case of a 144 km dry strip surrounded by moist land, and the largest vertical wind speed of 56 cm s^{-1} in the case of alternating 96-km moist and dry bands. This work indicates that both intensity and spatial scale of the land surface hetero-

geneity play important roles in the generation and modification of mesoscale circulations. They also point out that the absence of large-scale flow favors the development of mesoscale circulation; a mean flow would likely weaken the mesoscale circulation and make the convective rainfall less likely. Segal et al (1988) performed a series of 2D numerical simulations of vegetation-bare soil contrast forced mesoscale flow induced by a vegetation and bare soil contrast assuming stable atmosphere ($N \sim 10^{-2}$ s^{-1}). For a surface temperature difference of 15 K across a distance of 3 km a maximum horizontal wind of 7 m s^{-1} and a maximum vertical wind of 53 cm s^{-1} are observed. While for a surface temperature difference of 5 K across a distance of 30 km the maximum horizontal wind and the maximum vertical wind are reduced to 2.8 m s^{-1} and 7 cm s^{-1}, respectively. They also found that the magnitude of the gradient of the surface temperature is the critical factor in the thermally induced flow.

Avissar & Pielke (1989) suggested that the effect of heterogeneous land surfaces should be parameterized in large scale atmospheric models. They proposed a scheme for parameterization of the subgrid-scale forcing of heterogeneous land surfaces (regrouped into two adjacent subgrid areas with contrasting thermal properties) using a 2D numerical model. Under the condition of synoptic wind of 0.5 m s^{-1} and stable stratification, a mesoscale flow as strong as sea breeze (maximum horizontal wind of 6 m s^{-1} and maximum vertical wind of 20 cm s^{-1}) may develop when strong contrasts in sensible heat flux ($\sim$ 350 W m^{-2}) are generated by the land surface heterogeneities. André et al (1990) showed that, in the tropics and midlatitudes, a horizontal gradient of less than about 10 W m^{-2} per 30 km has only minor influence on local wind patterns. With a gradient of 100 W m^{-2} per 30 km, significant effects are discernible from the statistical evaluation of observational data. A gradient of 1000 W m^{-2} per 30 km has been found to have a pronounced influence on local wind patterns. A numerical study by Xian & Pielke (1991) again show that the thermally driven flow is dominated by both intensity and length scale of the differential heating. They also conclude that a stable atmosphere is not a favorable environment for the development of a sea-breeze.

Pielke et al (1991) applied a 2D version of the RAMS model developed at Colorado State University to simulate the mesoscale heat flux associated with the nonhomogeneous surface

that was initialized with alternating land and water strips of widths ranging from 4 km to 96 km. No phase change of water was permitted. The mesoscale heat flux reaches a maximum of 200 - 300 W m^{-2} for 32, 64, and 96 km wide strip cases, significantly larger than the turbulent heat flux. They emphasize that the nonlinear advective effects should be incorporated in evaluating the contribution of the different spatial scales of the surface nonhomogeneity to the vertical mesoscale heat flux. Chen & Avissar (1994) also adopted the 2D version of the RAMS to compute mesoscale heat fluxes associated with flow induced by soil moisture discontinuities in the dry atmosphere. The wet-and-dry contrast of the land surface (maximum domain-averaged turbulent sensible heat flux of 250 W m^{-2}) induces a maximum mesoscale sensible heat flux of 100 W m^{-2}. They found that the mesoscale fluxes were weakened by synoptic winds but remained significant with moderate winds. It is worth noting that the mesoscale heat fluxes in these simulations decreased by a factor of two in the case of a random distribution of initial soil moisture over the six patches. They further argued that strong nonlinear relation exists between sharpness of the contrast and the flux intensity. Li & Avissar (1994) emphasized the nonlinearity of the relations between the land surface characteristics and the mesoscale fluxes. The statistics obtained from a large number of simulations using the model proposed by Avissar & Pielke (1989) indicate, for example, that the mesoscale latent heat flux is the most sensitive to spatial variability of the land surface. They suggested it is important to consider the spatial distribution of leaf area index, stomatal conductance, and surface roughness in vegetated areas, and soil-surface wetness and surface roughness in bare land in the parameterization of land surface processes in atmospheric models.

Among the early attempts of three-dimensional numerical modeling of mesoscale circulations, Pielke (1974) studied the sea breeze over south Florida, and Mahrer & Pielke (1977) investigated the mesoscale flow induced by the combined terrain and thermal forcing. Motivated by the satellite and aircraft observations of surface temperature over the irrigated crop areas of northeast Colorado, Segal et al (1989) carried out 3D simulation of the air motion induced by the contrast in the irrigated-dry land (resulting in a sensible heat flux difference of 200 W m^{-2}) in the stable atmosphere. A maximum horizontal wind of about 7 m s^{-1}

was observed when synoptic winds are absent. They suggest that the flow induced by the pure land surface heterogeneity may be difficult to resolve when moderate synoptic wind is present. Avissar & Chen (1993) performed 3D simulations of mesoscale kinetic energy and mesoscale fluxes induced by the landscape discontinuity for a stable atmosphere ($N \sim 10^{-2}$ s^{-1}) and a slight synoptic wind (0.5 m s^{-1}). A horizontal wind of 6 m s^{-1} and a vertical wind of 1 m s^{-1} were simulated. The mesoscale heat flux of 30 W m^{-2} is produced in response to turbulent sensible heat flux of 250 W m^{-2}. They argued that the impact of the synoptic wind was dependent on the distribution of the soil moisture at the ground surface, but in general strong synoptic wind would sway the mesoscale perturbation and reduce the intensity of the mesoscale circulation. The authors also suggested a nonlinear relationship between the patch size and the fluxes, up to a horizontal scale of approximately 100 km, supporting the previous study by the first author.

Lynn et al (1995a) conducted 3D simulations of mesoscale circulation in a stable atmosphere forced by a landscape covered with two kinds of contrasting patches in wetness. The resultant flow was comparable to a sea breeze. The mesoscale heat flux varied with the patch size with a maximum of 14 W m^{-2} corresponding to 90 km patches of fully saturated and completely dry soil, while the domain-averaged maximum turbulent sensible heat flux is about 40 W m^{-2}. They found the mesoscale heat flux increases with the patch size and difference in level of saturation. The simulation results also suggested that the the mesoscale fluxes were not sensitive on moderate synoptic wind, but sensitive to the spatial distribution of surface wetness. Hence, they argued it is necessary to parameterize mesoscale processes induced by landscape discontinuities in GCMs. Besides, the authors noted that in general mesoscale fluxes are smaller for 3D simulations than for 2D simulations. In a companion paper Lynn et al (1995b) proposed parameterizations of the mesoscale heat fluxes using similarity theory.

In summary, significant thermally induced mesoscale flow have been simulated in response to sharp contrast of landscape, due to discontinuities of soil moisture or vegetation cover, using numerical models. Both intensity and length scale of surface heating are shown to be important for the development of the mesoscale flow. The objective of this study is to assess

quantitatively the impact of random distribution of thermal properties of landscape on the mesoscale circulation.

4.3 Numerical Model

The numerical model used in this study is the updated three-dimensional CLARK model (version G2TC38) developed at NCAR. Detailed description of this model is given by Clark (1977) and Clark & Hall (1995), hence is not repeated here.

The model is nonhydrostatic and can be forced by a prescribed TSFH from the land surface. The atmosphere is assumed to be dry. Cyclic boundaries are used to simulate infinite domain conditions. The simulation domain is a 200 km $\times$ 200 km area. The horizontal resolution for the simulations described in this paper ranges between 5 and 10 km depending on the length scale of the prescribed forcing. The atmosphere is divided into 20 vertical levels with variable increments (see Table 4.1). Integration time step is 15 sec to ensure the stability of the numerical scheme. The total simulation time is 24 hrs. The design of the numerical experiments is described as follows.

4.3.1 Random Surface Forcing

To realistically represent the observed heterogenous land surface, we propose to model the turbulent sensible heat flux $H_s(x, y; t)$ over the surface as a homogeneous random field. Realizations of this random field can be simulated by sampling from the spectrum, and utilized as the input to the numerical CLARK model. The sensible heat flux is described by

$$H_s(x, y; t) = (H_0 + \sigma_H \hat{H}(x, y))I(t) \tag{4.1}$$

where H_0 is the domain-mean daily maximum turbulent sensible heat flux, σ_H is the corresponding standard deviation, and the random function $\hat{H}$ with zero mean and unit variance fully characterizes the spatial distribution of $H_s(x, y; t)$. According to many observations,

the time-varying behavior of turbulent heat flux follows closely the insolation curve $I(t)$

$$I(t) = \begin{cases} \sin(\frac{2\pi}{T_0}t) & , \quad 0 \leq t \leq T_0/2 \quad (\text{day} - \text{time}) \\ 0 & , \quad T_0/2 < t \leq T_0 \quad (\text{night}) \end{cases} \tag{4.2}$$

Statistically, $\hat{H}$ may be characterized by spectral density function or autocorrelation function (e.g. Yaglom, 1987). Two types of hypothetical distributions will be utilized in the numerical experiments : a banded white-noise spectral density function S_H and exponential correlation function R_H with correlation length of 10 km, 30 km, and 50 km. These values of correlation length are consistent with those estimated from **NDVI** data analysis conducted in Chapter 2. It can be shown that the spectrum corresponding to correlation function of the form (2.2) is similar to the spectrum corresponding to an exponential correlation whose length scale is defined in (2.3). But the latter has a much simplier functional form, hence is much easier to use. In practice random functions with exponential correlation proves to be the convenient approximations of a wide spectrum of observed random processes.

Banded White-noise Spectral Density Function Consider the situation where the land surface heterogeneity lacks dominant length scales. In this case, the variability of the TSHF at surface has uniform distribution over a certain range of length scales. This type of variability could be described by a banded white noise spectral density function. In the following simulations, we impose a low limit of 20 km and a high limit of 50 km on the length scale of the TSHF over the mesoscale simulation domain ($\sim$ 200 km). Hence, S_H is constant over the wave number window

$$S_H(k_1, k_2) = \begin{cases} \frac{1}{4(k_b - k_a)^2} & , \quad k_a < \mid k_1 \mid, \mid k_2 \mid < k_b \\ 0 & , \quad \text{otherwise} \end{cases} \tag{4.3}$$

where k_1, k_2, k_a and k_b are wave number with

$$k_a = \frac{2\pi}{50}\text{km}^{-1}, \qquad k_b = \frac{2\pi}{20}\text{km}^{-1}$$

A realization of the random field of H_s with S_H specified in (4.3) is illustrated in Figure 4-1.

Exponential Autocorrelation Function When the random field H_s has a dominant length scale L, an exponential autocorrelation function R_H may be used to characterize it statistically

$$R_H(x,y) = \exp(-\frac{\sqrt{x^2+y^2}}{L}) \tag{4.4}$$

The spectral density function (Fourier transform of R_H) is shown to be

$$S_H(k_1,k_2) = \frac{1}{2\pi L}\frac{1}{[k_0^2+k^2]^{\frac{3}{2}}} \tag{4.5}$$

where $k_0 = 1/L$, $k^2 = k_1^2 + k_2^2$.

The realizations of this type of random field H_s with correlation length scales $L = 10, 30$ and 50 km are plotted in Figure 4-2, 4-3 and 4-4, respectively.

In the numerical simulations, H_0 is taken to be 200 W m^{-2} and σ_H to be 50 W m^{-2}, a value somewhat larger than but still on the same order of magnitude as that ($\sim$ 25 W m^{-2}) estimated over the three regions considered in Chapter 2. These values lead to a range of H_s variability on the order of 200 W m^{-2}, fairly close to the observed variability in surface heating for other areas (Sun & Mahrt, 1994; Doran et al, 1995).

4.3.2 Synoptic Conditions

The parameters characterizing the synoptic environment in the numerical model for a dry atmosphere are atmospheric stability N (Brunt-Väisälä frequency) and synoptic wind u_0, both taken to be constant in time. Three vertical profiles of N are tested: neutral stratification ($N = 0$), stable stratification ($N = 10^{-2}$ s^{-1}), and neutral within the depth of the boundary layer ($\sim$ 1 km) and stable above that level. Three values of u_0 are used in the different simulations: 0, 5, and 10 m s^{-1}. The objective is to identify the condition(s) under which significant mesoscale circulation and fluxes may result.

4.4 Results and Discussions

Some fifty simulations have been performed to evaluate the impact of length scale of the forcing, atmospheric stability, and synoptic wind on the mesoscale circulation and fluxes. The mesoscale circulation can be quantified by the standard deviations, σ_u, σ_v and σ_w of the random fields of the three wind components u, v and w, over the horizontal domain.

$$\begin{aligned} \sigma_u^2(z,t) &= \overline{u'^2} \\ \sigma_v^2(z,t) &= \overline{v'^2} \\ \sigma_w^2(z,t) &= \overline{w'^2} \end{aligned}$$

The mesoscale momentum fluxes M^x, M^y, and heat flux H can be expressed as the cross-covariance (eddy-correlation) between the vertical velocity and the pertinent variables,

$$\begin{aligned} M^x(z,t) &= \overline{w'u'} \\ M^y(z,t) &= \overline{w'v'} \\ H(z,t) &= \rho C_p \overline{w'\theta'} \end{aligned}$$

where ρ is the (constant) air density (~ 1 kg m^{-3}); C_p, heat capacity of the air at constant pressure. The primed terms stand for the perturbations around the (horizontal) domain means.

4.4.1 Effect of the Length Scale of the Forcing

The linear theory presented in Chapter 3 suggests that neutral stratification and zero synoptic wind are the most favorable conditions for mesoscale circulation to develop. We will start by investigating the impact of the length scale of the forcing under these conditions.

Banded White-noise Forcing The space-time distributions of the standard deviations of the resultant winds and the mesoscale momentum and heat fluxes are presented in Figure 4-5. The maximum horizontal wind is about 10 m s^{-1}, and the maximum vertical wind

about 3 m s^{-1}, stronger than a sea breeze. The strongest thermal flow is observed around 3:00pm. The circulation cells penetrate as high as 5 km, far beyond the depth of the observed planetary boundary layer (on the order of 1 km).

The maximum (downward) momentum fluxes, ~ 0.8 m^2 s^{-2}, are one order of magnitude greater than the turbulent momentum fluxes, which are usually on the order of 0.05 m^2 s^{-2} (e.g. Stull, 1988), in the boundary layer. Nevertheless, the maximum heat flux, $\sim$ 20 W m^{-2}, is one order of magnitude smaller than the turbulent heat flux, $\sim$ 200 W m^{-2}, that has been used to force the circulation. Thus, the mesoscale circulation is not efficient in terms of heat transport.

Exponential Autocorrelation Function Forcing The statistics of the thermal flow and the fluxes computed from the simulations under exponential autocorrelation forcing with correlation length scales of 10, 30, and 50 km are illustrated in Figure 4-6, Figure 4-7, and Figure 4-8, respectively. Significant thermal flow is developed under these types of forcing with maximum horizontal wind of about 10 m s^{-1}, and maximum vertical wind about 2 m s^{-1}. The mesoscale momentum fluxes, ~ 0.7 m^2 s^{-2}, are found to be downward and much stronger than the corresponding turbulent flux. The mesoscale heat flux, $\sim$ 20 W m^{-2}, is substantially weaker than turbulent heat flux within the boundary layer. There are no significant differences in the results among the three cases of different correlation length scales.

Discussion Banded white-noise forcing has a flat spectral density function over a limited wave-number window. Exponential autocorrelation forcings have spectral density functions of power-law with exponent -2 at small length scales and flat at large length scales. Although the functional forms of these two kinds of forcings are different, comparing Figure 4-5 with Figure 4-6, 4-7 and 4-8 reveals that they produce almost identical standard deviations of horizontal winds, momentum and heat fluxes. The exponential autocorrelation forcings (Figure 4-6, 4-7 and 4-8) result in slightly smaller standard deviation of vertical velocity. The similar behavior of the system when forced by banded white noise and exponentially correlated noise suggests that surface heterogeneities with very large length scales are not effective in forcing

mesoscale circulations. Forcings with length scales around tens of kilometers are effective in forcing mesoscale circulations.

Simulations under banded white-noise forcings with length scales of 5 - 15 km and 50 - 80 km were also performed in the case of neutral stratification and zero synoptic wind. The results (not shown by figures) indicate that smaller length scale forcing (with the same standard deviation) is more effective in inducing vertical velocity and momentum fluxes, and larger length scale forcing is more effective in inducing horizontal velocities and heat flux. It is also found that the cross-correlations (covariance normalized by the corresponding standard deviations) of the vertical wind component with potential temperature, and with horizontal wind components are not very sensitive to the length scales of the forcing. With increasing length scales of the forcing, the decrease in the standard deviation of vertical velocity is greater than the increase in the standard deviations of horizontal velocities, leading to a decrease in momentum fluxes. On the other hand, the decrease in the standard deviation of the vertical velocity is smaller than the increase in the standard deviation of the potential temperature, leading to an increase in the heat flux. We note that the mesoscale fluxes of momentum and heat plateau at a certain length scale since there is no significant difference between the results corresponding to 20 - 50 km and 50 - 80 km banded white-noise forcings.

The inherent length scale of the atmospheric flow system at mesoscales may be defined as the wave number (inversely proportional to the length scale) at which the amplitude of the frequency response function of the mesoscale circulation attains its maximum. Significant flow is expected to be induced when the length scales of the surface forcing are around the inherent length scale of the atmosphere. The numerical simulations demonstrate that the banded white noise forcing with the length scale (wave number) window of 20 - 50 km is as effective as the exponential correlation forcings with length scale window of $0 - \infty$ km in driving mesoscale circulations. This finding suggests that the inherent length scale of this mesoscale atmospheric flow is likely to be around tens of kilometers.

4.4.2 Effect of Atmospheric Stability

Constant N The results of the mesoscale flow and fluxes when the atmosphere is stable are presented in Figure 4-9. The maximum horizontal wind in this case is only about 2 m s^{-1}, maximum vertical wind about 0.25 m s^{-1}. Maximum heat flux becomes insignificant ($\sim$ 2 W m^{-2}). Momentum fluxes ($\sim$ 0.025 m^2 s^{-2}) are of the same order as turbulent flux. The mesoscale circulation is confined within the lowest one kilometer layer.

The numerical simulation indicates that the stability substantially reduced the thermal flow. Compared to the neutral atmosphere, the horizontal wind is reduced by a factor of five, while the vertical motion is reduced by a factor of ten in a stable atmosphere. The mesoscale fluxes decrease by one order of magnitude. Therefore, the thermal flow is probably difficult to detect within the boundary layer since it is likely to be masked by turbulence.

Varying N Because the boundary layer tends to be well-mixed due to strong turbulent flow, the stratification is usually close to neutral within the depth of the boundary layer ($\sim$ 1 km) and stable upward. The results under this condition are presented in Figure 4-10. As can be expected, the resultant flow and fluxes turn out to be somewhere between the cases of neutral and stable stratifications.

The maximum horizontal wind of 6 m s^{-1}, and maximum vertical wind of 1 m s^{-1}, comparable to sea breeze, are observed in the simulation. Momentum fluxes, $\sim$ 0.4 m^2 s^{-2}, are still significant, while heat flux, $\sim$ 10 W m^{-2}, is not. Figure 4-10 also illustrates that the penetration depth of the mesoscale flow is close to the depth of the boundary layer. Hence, even though the atmosphere is neutral in the lowest 1 km layer near land surface, it is probably not easy to separate the signals of mesoscale circulation from that due to turbulence.

Discussion Stability plays a more important role than does the length scale of forcing as predicted by this numerical model. The presence of stable stratification strongly inhibits the development of free convection in dry atmosphere. Relatively weak mesoscale circulation is likely to be masked by the turbulent flow within the boundary layer although it could make

appreciable contribution to the total momentum fluxes.

4.4.3 Effect of Synoptic Wind

Figure 4-11 and Figure 4-12 illustrate the mesoscale circulation and fluxes when the synoptic wind is 5 m s^{-1} and 10 m s^{-1}, respectively, with other conditions being equal to those for the case of varying N shown in Figure 4-10. In general, the synoptic winds up to 10 m s^{-1} do not have strong impact on the results based on the model simulations. When the synoptic winds increase from 0 to 10 m s^{-1}, the momentum flux in the direction parallel to the wind is enhanced by 50%, while the momentum flux in the perpendicular direction goes up only by 20%. Heat flux is doubled, but still remains at a low level of $\sim$ 25 W m^{-2}.

The impact of synoptic wind on the mesoscale circulation predicted by the model is shown to be much weaker than that based on the stochastic linear theory under the same land surface conditions.

4.5 Linear Analytical Model vs Nonlinear Numerical Model

The basic differences between the linear analytical theory and the nonlinear numerical model come from the treatment of nonlinear advection terms and the modeling of dissipation process in the governing equations. The linear theory neglects the nonlinear advection terms and represents the dissipation mechanism by a linear damping (Rayleigh friction) process with constant dissipation rate. The CLARK numerical model includes all nonlinear advection terms and uses the flow-dependent eddy diffusion to represent the dissipation effect.

For the purpose of comparison, the dissipation rate α (Rayleigh friction parameter) in the linear model is estimated from the numerical simulation to make the comparison consistent (see Appendix D). Figure 4-13 shows the mesoscale circulation and mesoscale fluxes predicted by the linear theory. Figure 4-5 shows the mesoscale circulation and mesoscale fluxes obtained from the numerical simulation. Both cases use identical surface forcing and synoptic conditions.

The fundamental features of the spatial-temporal distribution of mesoscale circulation and fluxes predicted by the stochastic linear theory are consistent with the numerical model (compare Figure 4-13 with Figure 4-5). It indicates that the linear model is able to capture the basic physics behind the thermally induced mesoscale flow qualitatively. Quantitative comparison between these two Figures suggests that the linear theory overestimates mesoscale flow. Intensity of the wind is overestimated by a factor of about five, and heat flux by a factor of 20. In contrast, the linear theory underestimates momentum fluxes (being zero) in the absence of synoptic wind. Furthermore, the impact of stability and synoptic wind on the flow and fluxes are much stronger in the linear theory (results not shown here) than in the numerical model.

4.5.1 Effect of Nonlinear Advection

The numerical CLARK model simulation indicates that the nonlinear advection terms are greater than the linear time-derivative terms (see Figure 4-14). They are more important in the lower atmosphere where the thermally induced mesoscale circulation is significant. The nonlinear advection provides primary momentum transport mechanism in flow systems. Therefore, it is responsible for momentum flux within the mesoscael system since neglecting the nonlinear advective terms in the linear theory leads to zero momentum flux when synoptic wind is absent. The fact that the momentum fluxes remain when the eddy diffusion terms vanish (i.e. $K_m = 0$) (see Figure 4-17) support this argument.

4.5.2 Effect of Eddy Diffusion

The flow-dependence of the eddy diffusion coefficient K_m in the CLARK numerical model dominates spatial-temporal distribution of mesoscale circulation, particularly in the decaying stage. When the thermally induced flow decays as the result of dissipation, the value of K_m decreases in general (see Figure 4-16). This property of K_m is responsible for the varying decaying rate of the standard deviations of the wind velocities computed from the numerical simulations (comparing the left column with the right shown in Figure 4-18, 4-19, 4-20, and 4-21).

K_m is found to have stronger influence on the horizontal winds than on the vertical wind. For example in the case of neutral stability, as K_m (assumed to be a constant) goes from 0 to 70 m^2 s^{-1}, the maximum horizontal wind decreases from 35 m s^{-1} to 7 m s^{-1} while the maximum vertical velocity only drops from 2 m s $^{-1}$ to 1 m s^{-1}. But the spatial-temporal distribution of momentum flux is much less sensitive to the value of K_m. This supports the earlier argument that it is the nonlinear advection terms that mainly responsible for the momentum flux. Unlike α in the linear theory, the impact of K_m on the mesoscale heat flux is quite weak due to relatively weak influence of K_m on the vertical wind and potential temperature. The mesoscale heat flux does not change significantly as K_m goes form 7 m^2 s^{-1} to 70 m^2 s^{-1} based on the CLARK model simulations.

Discussion The linear model differs from the nonlinear numerical model mainly in two aspects: nonlinear advection and dissipation process. We argue that the underestimation of momentum flux and the sensitivity of the dependence of mesoscale circulation on synoptic wind and on stability predicted by the linear theory are caused by the omission of the nonlinear advection terms. These terms represent the transport of momentum due to the perturbed flow induced by the surface forcing. Linearization implies that there is no momentum transport mechanism when synoptic wind is zero. The thermal forcing accelerates only air parcels in a linear atmosphere. The same forcing accelerates the air parcels and is responsible for the transport of momentum in a nonlinear atmosphere. We also found in the numerical experiments that assuming zero eddy diffusion coefficient in the numerical model does not eliminate the momentum fluxes. Hence the existence of momentum fluxes can not be attributed to the dissipation process.

4.6 Summary

Several conclusions may be drawn from the numerical model simulations that have been described in this paper:

- Stability is an important factor. The stable stratification provides the dominant resistance of the atmosphere against the forcing induced by the surface sensible heat flux. Consequently, stability strongly inhibits the development of mesoscale circulation and mesoscale fluxes. Under the condition of a well mixed boundary layer and a stable free atmosphere above, thermally induced mesoscale flow is confined within the depth of planetary boundary layer.

- Impact of the synoptic wind is relatively weak compared to that of the stability. The 3D simulations have shown that presence of moderate synoptic wind increases slightly the mesoscale circulation and fluxes, in contrast to the inhibiting role of synoptic wind predicted by the linear theory. On the other hand, a possible negative feedback between the mesoscale and the large scale circulations is implied since enhancement of mesoscale momentum fluxes (downward) in turn leads to a stronger resistance to the large scale circulation.

- Any surface forcing (characterized by a spectral density function and a standard deviation of the surface sensible heat flux) with dominant length scales around the inherent length scale of the mesoscale system will be equally effective in inducing the mesoscale circulations. The functional form of the spectral density function or correlation function of the forcing is not critical. This property indicates that the atmosphere at mesoscales tends to respond to the surface forcing of a certain range of length scales under the same variability (standard deviation) of the forcing.The land surface heterogeneity, with length scales around a few tens of kilometers, is effective in forcing significant mesoscale circulations.

- Mesoscale momentum fluxes are one order of magnitude stronger, and mesoscale heat flux is one order of magnitude weaker than the corresponding turbulent fluxes in a neutral atmosphere. Hence in the absence of the resistance due to buoyancy the mesoscale circulation is more effective than turbulence in transporting kinetic energy, which will eventually dissipate into heat through viscosity. In a stable atmosphere, mesoscale and turbulent momentum fluxes are comparable, while mesoscale heat flux is insignificant.

The thermal flow is confined within the lowest 1 km layer.

- Nonlinear advection terms are responsible for the mesoscale momentum fluxes. It has been found from the simulations that momentum fluxes may result regardless of the turbulent dissipation in the numerical model. So, satisfactory prediction of the vertical transport of kinetic energy induced by land surface heterogeneity requires nonlinear modeling of the mesoscale circulation.

- Linear theory tends to overestimate the thermal flow and heat flux, but underestimate momentum fluxes by neglecting the momentum transport mechanism in the atmosphere. The linear theory's overestimation of the heat flux is mainly due to its overestimation of the vertical velocity and the correlation between vertical velocity and the potential temperature, while the standard deviation of the potential temperature remains virtually the same as that from the numerical simulation of the nonlinear flow. Nonlinear local advection not only reduces the intensity of the mesoscale circulation, but also reduces the correlation between the wind field and the temperature since advection usually causes mixing. Linearization neglects the momentum transport mechanism, leading to a underestimation of momentum fluxes.

level	z (m)
1	0
2	53
3	156
4	309
5	513
6	768
7	1073
8	1428
9	1826
10	2257
11	2712
12	3183
13	3665
14	4154
15	4647
16	5143
17	5640
18	6138
19	6637
20	7136

Table 4.1: Vertical grid points in the numerical model

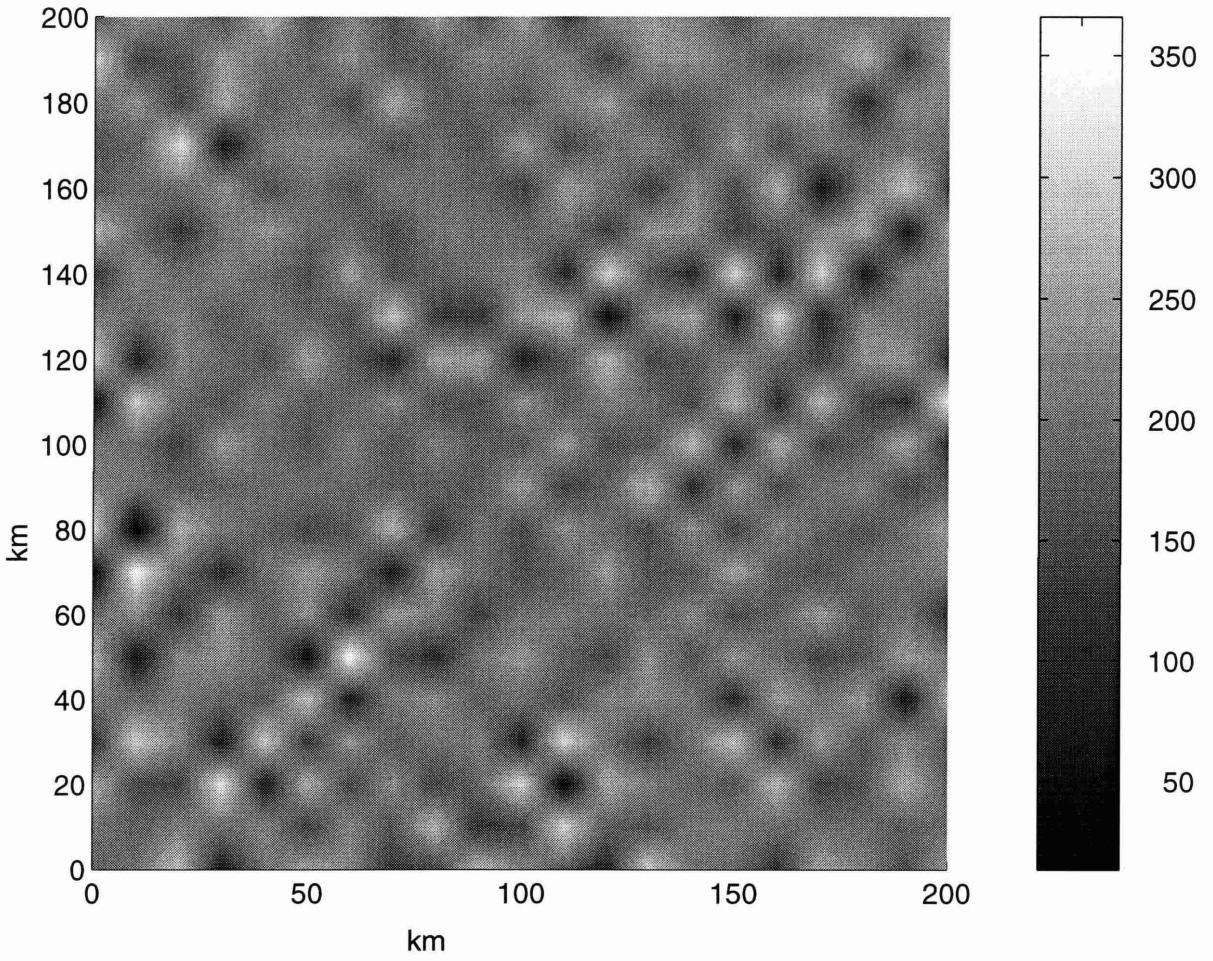

Figure 4-1: Random field of surface sensible heat flux H_s at noon time with banded white-noise spectral density function which is constant over the range of 20 km to 50 km, and zero otherwise. $H_0 = 200$ W m^{-2} and $\sigma_H = 50$ W m^{-2}.

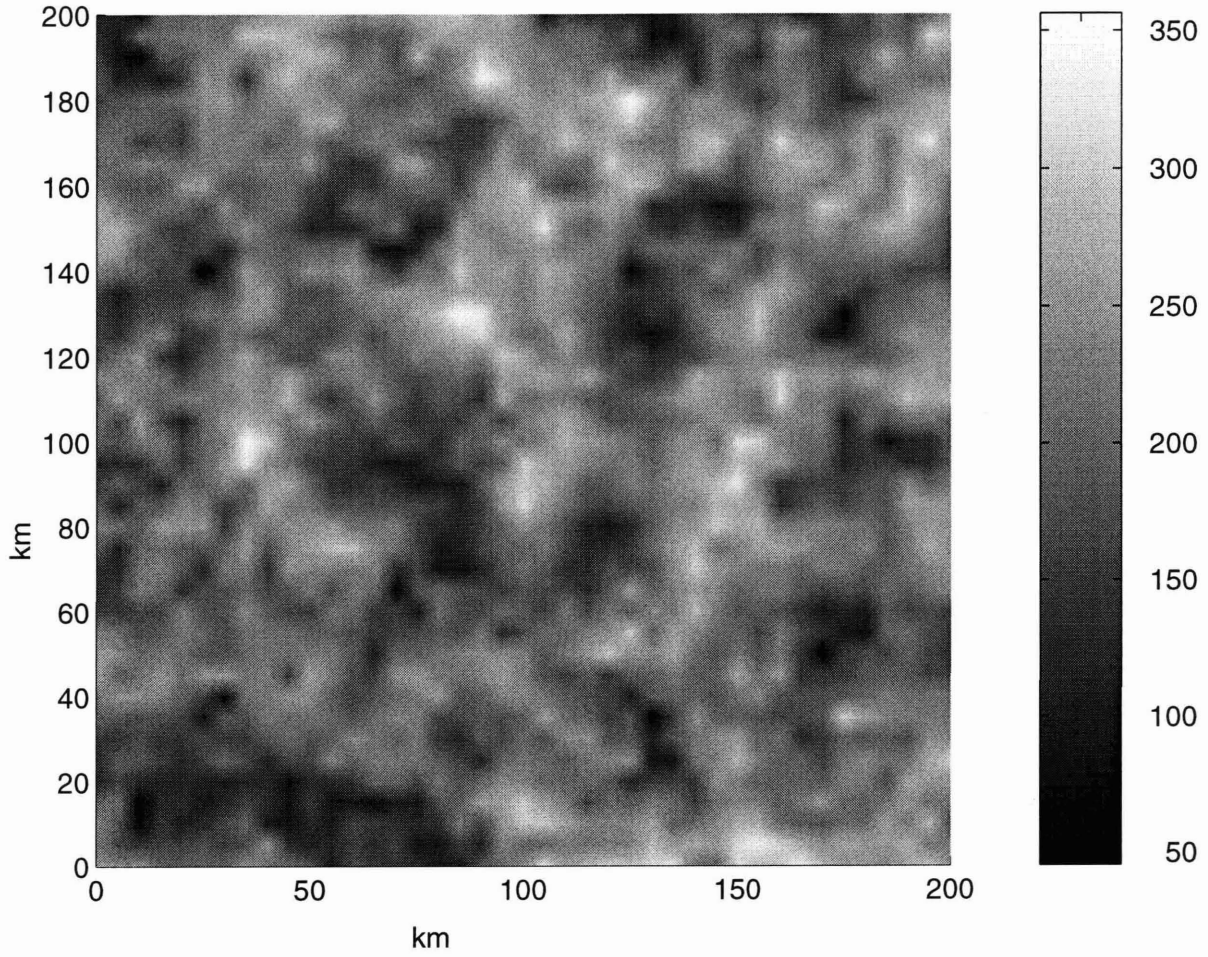

Figure 4-2: Random field of surface sensible heat flux H_s at noon time described by exponential correlation function with a correlation length $L = 10$ km. $H_0 = 200$ W m^{-2} and $\sigma_H = 50$ W m^{-2}.

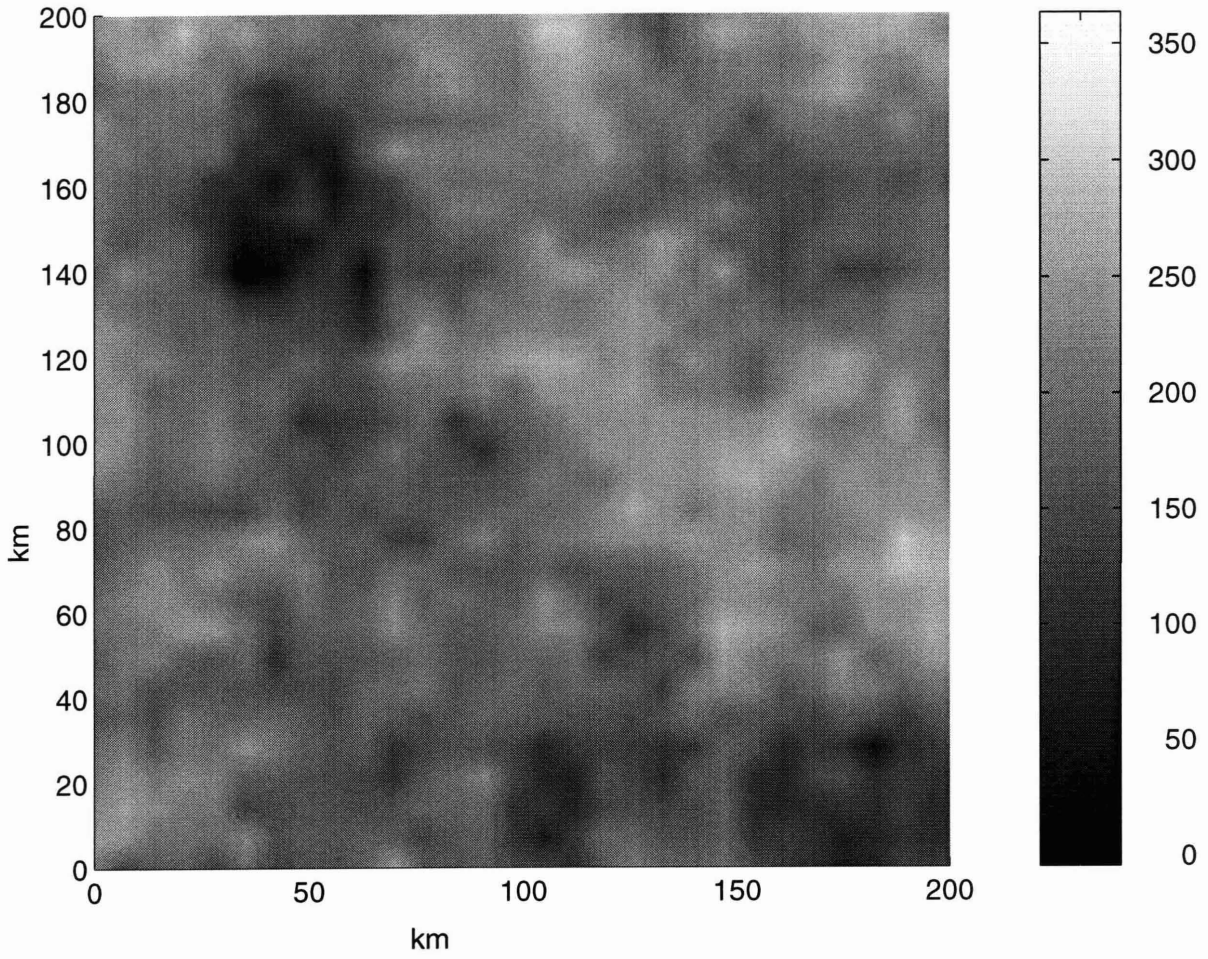

Figure 4-3: Random field of surface sensible heat flux H_s at noon time described by exponential correlation function with a correlation length $L = 30$ km. $H_0 = 200$ W m^{-2} and $\sigma_H = 50$ W m^{-2}.

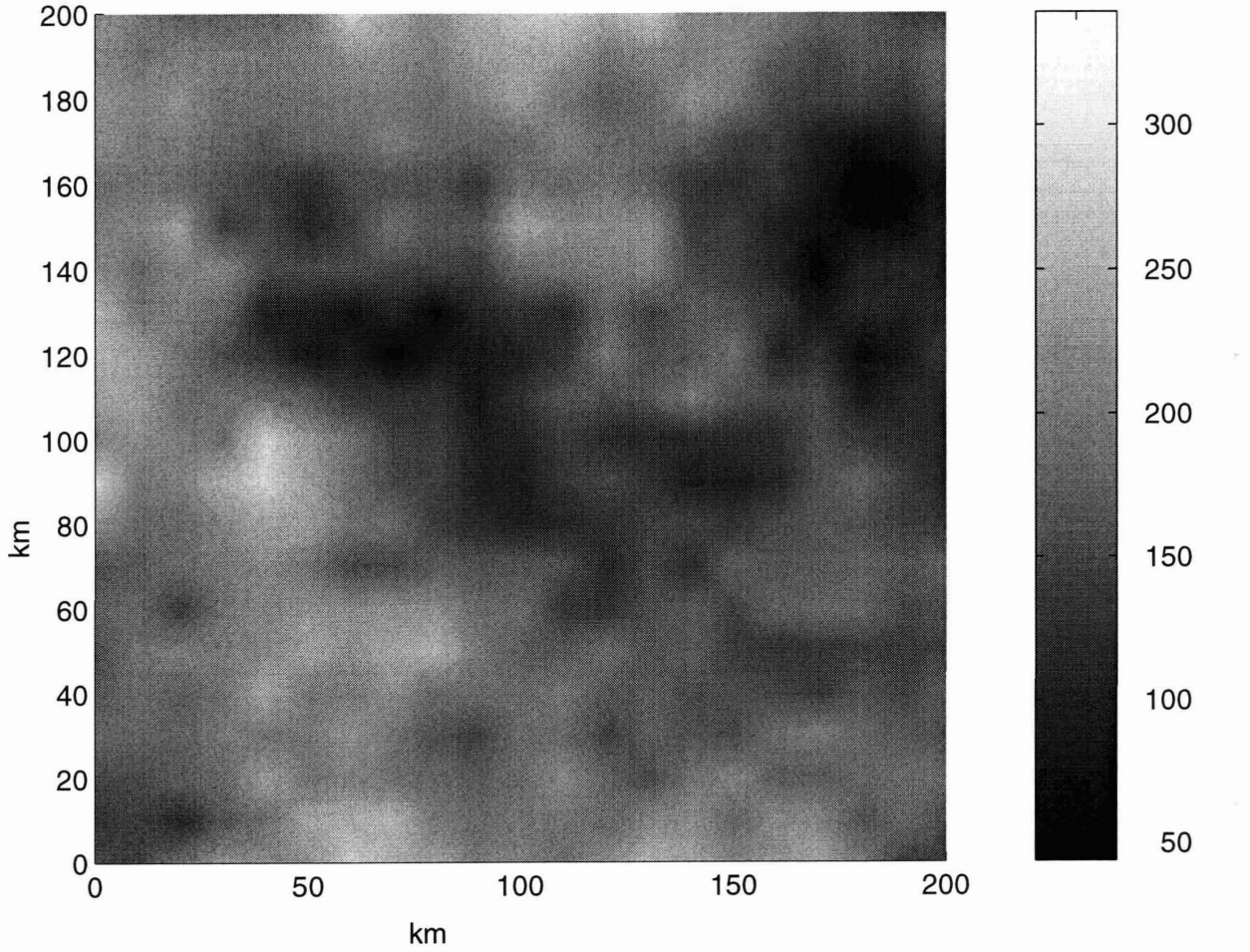

Figure 4-4: Random field of surface sensible heat flux H_s at noon time described by exponential correlation function with a correlation length $L = 50$ km. $H_0 = 200$ W m^{-2} and $\sigma_H = 50$ W m^{-2}.

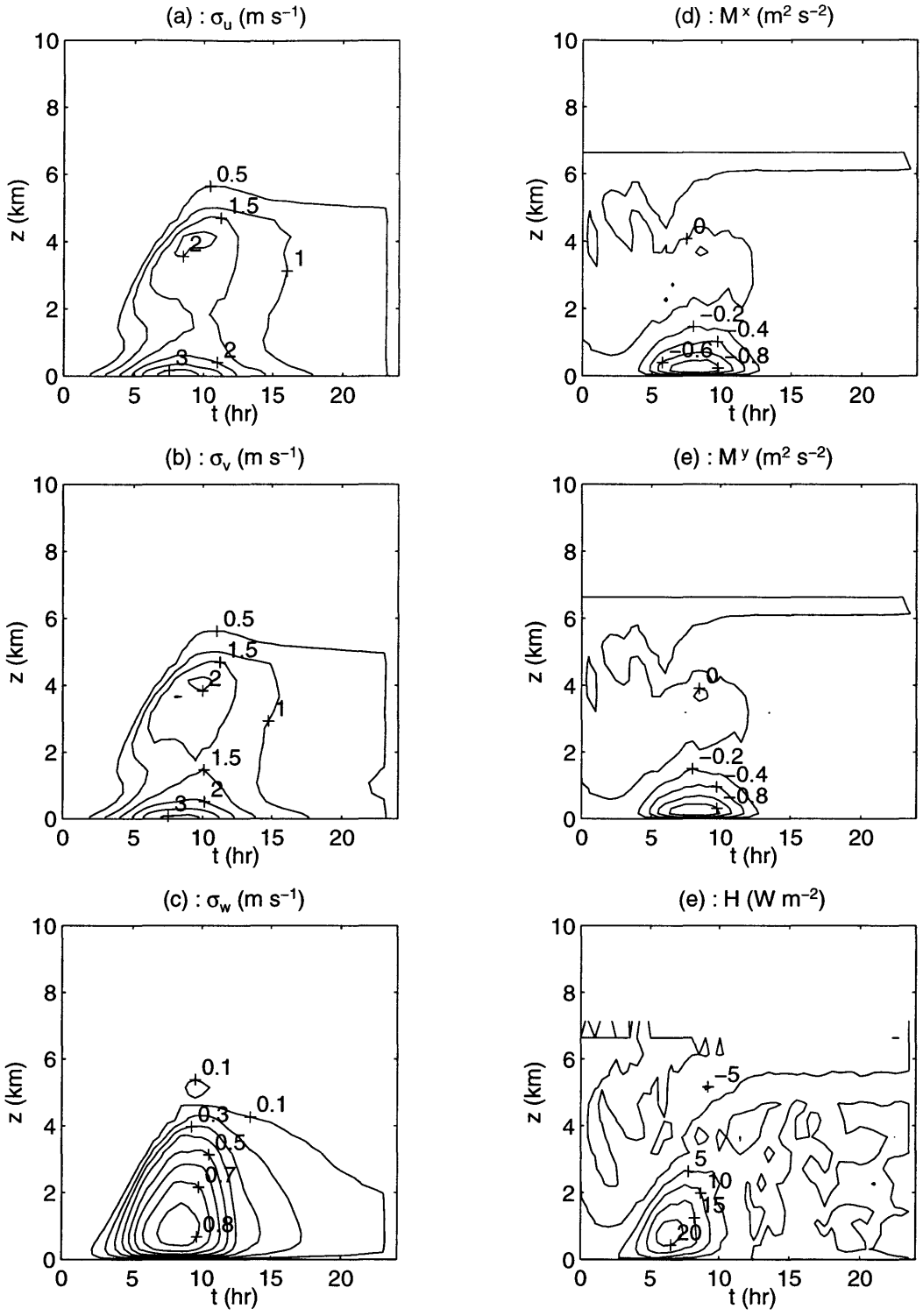

Figure 4-5: Numerical simulation of mesoscale circulations and fluxes under banded white-noise forcing in an environment of $N = 0$ and $u_0 = 0$. (a) standard deviation of u, (b) standard deviation of v, (c) standard deviation of w, (d) x momentum flux, (e) y momentum flux, and (f) heat flux

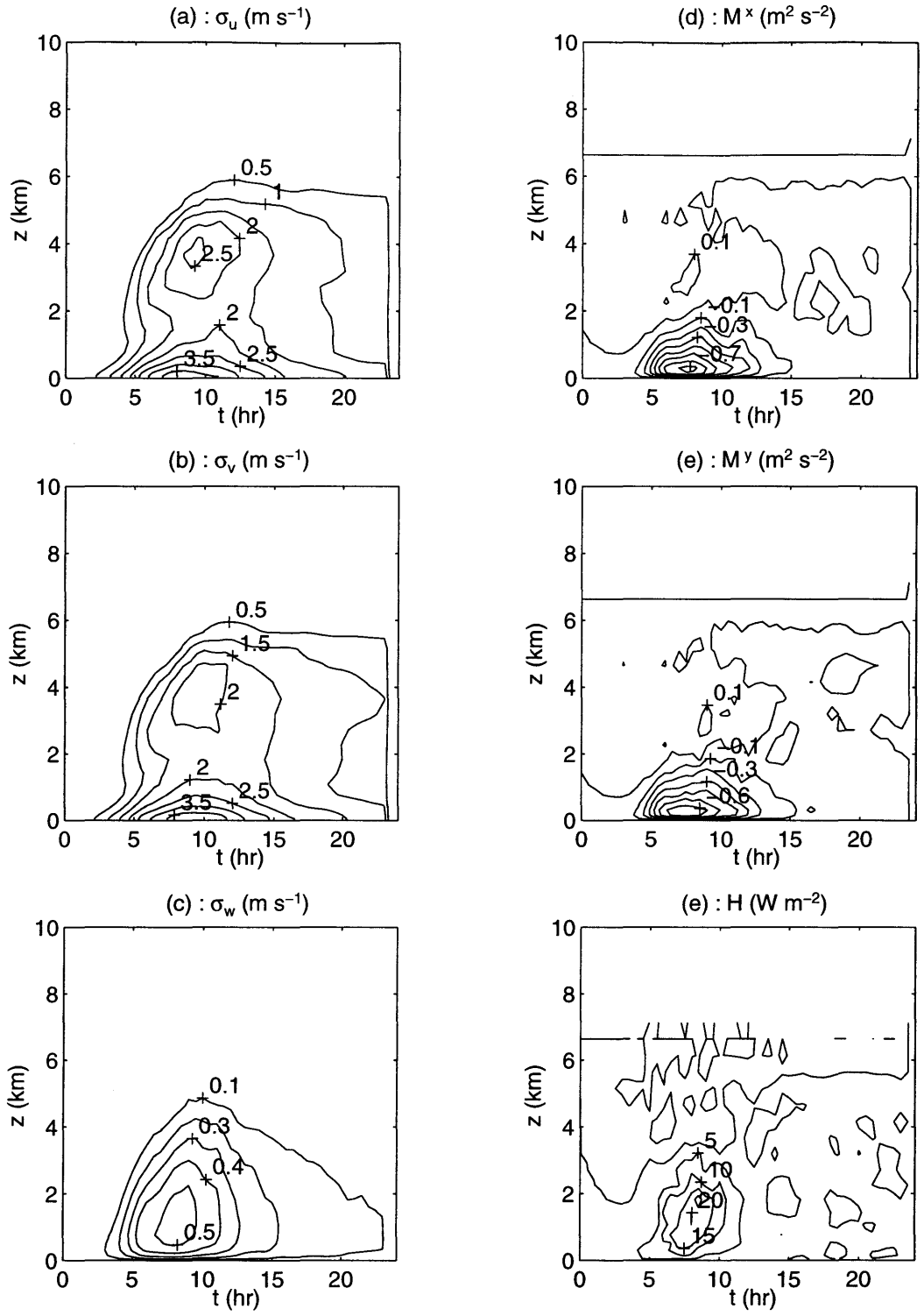

Figure 4-6: Numerical simulation of mesoscale circulation and fluxes under exponential autocorrelation forcing with $L = 10$ km in an environment of $N = 0$ and $u_0 = 0$.

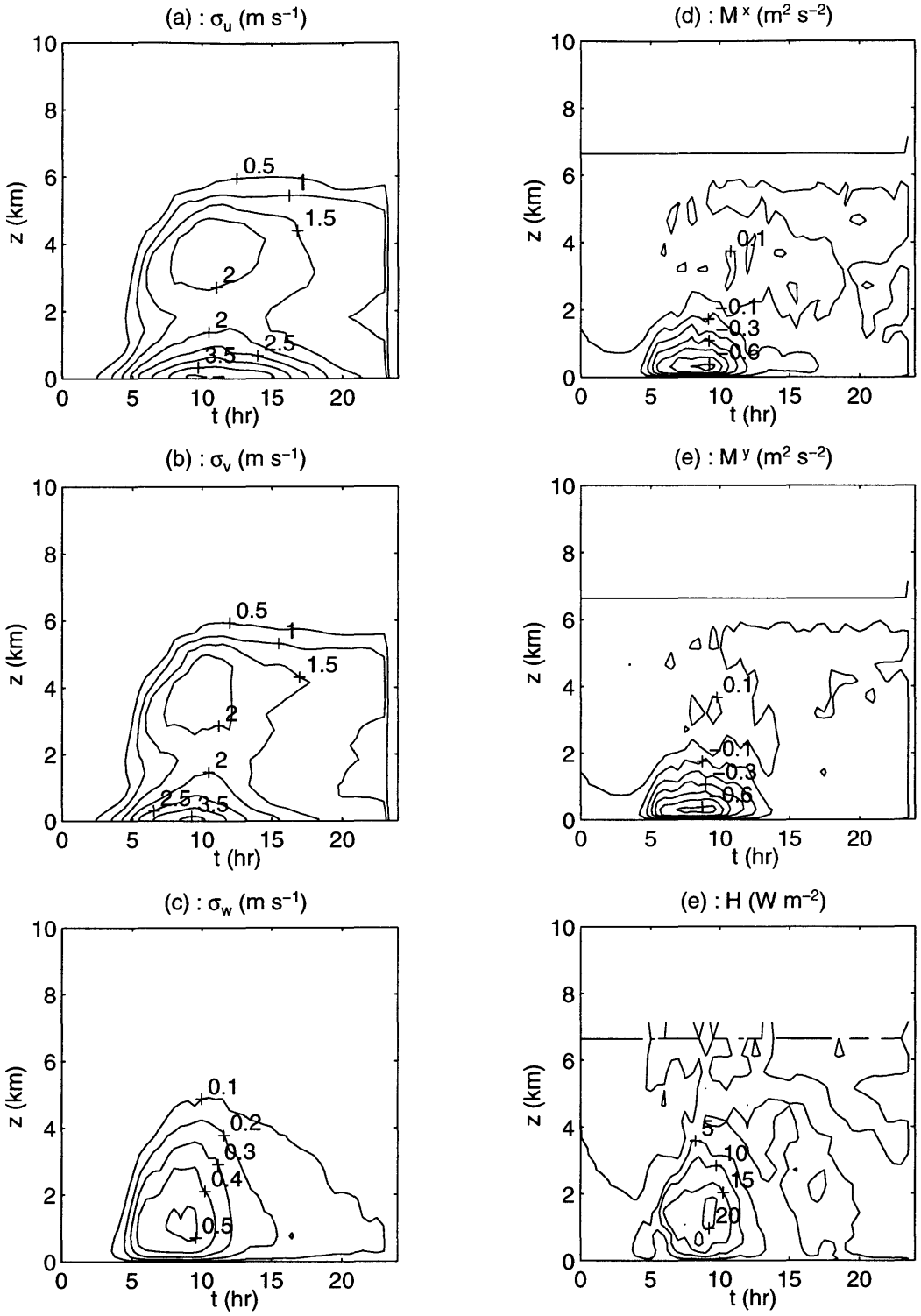

Figure 4-7: Numerical simulation of mesoscale circulation and fluxes under exponential autocorrelation forcing with $L = 30$ km in an environment of $N = 0$ and $u_0 = 0$.

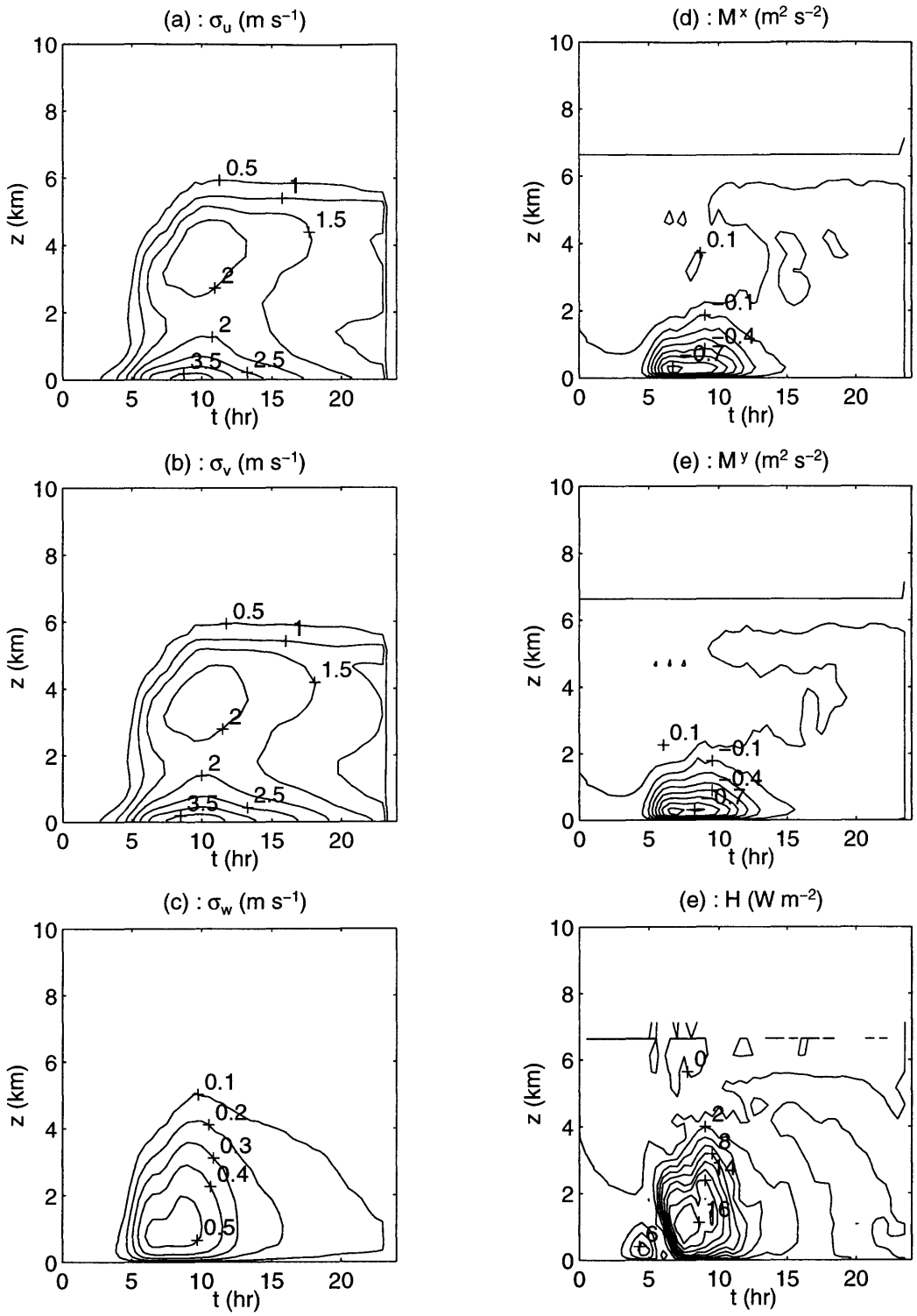

Figure 4-8: Numerical simulation of mesoscale circulation and fluxes under exponential autocorrelation forcing with $L = 50$ km in an environment of $N = 0$ and $u_0 = 0$.

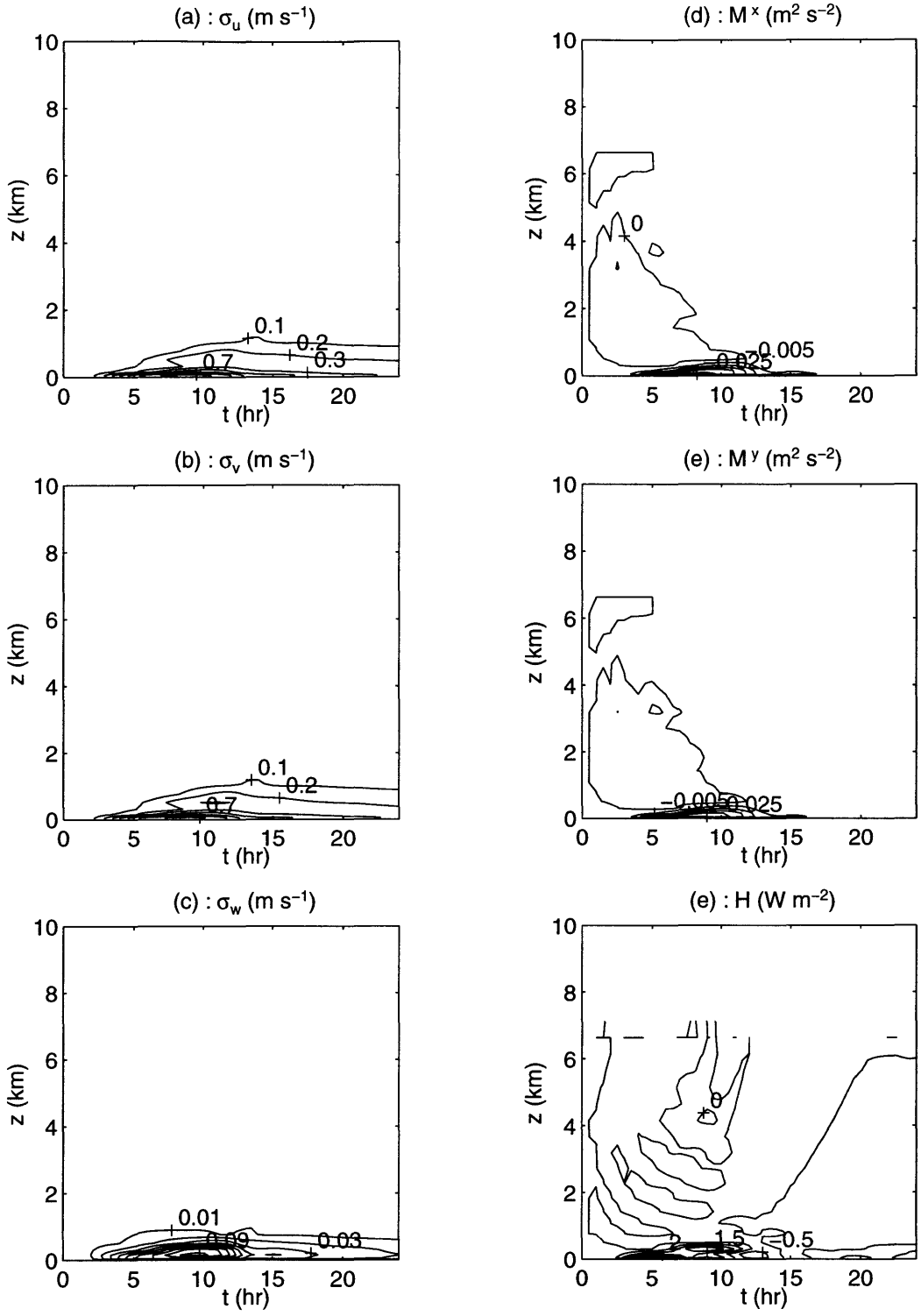

Figure 4-9: Numerical simulation of mesoscale circulation and fluxes under banded white-noise forcing in a stable atmosphere $N = 10^{-2}$ s^{-1}, and zero synoptic wind $u_0 = 0$.

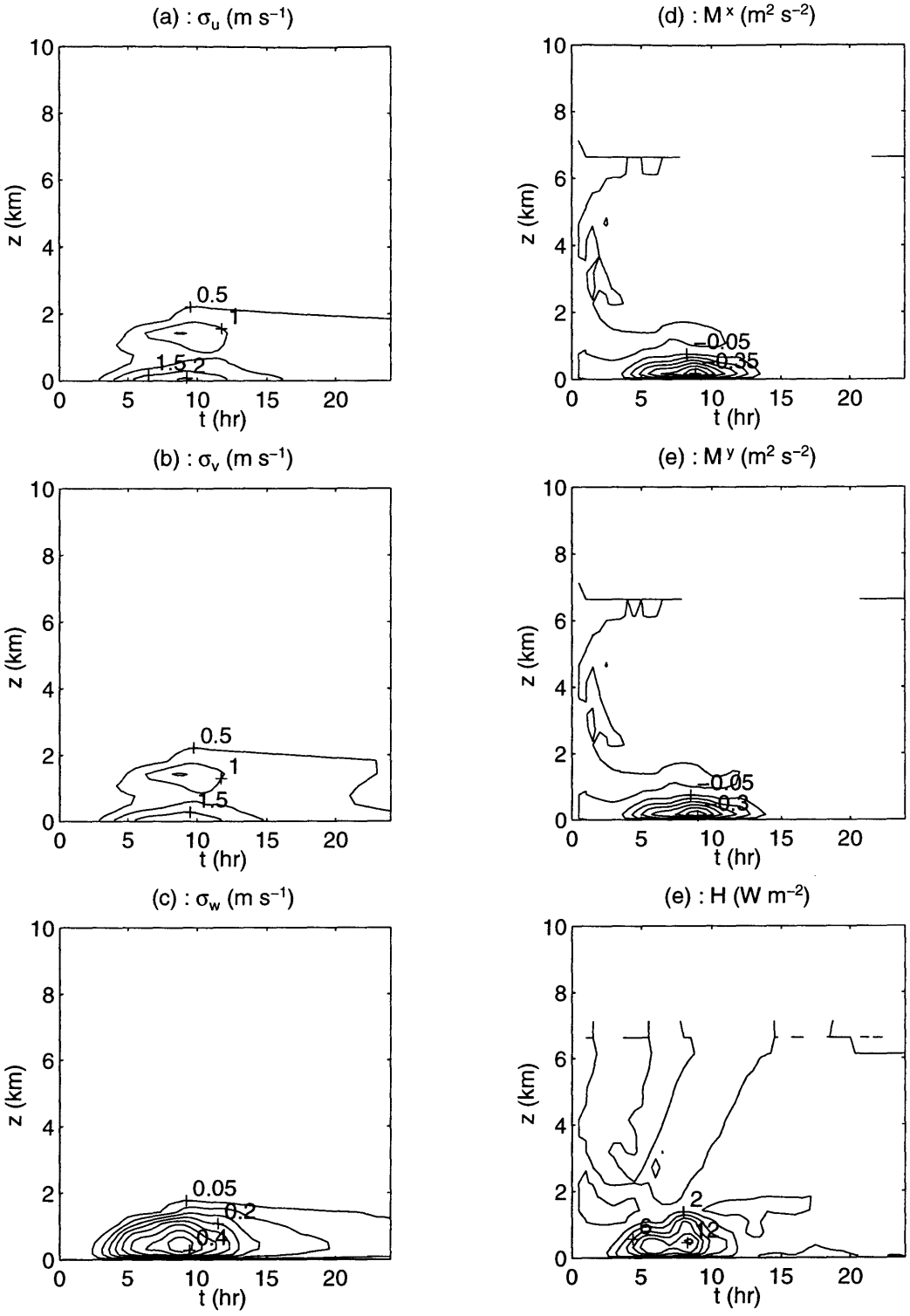

Figure 4-10: Numerical simulation of mesoscale circulation and fluxes under banded white-noise forcing in an atmosphere of varying stability (N = 0 in the lowest 1 km layer, and $N = 10^{-2}$ s^{-1} above), and zero synoptic wind $u_0 = 0$.

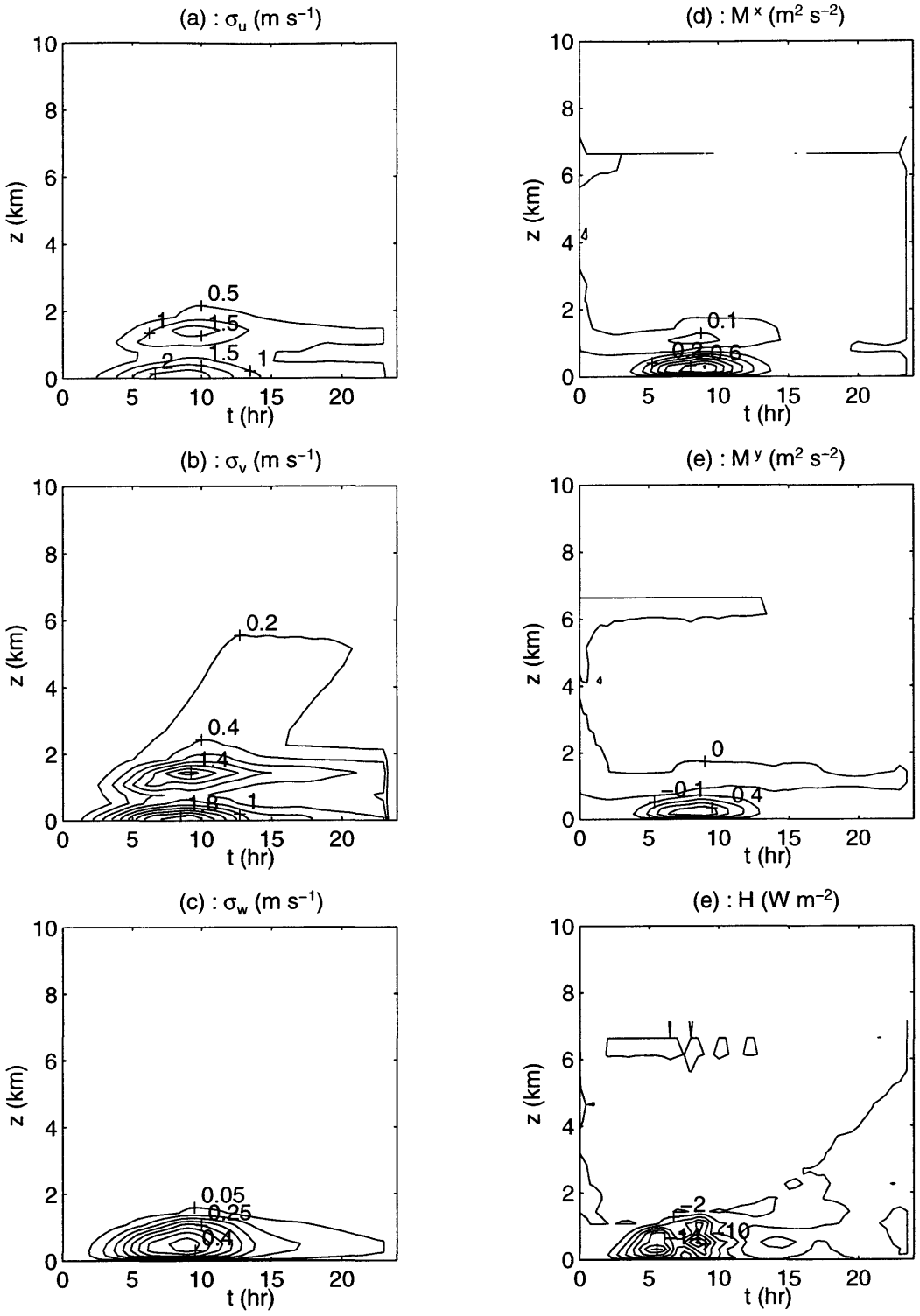

Figure 4-11: Numerical simulation of mesoscale circulation and fluxes under banded white-noise forcing in an atmosphere of varying stability (N = 0 in the lowest 1 km layer, and $N = 10^{-2}$ s^{-1} above), and synoptic wind $u_0 = 5$ m s^{-1}.

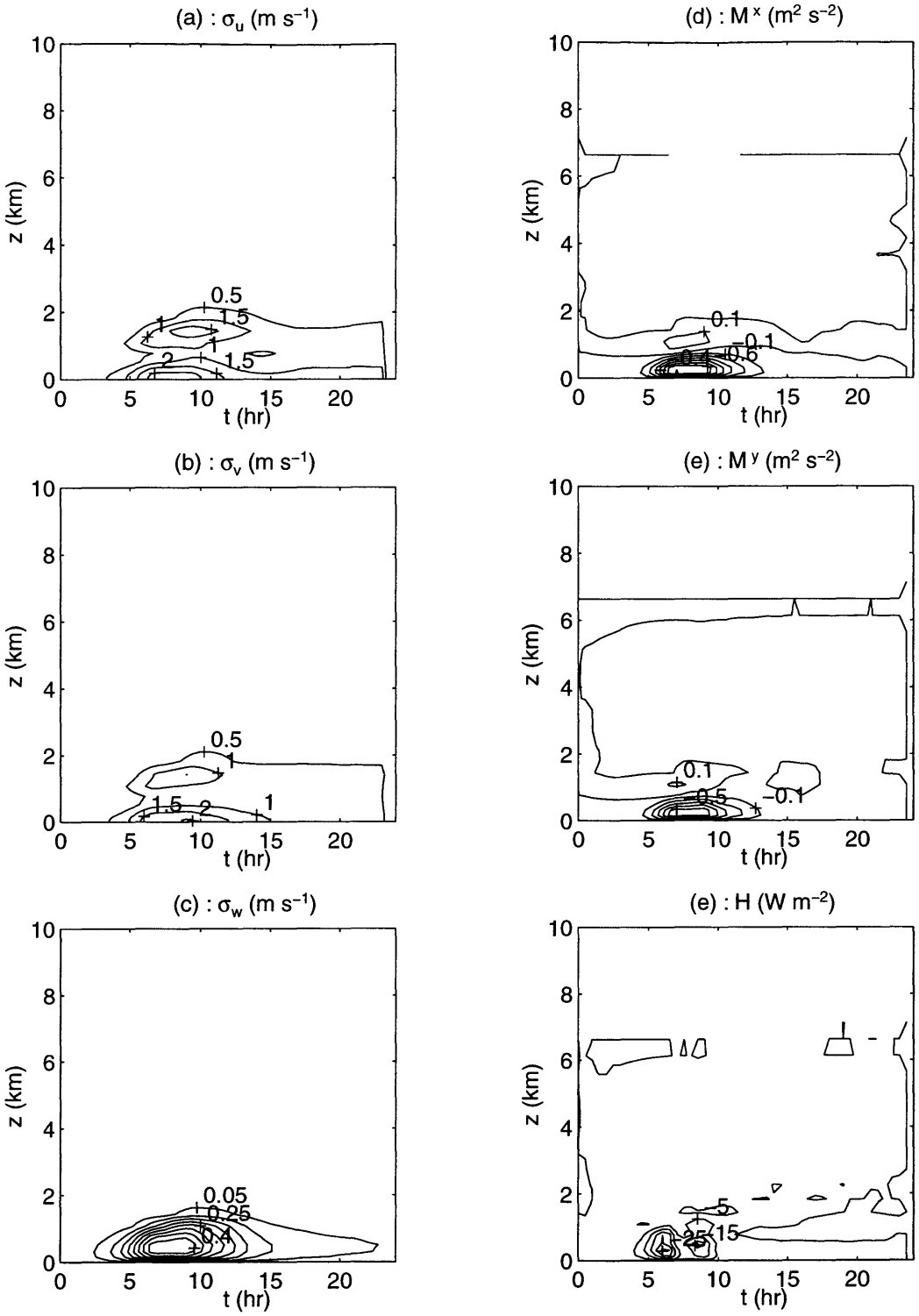

Figure 4-12: Numerical simulation of mesoscale circulation and fluxes under banded white-noise forcing in an atmosphere of varying stability (N = 0 in the lowest 1 km layer, and $N = 10^{-2}$ s^{-1} above), and synoptic wind $u_0 = 10$ m s^{-1}.

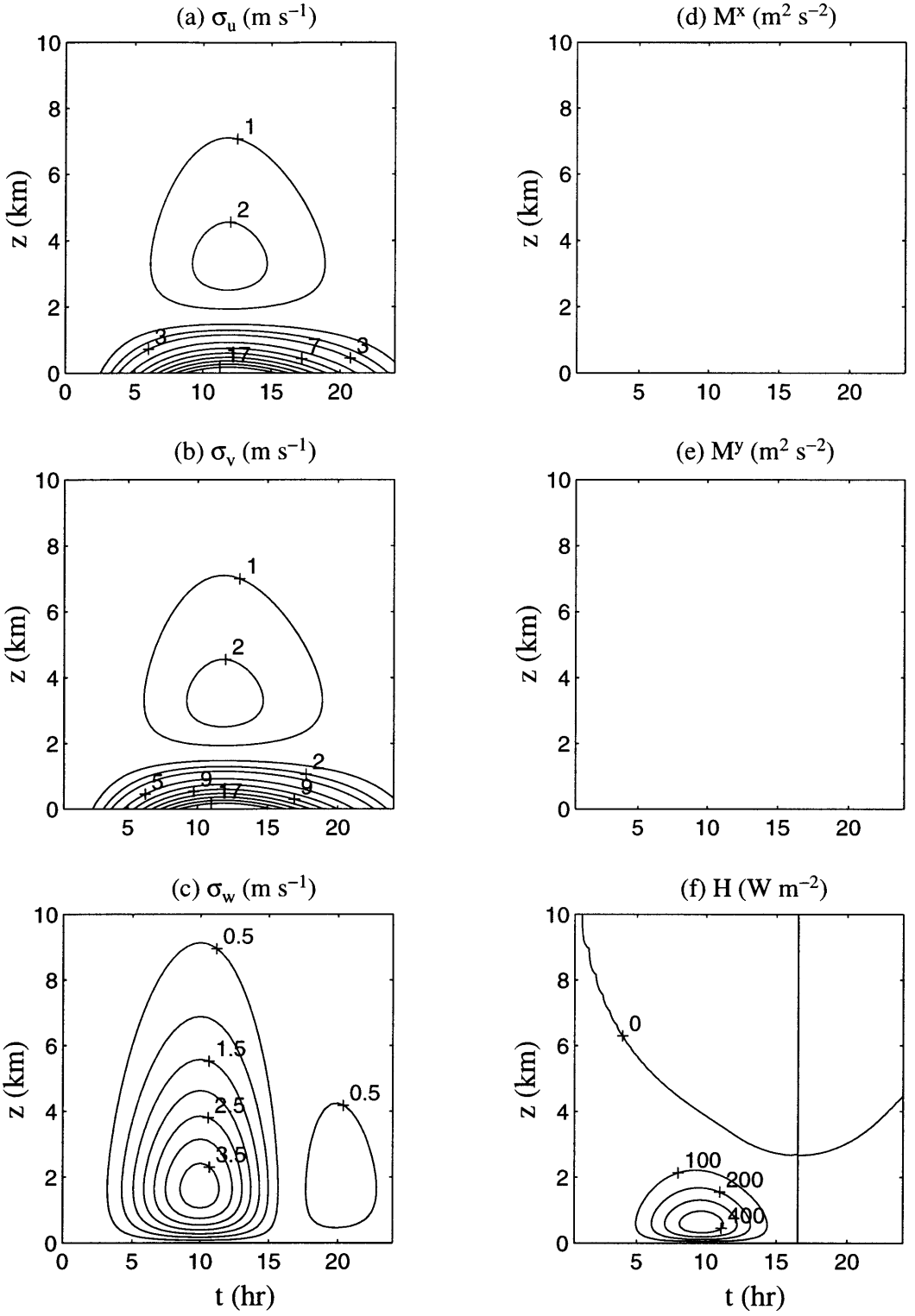

Figure 4-13: Sthochastic linear theory of mesoscale circulation and fluxes under banded white-noise forcing in an atmosphere of neutral stratification (N = 0) and zero synoptic wind ($u_0 = 0$).

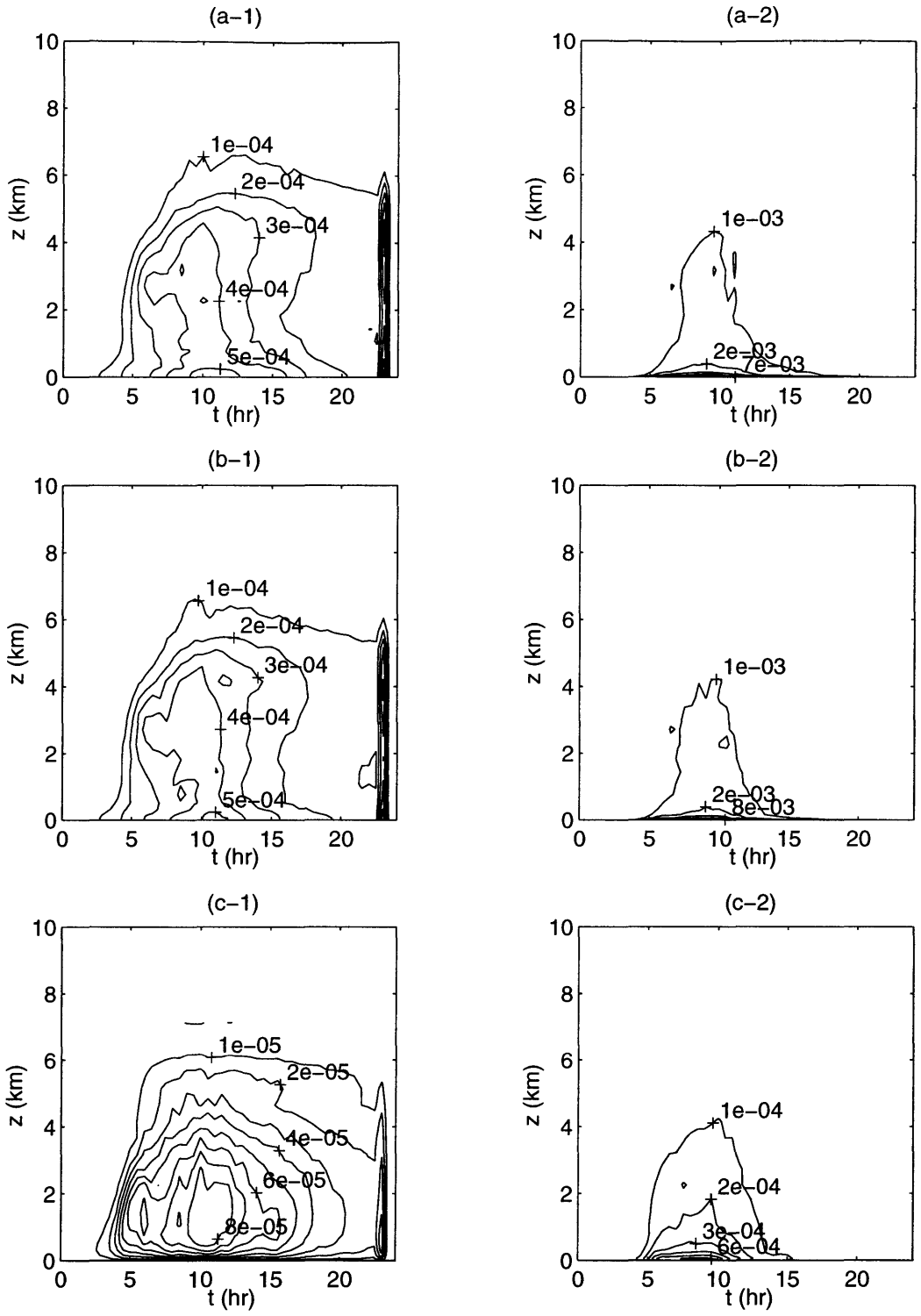

Figure 4-14: Time-derivative term (domain-mean absolute value) vs non-linear advective terms (sum of domain-mean absolute values) computed from CLARK model. (a-1) $\partial u/\partial t$, (a-2) $\vec{u} \cdot \nabla u$; (b-1) $\partial v/\partial t$, (b-2) $\vec{u} \cdot \nabla v$; (c-1) $\partial w/\partial t$, (c-2) $\vec{u} \cdot \nabla w$ where $\vec{u} = (u, v, w)$.

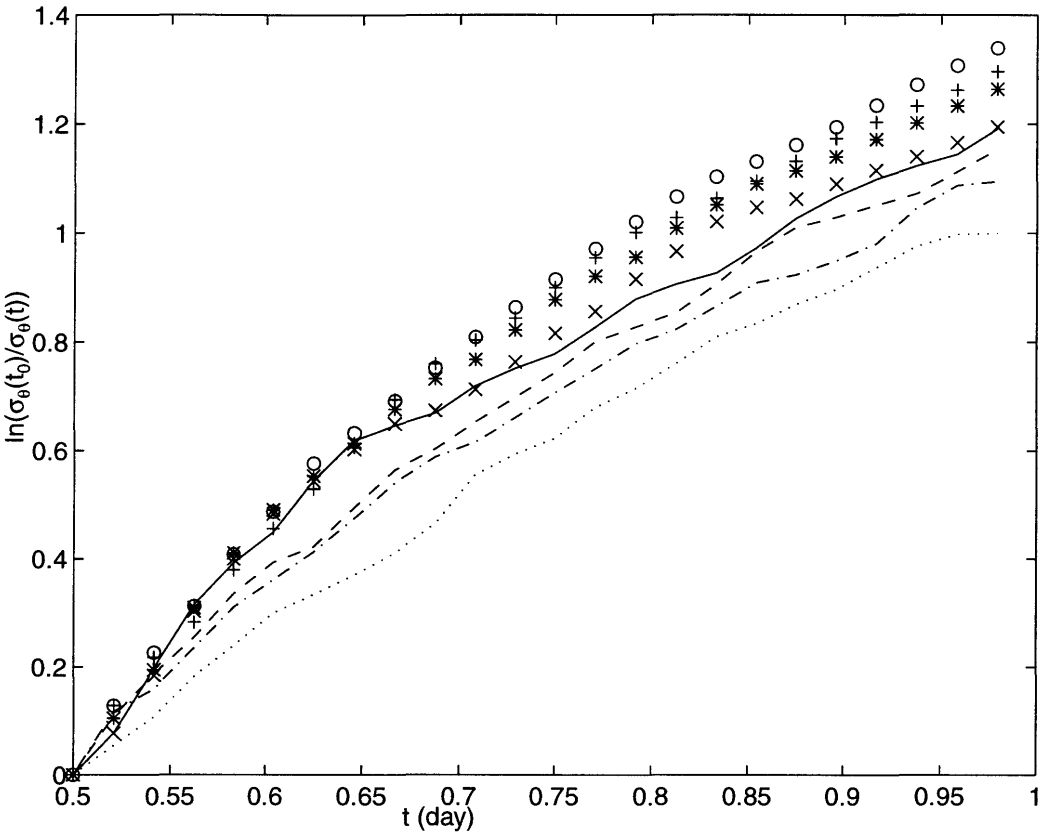

Figure 4-15: Standard deviation of potential temperature σ_θ vs time t at : z=53 m (+); z=156 m ($\circ$); z=306 m ($*$); z=513 m ($\times$); z=768 m (solid); z=1073 m (dash); z=1428 m (dash-dot); z=1826 m (dot)

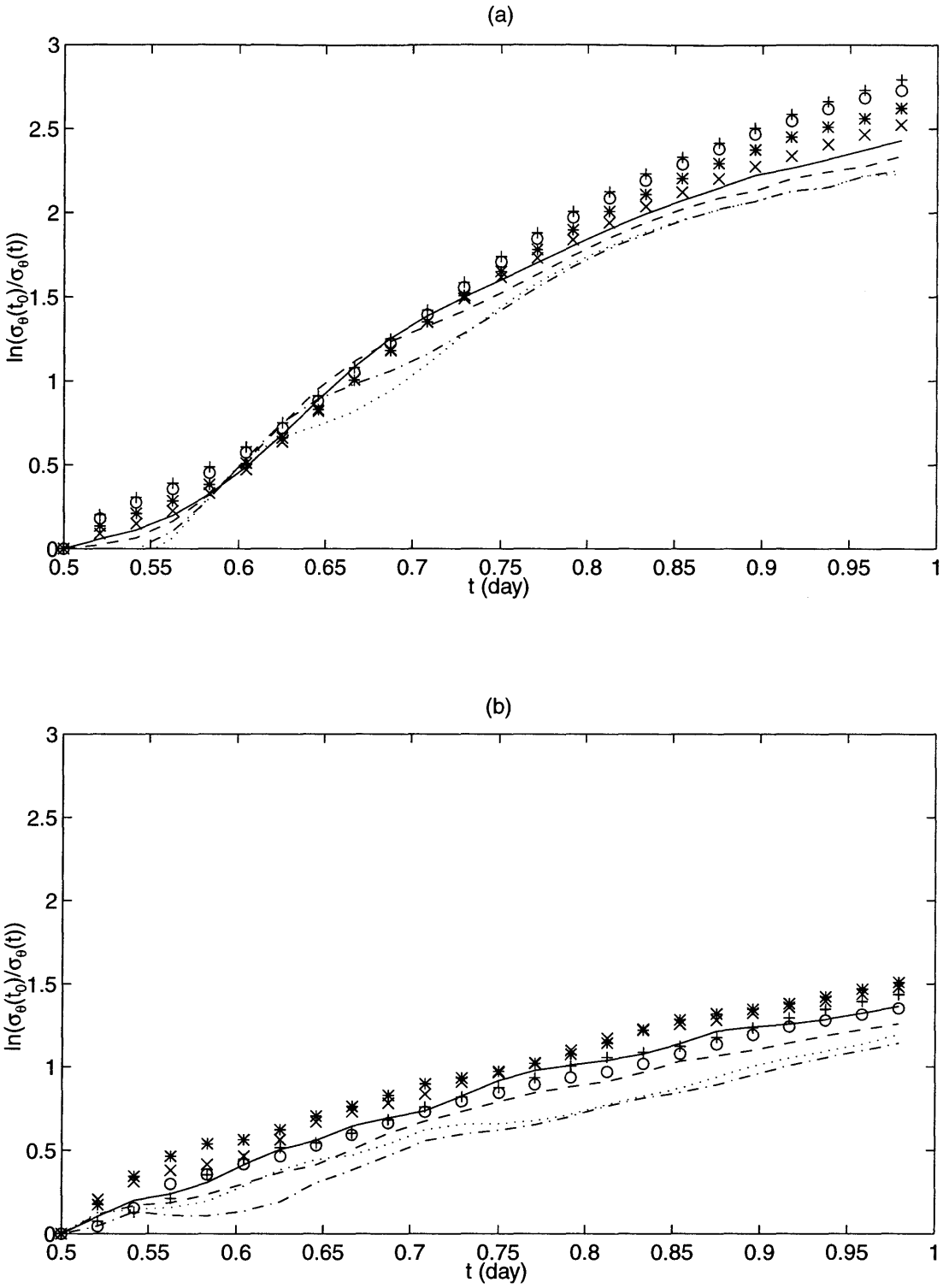

Figure 4-16: Same as Figure 4-15 (a) $K_m = 70$ m^2 s^{-1}, (b) $K_m = 7$ m^2 s^{-1}

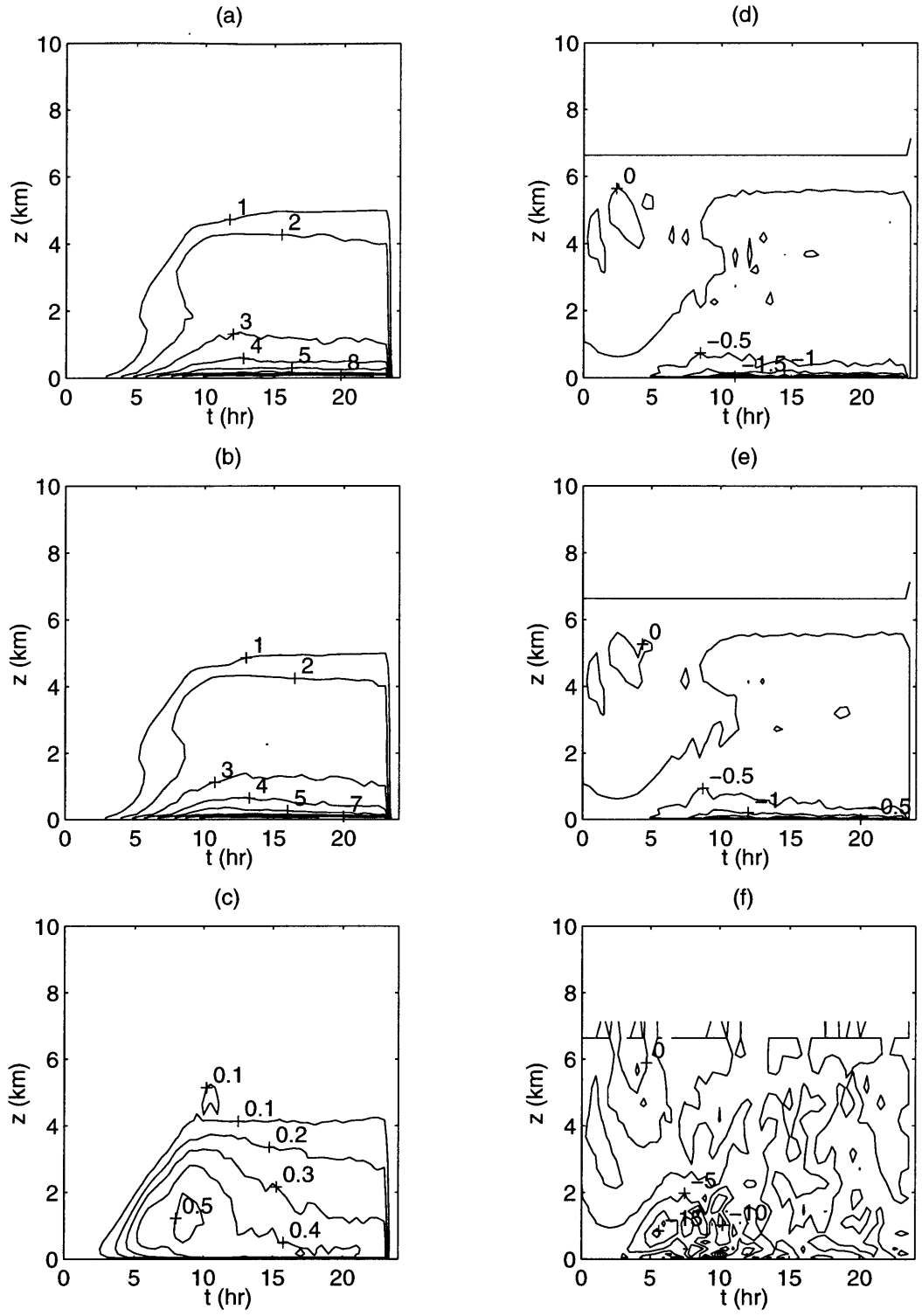

Figure 4-17: Standard deviation of wind velocities and mesoscale of fluxes in the case of $K_m = 0$ under banded white-noise surface heating distribution. (a) σ_u (m s^{-1}), (b) σ_v (m s^{-1}), (c) σ_w (m s^{-1}), (d) M_m^x (m^2 s^{-2}), (e) M_m^y (m^2 s^{-2}), and (f) H_m (W m^{-2})

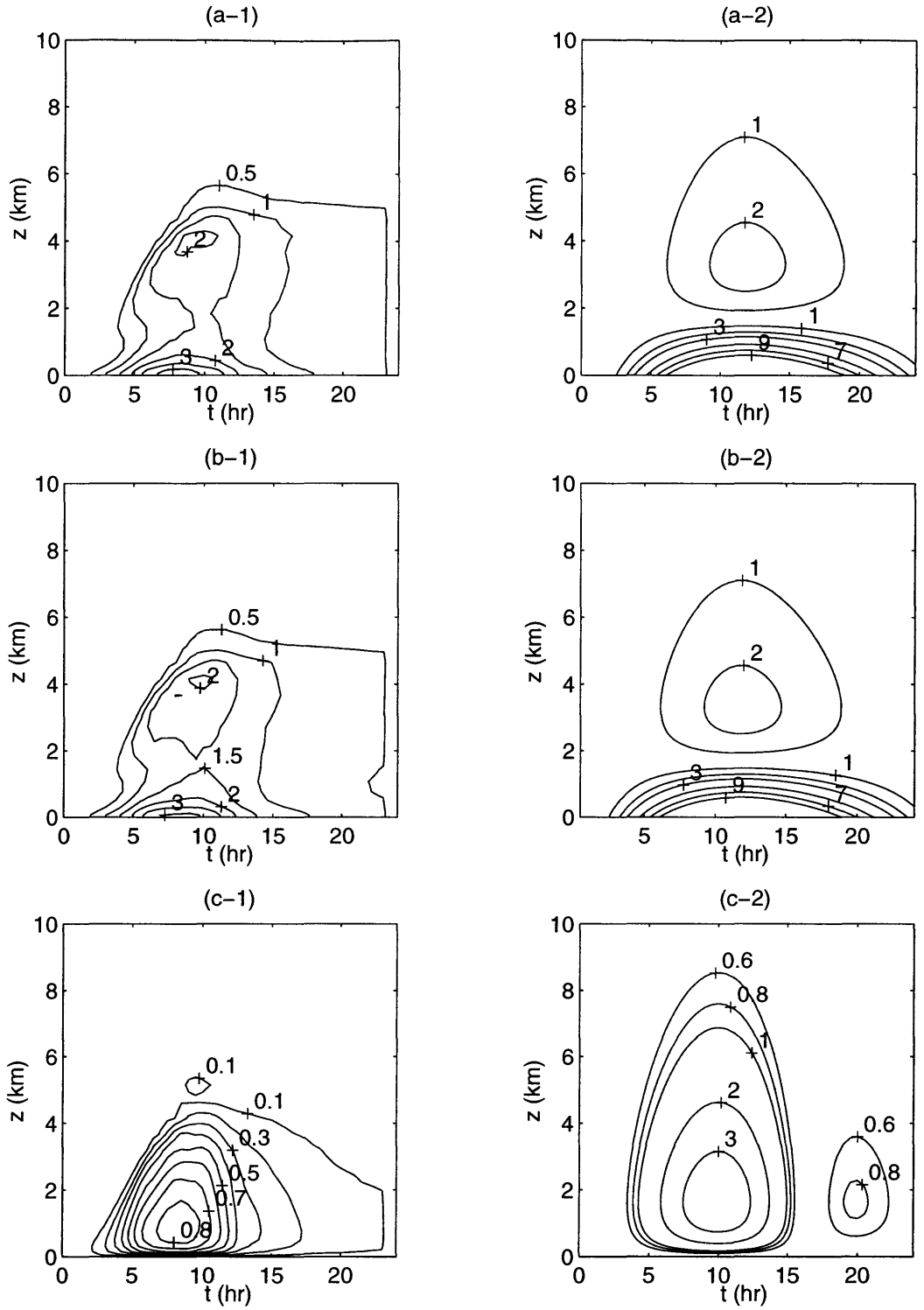

Figure 4-18: Standard deviation of wind velocities : numerical simulation (left column) vs linear theory (right column) under banded white-noise surface heating distribution. $H_0 = 200$ W m^{-2}, $\sigma_H = 50$ W m^{-2}, and $\alpha = 0.6\Omega_0$. (a) σ_u (m s^{-1}), (b) σ_v (m s^{-1}), (c) σ_w (m s^{-1}).

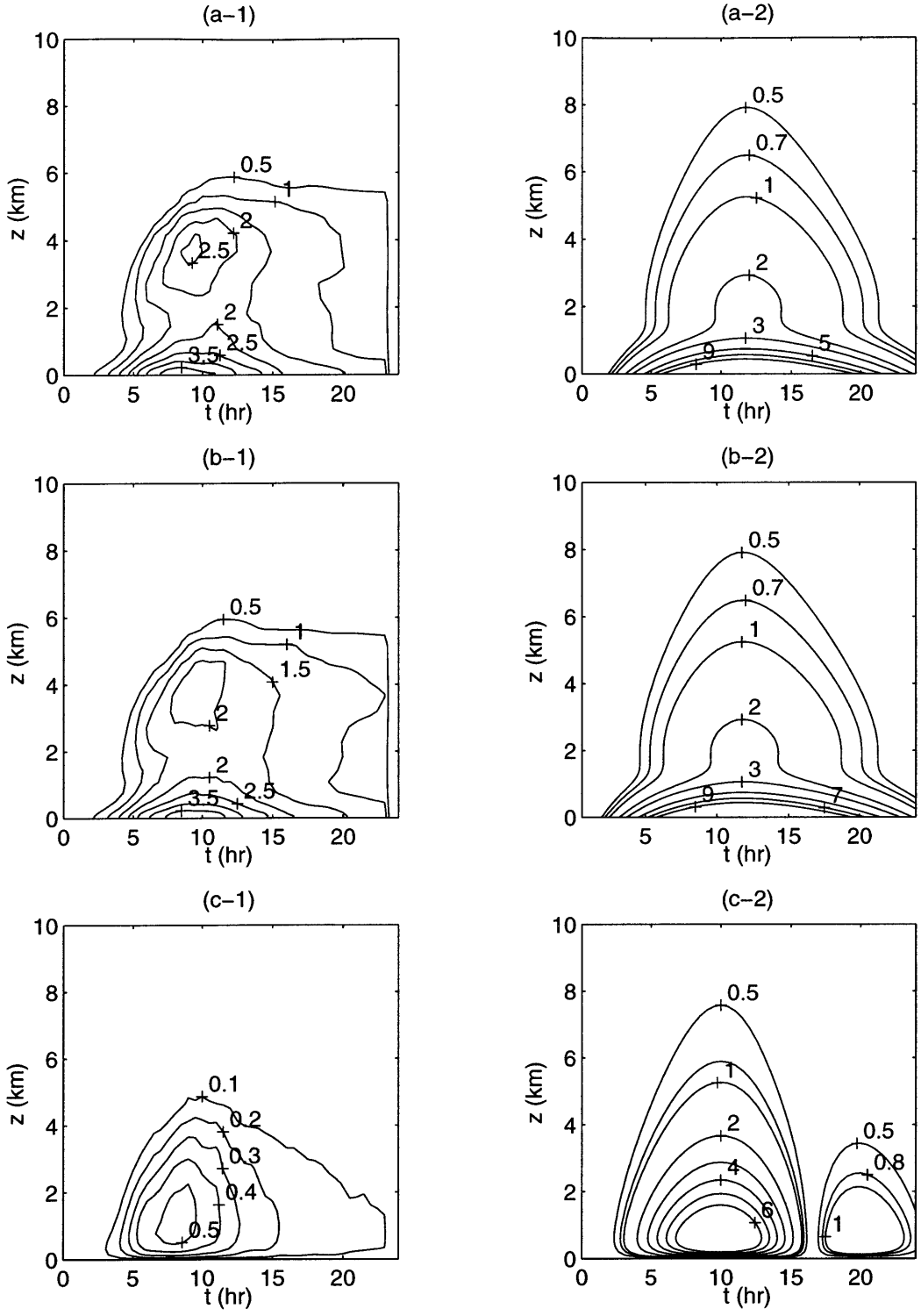

Figure 4-19: Standard deviation of wind velocities : numerical simulation (left column) vs linear theory (right column) under exponential correlation surface heating distribution with correlation length $L = 10$ km. $H_0 = 200$ W m^{-2}, $\sigma_H = 50$ W m^{-2}, and $\alpha = 0.6\Omega_0$. (a) σ_u (m s^{-1}), (b) σ_v (m s^{-1}), (c) σ_w (m s^{-1}).

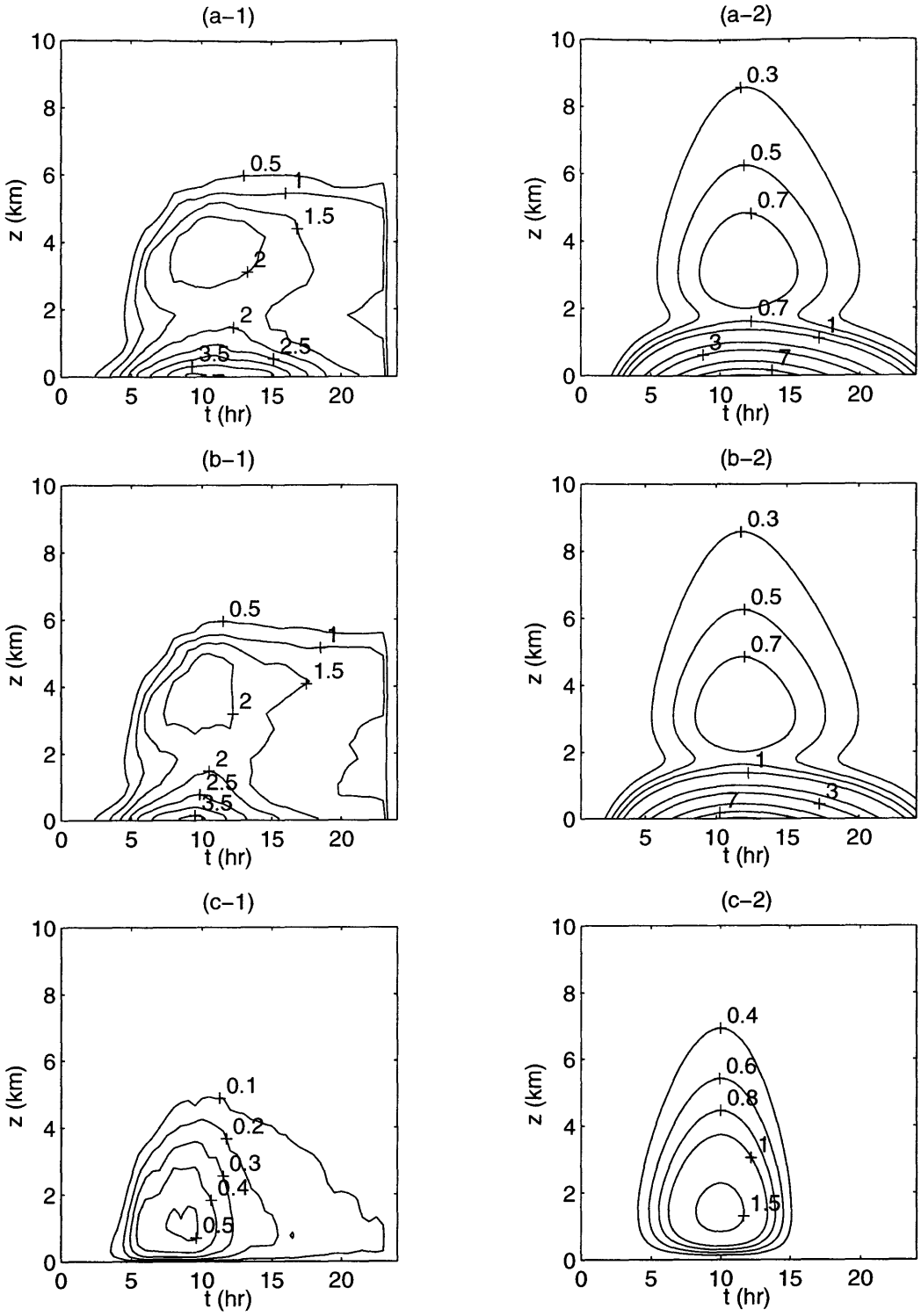

Figure 4-20: Standard deviation of wind velocities : numerical simulation (left column) vs linear theory (right column) under exponential correlation surface heating distribution with correlation length $L = 30$ km. $H_0 = 200$ W m^{-2}, $\sigma_H = 50$ W m^{-2}, and $\alpha = 0.6\Omega_0$. (a) σ_u (m s^{-1}), (b) σ_v (m s^{-1}), (c) σ_w (m s^{-1}).

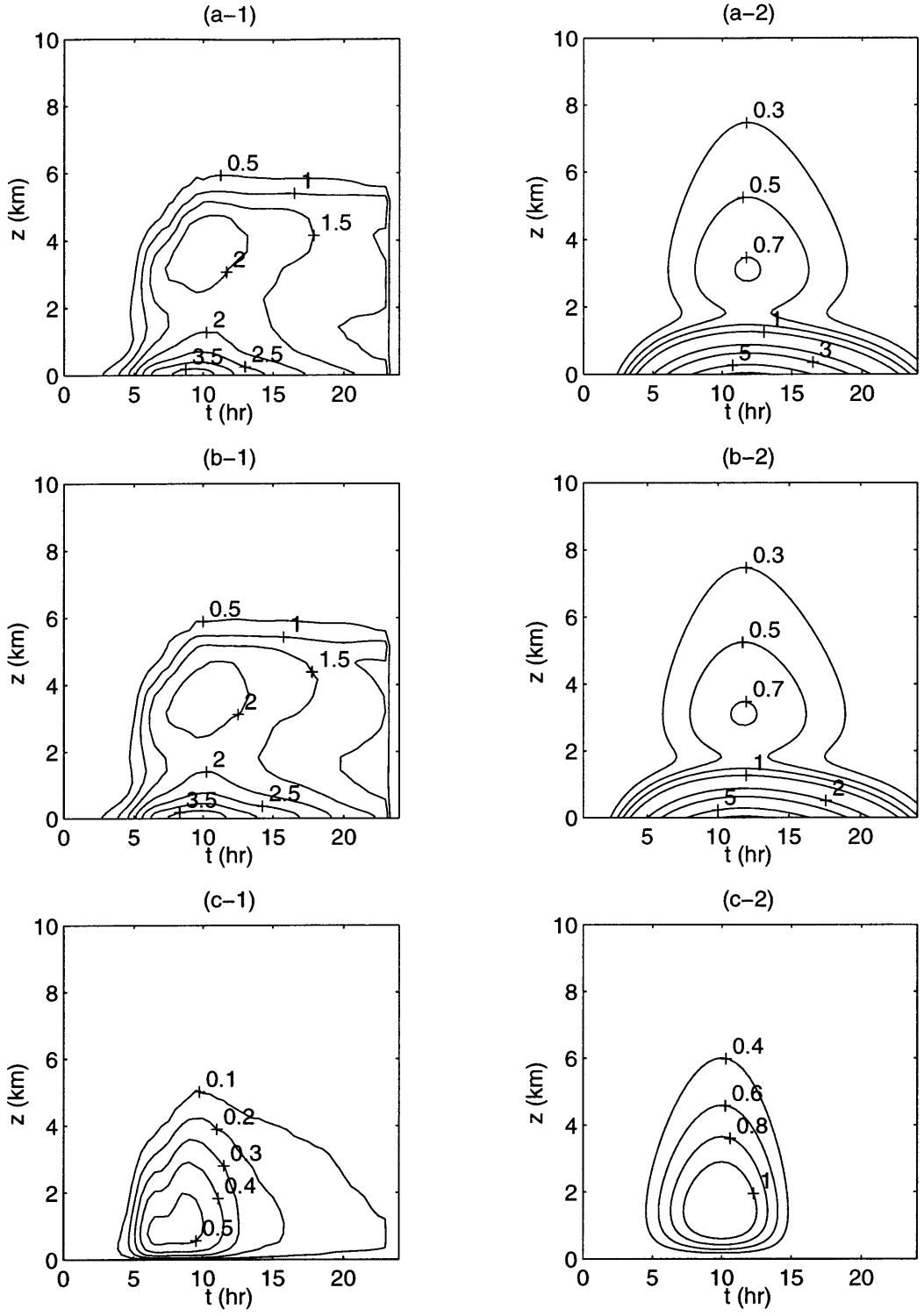

Figure 4-21: Standard deviation of wind velocities : numerical simulation (left column) vs linear theory (right column) under exponential correlation surface heating distribution with correlation length $L = 50$ km. $H_0 = 200$ W m^{-2}, $\sigma_H = 50$ W m^{-2}, and $\alpha = 0.6\Omega_0$. (a) σ_u (m s^{-1}), (b) σ_v (m s^{-1}), (c) $sigma_w$ (m s^{-1}).

Chapter 5

Stochastic Linear Model of Topographically Induced Flow

5.1 Motivation and Background

Variable topography provides another surface forcing to the mesoscale system (e.g. Atkinson 1981). Topographically induced mesoscale flow (frequently referred to as *mountain waves* in the literature) is responsible for a number of atmospheric processes such as wave drag or vertical transport of horizontal momentum (Eliassen & Palm 1960, Blumen 1965a, Blumen 1965b, Bretherton 1969, Smith 1978, etc.), orographic clouds (Conover 1964), etc. In recent years, there has been interest growing in improving large scale atmospheric models such as GCMs by improving the characterization of the subgrid land surface. Topographically induced mesoscale flows are one of the processes that potentially have important impact on the performance of large scale models.

Early attempts in understanding the generation mechanisms of mountain waves using analytical models assumed very simple topographies. Queney (1948) showed that when the topography has an infinite sinusoidal (two-dimensional) profile, the magnitude of the disturbance decays upward exponentially for small wavelengths of the wavy surface, and remains constant with height for large wavelengths. For an isolated two-dimensional mountain, Queney found that a single symmetric wave dies away rapidly both vertically and horizon-

tally over a hill of small size (width about 100m). Over a larger hill (width up to a few kilometers) an asymmetric wave forms throughout the whole depth of the atmosphere, and decreases horizontally. Lee waves propagating several hundred kilometers horizontally are produced over large hills (width about 100km). Blumen (1965a) further studied the interaction between neighboring mountains with random spacings using the Fourier transform tool. He found that the effect produced by the interaction depends on whether the mean mountain spacing is less or greater than the shortest internal gravity waves. These results indicate that the length scale of the topography plays an important role in determining the fundamental features of the mountain waves. Smith (1979, 1989) provides comprehensive overviews of the mountain wave theories up to the late 80s.

Mountain waves could make a significant contribution to the vertical transport of horizontal momentum. It follows from two-dimensional linear (steady-state, non-rotating, and inviscid) theories that, in an environment of uniform Brunt-Väisälä frequency and background flow, there exists a momentum flux independent of height (Eliassen & Palm 1960). Hence a drag force acts on the atmosphere from the ground. It has been argued (e.g. Sawyer 1959) that the magnitude of this wave drag may be a significant fraction of the direct surface friction due to turbulence induced by surface roughness. Bretherton (1969) suggested that the most important wavelengths involved in the transport of momentum are between 10 km and 100 km, i.e. mesoscale mountains. Coriolis force also proves to be an important factor in mountain waves within a mesoscale domain, particularly in three-dimensional flow problems (Blumen 1965b, Lilly & Kennedy 1973, and Broad 1995). It has been suggested that the effect of topography induced subgrid flow should be taken into account in the parameterization schemes for the unresolved processes in the models for weather prediction and large scale atmospheric models such as GCMs (e.g. Palmer *et al.* 1986).

We note that the existing two- or three-dimensional linear models usually assume highly idealized topographies: sinusoidal ridges or isolated mountains of limited scope so that analytical solutions are feasible with the help of Fourier transform tools. Two serious problems arise with this approach. First, natural topography is far more complex than the above assumption. Observational studies (Young *et al.* 1983, Young *et al.* 1984, and Steyn *et al.*

1985) have shown that the topographic height has a continuous spectrum over a wide range of wavelengths. A continuous power-law spectrum with exponent somewhere between -1 and -2 has been identified by Bretherton (1969), and is supported by the work of Bannon & Yuhas (1990). It is unlikely that deterministic functions can sufficiently describe the variability of the natural topography. Thus, use of random functions is more appropriate to characterize the topography of complex terrains. A second problem is related to the use of the Fourier transform approach to seek analytical solutions for those cases where the irregularly variable topography covers a large area (Bretherton 1969). The Fourier transform approach can not be used to deal with the complex topography that extends to the entire large domain (idealized as an infinite domain in analytical modeling) since the Fourier transform of this type of topography does not exist.

In this chapter, these problems will be approached by proposing a three-dimensional stochastic linear theory similar to that for the thermally induced flow presented in Chapter 3. Again, the key step is to represent the complex topography as a two-dimensional random field characterized by a spectral density function or correlation function. The original governing equations for atmospheric flow link the random fields of the wind components, pressure, and temperature to the randomly variable topography as a boundary condition. Spectral representations of homogeneous random fields (e.g. Yaglom 1987) enable us to obtain a system of stochastic partial differential equations (SPDEs) that the random state variables must satisfy. The ensemble solution can then be derived by solving the SPDEs, in this case, analytically. Statistical properties, particularly the length scale properties, of the mountain waves are facilitated by analyzing the ensemble solution in the frequency domain. Area-averaged vertical transport of momentum and heat fluxes will be readily computed by doing integration in the frequency domain where the integrands are just the ensemble solution.

The static atmospheric stability and background flow in this stochastic linear model are assumed to be uniform over space and time. This is believed to be a reasonable assumption that helps to bring focus to the role of complex topography in the behavior of mountain waves. This simplification is necessary to ensure an analytical solution and proves to be a good starting point for deeper exploration.

5.2 Stochastic Modeling of 3D Mountain Waves

5.2.1 Governing Equations

Consider a transient, rotating, non-hydrostatic and dissipative Boussinesq atmospheric flow starting from rest. The dissipation effect is represented by Rayleigh-friction with a constant damping time. Analogous to the thermally induced flow studied in Chapter 2, the linearized three-dimensional governing equations for the airflow over a hilly terrain may be written as

$$\frac{\partial u}{\partial t} + u_0 \frac{\partial u}{\partial x} - fv = -\frac{\partial \phi}{\partial x} - \alpha u \tag{5.1}$$

$$\frac{\partial v}{\partial t} + u_0 \frac{\partial v}{\partial x} + fu = -\frac{\partial \phi}{\partial y} - \alpha v \tag{5.2}$$

$$\frac{\partial w}{\partial t} + u_0 \frac{\partial w}{\partial x} - b = -\frac{\partial \phi}{\partial z} - \alpha w \tag{5.3}$$

$$\frac{\partial b}{\partial t} + u_0 \frac{\partial b}{\partial x} + N^2 w = -\alpha b \tag{5.4}$$

$$\frac{\partial u}{\partial x} + \frac{\partial v}{\partial y} + \frac{\partial w}{\partial z} = 0 \tag{5.5}$$

where u, v and w are the perturbed wind components due to topography, b is the perturbed buoyancy, ϕ is the perturbed geopotential, f is the Coriolis parameter, N is the Brunt-Väisälä frequency, and u_0 is the large scale flow. N and u_0 are assumed to be uniform in space and time to keep the mathematics tractable.

5.2.2 Boundary Conditions

Solving Eq (5.1) - (5.5) requires boundary conditions at surface and infinite height. An approriate boundary condition at the surface is that the flow will follow the profile of topography, or equivalently, the projection of the wind velocity vector in the direction of the surface normal vector is zero (Smith, 1989),

$$\vec{v} \cdot \nabla \{z - h(x, y)\} = 0 \tag{5.6}$$

where $h(x, y)$ is the topographic height and ∇ is the gradient operator

$$\nabla = (\frac{\partial}{\partial x}, \frac{\partial}{\partial y}, \frac{\partial}{\partial z}).$$

The wind velocity vector $\vec{v}$ is composed of large scale flow u_0 and topographically induced mesoscale flow u, v, w

$$\vec{v} = (u_0 + u, v, w). \tag{5.7}$$

Combining (5.6) and (5.7) leads to

$$w = u_0 \frac{\partial h}{\partial x} + u \frac{\partial h}{\partial x} + v \frac{\partial h}{\partial y} \tag{5.8}$$

at the surface $z = h(x, y)$. Eq (5.8) is a nonlinear boundary condition due to the product terms of u, v and h. It has been shown (e.g. Smith 1980) that under the conditions of small amplitude of topography and mesoscale flow, i.e.

$$\frac{H_0 N}{u_0} < 1 \tag{5.9}$$

$$u, v < u_0 \tag{5.10}$$

where H_0 is a characteristic height of mountain barrier, Eq (5.8) may be linearized as

$$w \mid_{z=0} = u_0 \frac{\partial h(x, y)}{\partial x} \tag{5.11}$$

where $z = 0$ locates at the actual level of domain-mean height h_0. Eq. (5.11) is a mathematically convenient condition for a possible analytical solution. Loosely speaking, z could be interpreted as the distance in the normal direction of the surface profile. Validity of this approximate boundary condition is limited to the cases of mountains with height lower than 1000 m.

At infinite height, the boundary condition takes the form

$$\lim_{z \to \infty} \mid u, v, w, b, \phi \mid < \infty. \tag{5.12}$$

Equation (5.12) simply states that the amplitudes of the perturbed flow are finite.

5.2.3 The Statistical Description of Topography

Topographic height h, without loss of generality, can be decomposed into a domain-mean h_0 and a perturbation around h_0, h', so

$$h(x, y) = h_0 + h'(x, y). \tag{5.13}$$

When the statistical properties of topography do not vary over the domain of interest, h' can be modeled as a 2D homogeneous random field characterized by a spectrum $\sigma_h^2 S_h$. The spectral density function S_h describes the distribution of the variability (standard deviation σ_h) of topographic height over length scales. Using the spectral representation of a homogeneous random field (Yaglom 1987), we may write

$$h' = \int_{-\infty}^{\infty}\int_{-\infty}^{\infty} \mathrm{e}^{i(k_1 x + k_2 y)} dZ_h(k_1, k_2) \tag{5.14}$$

where dZ_h is a zero-mean independent random variable in frequency domain (k_1, k_2). dZ_h, the counterpart of h' in physical domain (x, y), relates to the spectrum $\sigma_h^2 S_h$ in the form

$$\mathrm{E}[dZ_h(k_1, k_2) dZ_h^*(k_3, k_4)] = 0 \quad \text{for} \quad (k_1, k_2) \neq (k_3, k_4) \tag{5.15}$$

$$\mathrm{E}[\mid dZ_h(k_1, k_2) \mid^2] = \sigma_h^2 S_h(k_1, k_2) dk_1 dk_2 \tag{5.16}$$

where $\mathrm{E}[\cdot]$ represents mathematical expectation.

5.3 Analytical Solution

5.3.1 Decomposition and the Spectral Representation

Randomness in topography, the external forcing for mountain waves, makes all dependent variables in Eqs. (5.1) through (5.5) random. Given the linearity of the governing equations

it is safe to assume that if the forcing is horizontally homogeneous, the dependent variables will be horizontally homogeneous also.

Again using a spectral representation of the perturbed state variables u, v, w, b, and ϕ in the governing Eqs. (5.1) - (5.5) leads to the following expressions

$$u = \int_{-\infty}^{\infty}\int_{-\infty}^{\infty} e^{i(k_1 x+k_2 y)} dZ_u(k_1,k_2;z,t) \tag{5.17}$$

$$v = \int_{-\infty}^{\infty}\int_{-\infty}^{\infty} e^{i(k_1 x+k_2 y)} dZ_v(k_1,k_2;z,t) \tag{5.18}$$

$$w = \int_{-\infty}^{\infty}\int_{-\infty}^{\infty} e^{i(k_1 x+k_2 y)} dZ_w(k_1,k_2;z,t) \tag{5.19}$$

$$b = \int_{-\infty}^{\infty}\int_{-\infty}^{\infty} e^{i(k_1 x+k_2 y)} dZ_b(k_1,k_2;z,t) \tag{5.20}$$

$$\phi = \int_{-\infty}^{\infty}\int_{-\infty}^{\infty} e^{i(k_1 x+k_2 y)} dZ_\phi(k_1,k_2;z,t) \tag{5.21}$$

where dZ_u, dZ_v, dZ_w, dZ_b, and dZ_ϕ are independent random variables in the frequency domain, corresponding to u, v, w, b, and ϕ in the physical domain respectively.

5.3.2 Governing Equations in the Frequency Domain

The governing equations for dZs can be readily derived by substituting Eqs. (5.17) through (5.21) into Eqs. (5.1) through (5.5) as follows,

$$(\frac{\partial}{\partial t} + \alpha + ik_1u_0)dZ_u - f dZ_v = -ik_1 dZ_\phi \tag{5.22}$$

$$(\frac{\partial}{\partial t} + \alpha + ik_1u_0)dZ_v + f dZ_u = -ik_2 dZ_\phi \tag{5.23}$$

$$(\frac{\partial}{\partial t} + \alpha + ik_1u_0)dZ_w - dZ_b = -\frac{\partial}{\partial z} dZ_\phi \tag{5.24}$$

$$(\frac{\partial}{\partial t} + \alpha + ik_1u_0)dZ_b + N^2 dZ_w = 0 \tag{5.25}$$

$$ik_1 dZ_u + ik_2 dZ_v + \frac{\partial}{\partial z} dZ_w = 0 \tag{5.26}$$

The boundary and initial conditions in the frequency domain are

$$dZ_w\,|_{z=0} = ik_1u_0 dZ_h \tag{5.27}$$

$$\lim_{z\to\infty} \mid dZ_u, dZ_v, dZ_w, dZ_b, dZ_\phi \mid \; < \; \infty \tag{5.28}$$

and

$$dZ_u, dZ_v, dZ_w, dZ_b, dZ_\phi \mid_{t=0} = 0 \tag{5.29}$$

5.3.3 Solution for the dZ's

The analytical solution of Eqs. (5.22) through (5.26) under the prescribed initial and boundary conditions (5.27), (5.28) and (5.29) is shown below while the detailed derivation is given in Appendix E.

Transient Solution

a) when $N \neq f$

$$dZ_u = \frac{2k_1u_0}{\pi k}\{\int_a^b \cos(zkG(\xi))G(\xi)\frac{\xi k_1 I_s(t,\xi;u_0,\alpha) - fk_2 I_c(t,\xi;u_0,\alpha)}{\xi}d\xi\}dZ_h \tag{5.30}$$

$$dZ_v = \frac{2k_1u_0}{\pi k}\{\int_a^b \cos(zkG(\xi))G(\xi)\frac{\xi k_2 I_s(t,\xi;u_0,\alpha) + fk_1 I_c(t,\xi;u_0,\alpha)}{\xi}d\xi\}dZ_h \tag{5.31}$$

$$dZ_w = -\frac{2ik_1u_0}{\pi}\{\int_a^b \sin(zkG(\xi))I_s(t,\xi;u_0,\alpha)d\xi\}dZ_h \tag{5.32}$$

$$dZ_b = -\frac{2ik_1u_0N^2}{\pi}\{\int_a^b \sin(zkG(\xi))\frac{I_c(t,\xi;u_0,\alpha)}{\xi}d\xi\}dZ_h \tag{5.33}$$

$$\begin{aligned} dZ_\phi = \frac{2ik_1u_0}{\pi k}[\int_a^b &\cos(zkG(\xi))G(\xi)\{\sin(\xi t) + \\ &\frac{\xi(\alpha + ik_1u_0)I_s(t,\xi;u_0,\alpha) - f^2 I_c(t,\xi;u_0,\alpha)}{\xi}\}d\xi]dZ_h \end{aligned} \tag{5.34}$$

b) when $N = f$

$$dZ_u = \frac{k_1u_0}{k}\{k_1 + fk_2\frac{1-\mathrm{e}^{-(\alpha+ik_1u_0)t}}{\alpha+ik_1u_0}\}\mathrm{e}^{-zk}dZ_h \tag{5.35}$$

$$dZ_v = \frac{k_1 u_0}{k}\{k_2 - f k_1 \frac{1 - \mathrm{e}^{-(\alpha + ik_1 u_0)t}}{\alpha + ik_1 u_0}\}\mathrm{e}^{-zk} dZ_h \tag{5.36}$$

$$dZ_w = ik_1 u_0 \mathrm{e}^{-zk} dZ_h \tag{5.37}$$

$$dZ_b = -k_1 u_0 f^2 \{\frac{1 - \mathrm{e}^{-(\alpha + ik_1 u_0)t}}{\alpha + ik_1 u_0}\}\mathrm{e}^{-zk} dZ_h \tag{5.38}$$

$$dZ_\phi = \frac{k_1 u_0}{k}\{\delta(t) + \alpha + ik_1 u_0 + f^2 \frac{1 - \mathrm{e}^{-(\alpha + ik_1 u_0)t}}{\alpha + ik_1 u_0}\}\mathrm{e}^{-zk} dZ_h \tag{5.39}$$

where

$$[a, b] = [\min\{f, N\}, \max\{f, N\}] \tag{5.40}$$

$$G(\xi) = \mid \frac{N^2 - \xi^2}{f^2 - \xi^2} \mid^{\frac{1}{2}} \tag{5.41}$$

$$I_s(t, \xi; u_0, \alpha) = \int_0^t \sin(\xi\tau)\mathrm{e}^{-(\alpha + ik_1 u_0)\tau} d\tau \tag{5.42}$$

$$I_c(t, \xi; u_0, \alpha) = \int_0^t \cos(\xi\tau)\mathrm{e}^{-(\alpha + ik_1 u_0)\tau} d\tau \tag{5.43}$$

Here, $\delta(t)$ is a Dirac delta function. ξ is a dummy integration variable. The functional forms of the integrals on the right of (5.42) and (5.43) are given in Appendix F. The other symbols are specified in Appendix A.

The ensemble solution (5.30) through (5.39) describes the general transient process of the atmosphere initially at rest. The possible steady-state solution can be derived from this transient solution under general initial and boundary conditions.

Steady-state Solution

A steady-state solution is obtained by letting $t \to \infty$ in the transient solution

$$dZ_u = \frac{k_1 u_0}{k}\{\frac{k_1(\alpha + ik_1u_0) + fk_2}{\alpha + ik_1u_0}\}\hat{T}(k_1)\mathrm{e}^{\mp zk\hat{T}(k_1)}dZ_h \tag{5.44}$$

$$dZ_v = \frac{k_1 u_0}{k}\{\frac{k_2(\alpha + ik_1u_0) - fk_1}{\alpha + ik_1u_0}\}\hat{T}(k_1)\mathrm{e}^{\mp zk\hat{T}(k_1)}dZ_h \tag{5.45}$$

$$dZ_w = ik_1u_0\mathrm{e}^{\mp zk\hat{T}(k_1)}dZ_h \tag{5.46}$$

$$dZ_b = -ik_1u_0\{\frac{N^2}{\alpha + ik_1u_0}\}\mathrm{e}^{\mp zk\hat{T}(k_1)}dZ_h \tag{5.47}$$

$$dZ_\phi = \frac{ik_1u_0}{k}\{\frac{(\alpha + ik_1u_0)^2 + f^2}{\alpha + ik_1u_0}\}\hat{T}(k_1)\mathrm{e}^{\mp zk\hat{T}(k_1)}dZ_h \tag{5.48}$$

where

$$\hat{T}^2(k_1) = \frac{(\alpha + ik_1u_0)^2 + N^2}{(\alpha + ik_1u_0)^2 + f^2} \tag{5.49}$$

and the minus sign in $\mp$ corresponds to the case where $\mathrm{Re}(\hat{T})$ is positive, and the plus sign to the case where $\mathrm{Re}(\hat{T})$ is negative. Re() returns the real part of its argument.

This solution deserves further discussion. The existence of a steady-state solution stems from the non-zero value of α. In other words, flow induced by topography will not reach steady-state unless there is a dissipation process that balances the constant disturbance energy from the ground into the air when the atmosphere is initially at rest. When using steady-state governing equations without the time-derivative terms in Eq. (5.1) - (5.5), we found that an inviscid steady-state solution (results and derivations not shown here) can be obtained by letting α go to zero in solution (5.44) - (5.48). In this case, it takes a very long time for the flow to reach steady-state. This fact implies that a certain dissipation mechanism is necessary for the existence of steady-state of mountain waves although the process through which this steady-state is reached may not be of concern.

At steady-state, the dissipation coefficient α still plays an important role in the propaga-

tion of mountain waves. The vertical distribution of the wave disturbances is represented by the term $e^{\mp zk\hat{T}}$ in solution (5.44) through (5.48). Specifically, dissipation affects the vertical profile of mountain waves through the dependence of $\hat{T}$ function on α as shown in (5.49). It can be shown (see Appendix D) that the real part of $\hat{T}(k_1)$ will have non-zero value for $\alpha \neq 0$. Consequently the amplitudes of mountain waves decay upward.

When the dissipation vanishes (i.e. $\alpha = 0$), Eq. (5.49), which is valid for $\alpha \geq 0$ as discussed above, reduces to

$$\hat{T}(k_1) = \sqrt{\frac{k_1^2 u_0^2 - N^2}{k_1^2 u_0^2 - f^2}} \tag{5.50}$$

Therefore, $\hat{T}(k_1)$ is either purely imaginary or positive depending on the value of wave number k_1. Keep in mind that k_1 is inversely proportional to the length scale of topographic height in the direction of background flow. In other words, the statistical properties of topography in the direction of background flow determine the fundamental feature of the vertical profiles of mountain waves. $\hat{T}(k_1)$ is purely imaginary when wave number k_1 satisfies

$$\frac{f}{u_0} < k_1 < \frac{N}{u_0} \tag{5.51}$$

and is non-negative otherwise. The right half of the inequality (5.51) is consistent with the well-known classical result (Scorer 1949) based upon a two-dimensional, linear, non-rotating and inviscid model. The left half of the inequality is due to the effect of Coriolis force. For typical values of N ($\sim 10^{-2}$ s^{-1}), f($\sim 10^{-4}$ s^{-1}) and u_0 (~ 10 m s^{-1}), (5.51) corresponds to a range of length scales between 6 km and 600 km. Over this range the amplitude of mountain waves do not decay with height for $\alpha = 0$. Topography with length scales either less than 6 km or greater than 600 km will cause perturbations that decay upwards. An earlier study (e.g. Bretherton 1969) suggested that topography with length scales between 10 km and 100 km contributes the most to the transport of momentum. Hence, we expect that the wave energy carried by mountain waves over complex mesoscale terrains could reach very high levels when the dissipation effect of the atmosphere is not important.

It is worth emphasizing that this stochastic theory predicts that the fundamental features of the vertical distribution of steady-state mountain waves over complex terrains depend only

on the length scale properties of topographic height parallel to the constant background flow since $\hat{T}$ is a function of k_1 alone. This observation justifies predictions of the behavior of mountain waves by two-dimensional models.

For the sake of brevity, we rewrite the solution given in (5.30) through (5.48) as

$$dZ_u = \Pi_u(k_1, k_2)dZ_h \tag{5.52}$$

$$dZ_v = \Pi_v(k_1, k_2)dZ_h \tag{5.53}$$

$$dZ_w = \Pi_w(k_1, k_2)dZ_h \tag{5.54}$$

$$dZ_b = \Pi_b(k_1, k_2)dZ_h \tag{5.55}$$

$$dZ_\phi = \Pi_\phi(k_1, k_2)dZ_h \tag{5.56}$$

where Π functions in general vary with both height and time.

5.4 Statistics of the Mountain Waves

Analogous to the stochastic linear analysis conducted in Chapter 3, the statistics of the topography induced flow are expressed in terms of the standard deviations of the wind components, σ_u, σ_v and σ_w. The corresponding frequency response Π functions contain the length scale properties of the mountain waves.

For most of practical purposes, steady-state flow is of more interest than transient flow, hence will be the focus of the discussions.

5.4.1 The Properties of the Spatial Length Scale of Mountain Waves

The analysis of the length scale properties of mountain waves is facilitated by examining the frequency response functions Π_i defined in Eq. (5.52) - (5.56). Frequency response functions fully characterize the input (topography)-output (mountain waves) relation of a linear dynamic system (atmosphere) when its variability is decomposed over wave numbers k_1 and k_2.

One fundamental feature of the Π functions (except Π_ϕ) is that their amplitudes vanish when the wave number k goes to either zero or infinity according to (5.30) through (5.48). This behavior suggests that the variable topography of large length scale (flat ground) or of small length scale is not expected to induce significant mesoscale flow. A logical conclusion would be that there must exist a certain wave number $(\tilde{k}_1, \tilde{k}_2)$ at which the amplitude of Π function reaches its maximum value. For the purpose of illustration, we choose vertical velocity w and seek $(\tilde{k}_1, \tilde{k}_2)$ at which $\mid \Pi_w \mid^2$ takes maximum value.

The steady-state solution for dZ_w, (5.46), leads to

$$\mid \Pi_w(k_1, k_2) \mid^2 = k_1^2 u_0^2 \mathrm{e}^{-2zk|\mathrm{Re}(\hat{T}(k_1))|} \tag{5.57}$$

The maximum of the $\mid \Pi_w \mid^2$ function in (5.57) occurs when $(\tilde{k}_1, \tilde{k}_2)$ satisfies the following equations

$$\frac{\partial \mid \Pi_w(k_1, k_2) \mid^2}{\partial k_1} \mid_{(\tilde{k}_1, \tilde{k}_2)} = 0 \tag{5.58}$$

$$\frac{\partial \mid \Pi_w(k_1, k_2) \mid^2}{\partial k_2} \mid_{(\tilde{k}_1, \tilde{k}_2)} = 0 \tag{5.59}$$

The solution of Eq. (5.59) is

$$\tilde{k}_2 = 0 \tag{5.60}$$

The solution (5.60) means that the possible strongest perturbed vertical velocity corresponds to infinitely long two-dimensional ridges in the direction perpendicular to mean flow. In other words, the presence of three-dimensional mountain barriers tends to reduce the amplitude of the perturbed vertical velocity. This result is intuitively reasonable since the air has to pass over instead of going around the two-dimensional ridges.

The solution of Eq. (5.58) is expressed as an implicit function of $\tilde{k}_1$

$$\{zk_1 \frac{\partial}{\partial k_1}[k_1 \mathrm{Re}(\hat{T}(k_1))]\}_{k_1 = \tilde{k}_1} = 1 \tag{5.61}$$

The value of $\tilde{k}_1$ is better illustrated graphically due to the lack of simple analytical expression

for $\tilde{k}_1$.

Figure 5-1 shows $\mid \Pi_w(k_1, 0) \mid^2$ as a function of k_1 and z for non-dissipative atmosphere with $\hat{T}$ given in (5.50). Three regimes of $\mid \Pi_w \mid^2$ with respect to k_1 can be identified at fixed height z according to (5.51): **1)** $k_1 < f/u_0$ ($\log_{10}[k_1 u_0/N] < -2$ on the log scale used in Fig. 5-1); **2)** $f/u_0 < k_1 < N/u_0$ ($-2 < \log_{10}[k_1 u_0/N] < 0$); and **3)** $k_1 > N/u_0$ ($\log_{10}[k_1 u_0/N] > 0$) when f, N and u_0 take the same value as used in section 5.3.3. Within region **1**, $\mid \Pi_w \mid^2$ first increases with increasing k_1 to its local maximum, then decreases rapidly until k_1 hits the region boundary (-2 on the log scale in Fig. 5-1). In region **2**, $\mid \Pi_w \mid^2$ increases monotonically with increasing k_1. In region **3**, $\mid \Pi_w \mid^2$ first increases with increasing k_1 to reach its local maximum, and then decreases rapidly. Comparing the two local maxima in regions **1** and **3**, we find that $\mid \Pi_w \mid^2$ attains global maximum in region **3**, i.e. $\tilde{k}_1 > N/u_0$.

The global maxima of $\mid \Pi_w \mid^2$ corresponds to the most favorable length scale (defined as $2\pi/\tilde{k}_1$) of the topography that generates mountain waves. The variability of topography with length scales around this most favorable length scale is expected to induce significant mountain waves. In general, $\tilde{k}_1$ decreases with height, indicating that the topography of larger length scales is more efficient in inducing perturbations at higher levels. Fig. 5-1 illustrates that $\tilde{k}_1$ is convergent rapidly to N/u_0 (10^{-3} m^{-1}) as height z increases. At levels no lower than 1 km, $\tilde{k}_1$ corresponds to a length scale of about 6 km.

Figure 5-2 illustrates the influence of dissipation on the function $\mid \Pi_w \mid^2$. The discontinuity of $\mid \Pi_w \mid^2$ at the boundaries between region **2** and region **1** and **3** as a function of k_1 shown in Fig. 5-1 no longer exists due to the presence of dissipation. Within region **2**, dissipation results in a dependence of $\mid \Pi_w \mid^2$ on height, in contrast to the case of non-dissipative atmosphere. Dissipation also tends to constrain the influence of the mountain waves within the depth of the troposphere. Fig. 5-2 shows that the global maximum $\mid \Pi_w \mid^2$ is reached at $\tilde{k}_1 \sim 10^{-3}$ m^{-1} above 1 km level. It corresponds to the most favorable length scale of the topography for generating mountain waves. The value of this most favorable length scale is approximately $2\pi u_0/N \sim 6$ km. This is the same as in the non dissipative case and there is no significant difference between the values in Fig. 5-1 and Fig. 5-2 of the $\mid \Pi_w \mid^2$ function below the zero point on the ordinate (logarithm of normalized height z). Again,

the length scale estimate is based on the representative values of N and u_0 used in section 5.3.3. Therefore, the impact of dissipation on the magnitude of $\mid \Pi_w \mid^2$ is relatively weak within the lowest 1 km layer. We note that Fig. 5-1 is the limiting case of Fig. 5-2 as α goes to zero. We conclude that dissipation plays an important role in determining the vertical distribution of waves beyond the lowest 1 km layer.

5.4.2 Properties of σ_i

Using the solution of dZ_u, dZ_v and dZ_w given in Eq. (5.44) - (5.46), the variances of the wind components can be computed as,

$$\begin{aligned}\sigma_u^2(z) &= \mathrm{E}[dZ_u dZ_u^*] \\ &= \sigma_h^2 \int_{-\infty}^{\infty}\int_{-\infty}^{\infty} \frac{k_1^2 u_0^2}{k^2} \frac{(\alpha^2 + k_1^2 u_0^2)k_1^2 + f^2 k_2^2}{\alpha^2 + k_1^2 u_0^2} \mid \hat{T} \mid^2 \mathrm{e}^{-2zk|\mathrm{Re}(\hat{T})|} S_h(k_1, k_2) dk_1 dk_2 \end{aligned} \quad (5.62)$$

$$\begin{aligned}\sigma_v^2(z) &= \mathrm{E}[dZ_v dZ_v^*] \\ &= \sigma_h^2 \int_{-\infty}^{\infty}\int_{-\infty}^{\infty} \frac{k_1^2 u_0^2}{k^2} \frac{(\alpha^2 + k_1^2 u_0^2)k_2^2 + f^2 k_1^2}{\alpha^2 + k_1^2 u_0^2} \mid \hat{T} \mid^2 \mathrm{e}^{-2zk|\mathrm{Re}(\hat{T})|} S_h(k_1, k_2) dk_1 dk_2 \end{aligned} \quad (5.63)$$

$$\begin{aligned}\sigma_w^2(z) &= \mathrm{E}[dZ_w dZ_w^*] \\ &= \sigma_h^2 \int_{-\infty}^{\infty}\int_{-\infty}^{\infty} k_1^2 u_0^2 \mathrm{e}^{-2zk|\mathrm{Re}(\hat{T})|} S_h(k_1, k_2) dk_1 dk_2 \end{aligned} \quad (5.64)$$

The functional form of the spectral density function of topography, $S_h(k_1, k_2)$, needs to be specified to compute σ_u^2, σ_v^2 and σ_w^2 in (5.62) through (5.64). As discussed in Chapter 2, observational studies have suggested S_h follows a power-law within a wide range of length scales. For mesoscale terrains, the exponential index was somewhere between -1 and -2.5. In this study we use -1.5 as the power-law exponent and further assume this power-law spectrum covers length scales from 1 km to 200 km for the purpose of illustration.

σ_u^2, σ_v^2 and σ_w^2 as a function of height z are shown in Fig. 5-3 for different values of α (10^{-5} and 10^{-4} s^{-1}) and a typical value of u_0 (10 m s^{-1}). Fig. 5-3 illustrates that all of them decay rapidly upward. The topography induced flow in the direction of the synoptic wind is

stronger than in the perpendicular direction.

5.5 Water Balance in the Atmosphere

5.5.1 Governing Equations

Following the same procedure to derive the linearized water balance equation as in Chapter 3 for the thermally induced flow, the linearized water balance for the topographically induced flow is written as

$$\frac{\partial q'}{\partial t} + u_0 \frac{\partial q'}{\partial x} + w' \frac{d\bar{q}}{dz} = 0 \tag{5.65}$$

where the symbols in Eq. (5.65) are the same as those used in Eq. (3.63).

With the help of spectral representation of homogeneous random field, q' is expresses as

$$q' = \int_{-\infty}^{\infty}\int_{-\infty}^{\infty} \mathrm{e}^{i(k_1 x + k_2 y)} dZ_q(k_1, k_2; z, t) \tag{5.66}$$

Combining Eq (5.65) and Eq (5.66) leads to the governing equation for dZ_q in the frequency domain

$$\frac{\partial}{\partial t}(dZ_q) + ik_1 u_0 dZ_q = -\frac{d\bar{q}(z)}{dz} dZ_w \tag{5.67}$$

5.5.2 Analytical Solution

Transient Solution

The solution of transient process q' described by Eq (5.67) is given as follows

a) when $N \neq f$

$$\begin{aligned} dZ_q \;=\; & -\frac{d\bar{q}(z)}{dz}[\mathrm{e}^{-zk\hat{T}} - \mathrm{e}^{-zk\hat{T}_0}\mathrm{e}^{-ik_1u_0t} - \frac{2i}{\pi} \\ & \int_a^b \sin(zkG(\xi)) \frac{\{\xi^2 + \alpha(\alpha + ik_1u_0)\}I_c + \xi(2\alpha + ik_1u_0)I_s}{(\xi^2+\alpha^2)\{\xi^2 + (\alpha + ik_1u_0)^2\}} d\xi] dZ_h \end{aligned} \tag{5.68}$$

where $G(\xi)$, I_s and I_c are given in (5.41), (5.42) and (5.43), respectively. And

$$\hat{T}_0^2 = \frac{\alpha^2 + N^2}{\alpha^2 + f^2} \tag{5.69}$$

b) when $N = f$

$$dZ_q = -\frac{d\bar{q}(z)}{dz}\{1 - \mathrm{e}^{-ik_1u_0t}\}\mathrm{e}^{-zk}dZ_h \tag{5.70}$$

The steady-state solution can not be obtained as a limiting case by letting $t \to \infty$ in the transient solution (5.68) and (5.70) due to the oscillating term $\mathrm{e}^{-ik_1u_0t}$. Therefore, a steady-state water balance equation is needed to derive the steady-state solution.

A linearized steady-state water balance equation can be obtained by dropping the time-derivative term is Eq. (5.65)

$$u_0\frac{\partial q'}{\partial x} + w'\frac{d\bar{q}}{dz} = 0 \tag{5.71}$$

In the frequency domain, Eq. (5.71) becomes

$$ik_1u_0dZ_q = -\frac{d\bar{q}(z)}{dz}dZ_w \tag{5.72}$$

Using the steady-state solution for dZ_w given in (5.46), we have:

Steady-State Solution

$$dZ_q = -\frac{d\bar{q}(z)}{dz}\mathrm{e}^{\mp zk\hat{T}(k_1)}dZ_h \tag{5.73}$$

The solution of dZ_q could be written in a short form

$$dZ_q = \Pi_q(k_1, k_2)dZ_h \tag{5.74}$$

where the frequency response function Π_q is a function of height only for steady-state flow, but a function of both height and time for transient flow.

5.6 The Vertical Transport of Momentum, Heat, and Moisture

The discussion in this section focuses on steady-state flow.

5.6.1 Momentum Fluxes (Wave Drag)

The vertical fluxes of horizontal momentum M_x and M_y due to the wind components u and v in x and y direction are defined as

$$M_x = \overline{wu} \tag{5.75}$$

$$M_y = \overline{wv} \tag{5.76}$$

where the overbars stand for realization mean over horizontal domain.

With the help of the spectral representations for the wind components given in (5.17) - (5.19), the realization mean in the physical domain (x, y) can be replaced by the ensemble average in the frequency domain (k_1, k_2),

$$\begin{aligned} M_x &= \int_{-\infty}^{\infty}\int_{-\infty}^{\infty} \mathrm{E}[dZ_w(k_1,k_2)dZ_u^*(k_1,k_2)] \\ &= \int_{-\infty}^{\infty}\int_{-\infty}^{\infty} \Pi_w(k_1,k_2)\Pi_u^*(k_1,k_2)\sigma_h^2 S_h(k_1,k_2)dk_1dk_2 \end{aligned} \tag{5.77}$$

$$\begin{aligned} M_y &= \int_{-\infty}^{\infty}\int_{-\infty}^{\infty} \mathrm{E}[dZ_w(k_1,k_2)dZ_v^*(k_1,k_2)] \\ &= \int_{-\infty}^{\infty}\int_{-\infty}^{\infty} \Pi_w(k_1,k_2)\Pi_v^*(k_1,k_2)\sigma_h^2 S_h(k_1,k_2)dk_1dk_2 \end{aligned} \tag{5.78}$$

Substituting the analytical solution of dZ's in (5.44) through (5.46) into (5.77) and (5.78) leads to the expressions for M_x and M_y

$$M_x = \sigma_h^2 \int_{-\infty}^{\infty}\int_{-\infty}^{\infty} \frac{k_1^2 u_0^2}{k}[k_1 \sin\frac{\beta(k_1)}{2}] \mid \hat{T} \mid \mathrm{e}^{-2zk|\mathrm{Re}(\hat{T})|} S_h(k_1,k_2)dk_1dk_2 \tag{5.79}$$

$$M_y = \sigma_h^2 f \int_{-\infty}^{\infty}\int_{-\infty}^{\infty} \frac{k_1^2 u_0^2}{k} \frac{1}{\alpha^2 + k_1^2 u_0^2} [k_1^2 u_0 \cos\frac{\beta(k_1)}{2} - k_1 \alpha \sin\frac{\beta(k_1)}{2}] \\ | \hat{T} | \, e^{-2zk|\mathrm{Re}(\hat{T})|} S_h(k_1, k_2) dk_1 dk_2 \tag{5.80}$$

where $\hat{T}$ is given in (5.49), and $\beta(k_1)$ is computed using (G.14) in Appendix G.

M_x and M_y as a function of height z are shown in Fig. 5-4 for different values of α and a typical value of u_0 (10 m s^{-1}). The value of M_x is found to be about one order of magnitude larger than M_y. Hence, the major contribution to the vertical transport of momentum is due to the topographically induced flow in the direction of background wind. M_y, resulting from the Coriolis force according to Eq. (5.80), only shows up within a thin layer near the ground.

It is evident from (5.79) and (5.80) that M_x and M_y are zero when the synoptic wind u_0 is zero. Eq. (5.79) also shows that M_x will be vanishing when synoptic wind becomes very strong ($\sim$ 100 m s^{-1}). Eq. (5.80) shows that M_y increases with synoptic wind u_0 slowly. For realistic values of synoptic wind u_0 (e. g. 1 m s^{-1} $\sim$ 50 m s^{-1}), the value of M_x/σ_h^2 is on the order of 10^{-6}, while the value of M_y/σ_h^2 ranges from $\sim 10^{-8}$ to $\sim 10^{-7}$. In general, M_y is at least one order of magnitude smaller than, hence much less important than M_x.

The influence of dissipation on M_x is mainly on the shape of its vertical distribution, rather than on its magnitude. As the dissipation parameter α decreases to zero, the classical results for non-dissipative atmosphere can be retrieved. For example, Elliasen (1965) has shown that M_x is independent of height based on a linear theory for inviscid flow. Comparing (a) with (b) in Fig. 5-4 reveals that the dependence of M_x on height becomes much weaker as α decreasing by a factor of ten. At the same time, the impact of α on M_y is relatively weak.

When $\sigma_h \sim$ 300 m, M_x is on the order of 0.2 m^2 s^{-2}, considerably larger than the typical value of turbulent momentum flux in the atmospheric boundary layer ($\sim$ 0.05 m^2 s^{-2} according to Stull (1988)). For non-dissipative atmosphere ($\alpha = 0$), $\beta(k_1)$ in (5.79) and (5.80) turns out to be π for $f/u_0 < k_1 < N/u_0$, and zero otherwise. Hence, mesoscale topography is solely responsible for momentum flux M_x. This result is consistent with that predicted by 2D small-amplitude mountain wave theories (e.g. Eliassen & Palm 1960).

5.6.2 Heat Flux

Analogous to momentum fluxes, the vertical flux of heat associated with the mountain waves, H, can be defined as the horizontal domain averaged product of potential temperature θ and vertical velocity w,

$$H = \rho C_p \overline{w\theta}, \tag{5.81}$$

where θ related to buoyancy b in the form

$$\theta = \frac{\theta_0}{g} b.$$

Spectral representation (5.20) for b leads to its counterpart in the frequency domain,

$$dZ_\theta = \frac{\theta_0}{g} dZ_b,$$

where θ_0 is a reference potential temperature.

The realization mean over the physical domain (x, y) in (5.81) is, again, equivalent to the ensemble mean in the frequency domain (k_1, k_2) based on the same argument for the momentum fluxes,

$$\begin{aligned} H &= \frac{\rho C_p \theta_0}{g} \int_{-\infty}^{\infty}\int_{-\infty}^{\infty} \mathrm{E}[dZ_w(k_1,k_2) dZ_\theta^*(k_1,k_2)] \\ &= \frac{\rho C_p \theta_0}{g} \int_{-\infty}^{\infty}\int_{-\infty}^{\infty} \Pi_w(k_1,k_2)\Pi_\theta^*(k_1,k_2)\sigma_h^2 S_h(k_1,k_2) dk_1 dk_2. \end{aligned} \tag{5.82}$$

The heat flux H can be further expressed using the analytical solution (5.46) and (5.47) as,

$$H = -\frac{\rho C_p \theta_0 \sigma_h^2 N^2 \alpha}{g} \int_{-\infty}^{\infty}\int_{-\infty}^{\infty} \frac{k_1^2 u_0^2}{\alpha^2 + k_1^2 u_0^2} \mathrm{e}^{-2zk|\mathrm{Re}(\hat{T})|} S_h(k_1,k_2) dk_1 dk_2. \tag{5.83}$$

Equation (5.83) implies that there will be no heat flux for non-dissipative atmosphere ($\alpha = 0$) since the atmospheric flow is adiabatic for $\alpha = 0$. This linear theory predicts a downward transport of heat when dissipation is modeled in terms of Rayleigh-friction with constant damping time. The negative value of the heat flux is due to stable stratification where

potential temperature increases with height. The integrand in (5.83), as a function of wave number k, behaves similarly to the integrands in (5.79) and (5.80). Thus the mesoscale variability of topography makes the most significant contribution to the vertical transport of heat in a dissipative atmosphere.

Figure 5-5 illustrates the vertical distribution of heat flux H for different values of α and a typical value of u_0. The dissipation rate α has the most important influence on the heat flux. The value of H is nearly proportional to the value of α as shown in (5.83), and decreases with height. Again zero synoptic wind leads to a zero heat flux H according to (5.83). For large synoptic winds Eq. (5.83) predicts that heat flux H becomes insensitive to wind and decreases rapidly with height.

For the typical values of the parameters, e.g. $\theta_0 = 300$ K, $N = 10^{-2}$ s^{-1}, $\sigma_h \sim 300$ m, $\alpha \sim 10^{-4}$ s^{-1}, $C_p = 10^3$ J kg^{-1} K^{-1}, $g = 9.8$ m s^{-2}, the magnitude of H is on the order of 10^1 W m^{-2}. This value is considerably smaller than the typical value ($\sim 10^2$ W m^{-2}) of turbulent heat flux within the atmospheric boundary layer. Thus, mountain waves are not an efficient process in terms of vertical transport of heat. Therefore, heat flux associated with a topographically induced flow may not be of a serious concern in the parameterization of unresolved subgrid processes in large scale atmospheric models.

5.6.3 Moisture Flux

Moisture flux transported by the mountain waves, E, is defined as the horizontal domain averaged product of specific humidity q and vertical velocity w,

$$E = \overline{wq}, \tag{5.84}$$

Analogous to the heat flux, the realization mean over the physical domain (x, y) in (5.84) equals the ensemble mean in the frequency domain (k_1, k_2),

$$\begin{aligned} E &= \int_{-\infty}^{\infty}\int_{-\infty}^{\infty} \mathrm{E}[dZ_w(k_1,k_2)dZ_q^*(k_1,k_2)] \\ &= \int_{-\infty}^{\infty}\int_{-\infty}^{\infty} \Pi_w(k_1,k_2)\Pi_q^*(k_1,k_2)\sigma_h^2 S_h(k_1,k_2)dk_1dk_2. \end{aligned} \tag{5.85}$$

The moisture flux E can be further expressed using the analytical solution (5.46) and (5.73) as,

$$\begin{aligned} E &= -\sigma_h^2[\int_{-\infty}^{\infty}\int_{-\infty}^{\infty} ik_1 u_0 \mathrm{e}^{-2zk|\mathrm{Re}(\hat{T})|} S_h(k_1,k_2)dk_1dk_2]\frac{d\bar{q}(z)}{dz} \\ &= 0 \end{aligned} \tag{5.86}$$

This linear theory predicts that the mountain waves do not make a contribution to the vertical transport of moisture when averaged over the entire mesoscale domain. In other words, vertical transport of moisture by topography induced flow if any is a nonlinear behavior of the mesoscale system.

5.7 Effect of Large Scale Wind

Since large scale flow provides kinetic energy to the mesoscale system, it is of interest to examine the behavior of mountain waves as a function of large scale wind u_0.

Figure 5-6 shows how standard deviations of the topography induced wind components σ_u, σ_u, σ_u and the assocaited momentum fluxes M_x, M_y and heat flux H vary with the large scale wind u_0. The curves shown in Figure 5-6 are computed at the surface (z=0). The dependence of these quantities on height z have already been illustrated in Figure 5-3, Figure 5-4, and Figure 5-5.

All of these six statistics shown in Figure 5-6 increase slowly as u_0 increases from zero. After a moderate value of $u_0 \sim 5$ m s^{-1}, σ_u, σ_u, σ_u and M_y increase linearly with large scale wind u_0. H stabilizes at this moderate value of u_0. M_x oscillates and decays with u_0 from ~ 5 m s^{-1} up to ~ 90 m s^{-1}, and eventually goes to zero as u_0 becomes very large. So in the linear framework, the role of topography is to transfer the kinetic energy from the large scale flow into the mesoscale system and transport it upward within the mesoscale system. As the large scale wind u_0 becomes stronger, vertical transport of momentum by the topography induced flow in the direction of u_0 will be suppressed. At the same time the energy is transfered upward by the wind component perpendicular to u_0. Although the kinetic energy of the mountain waves increases with u_0, the transport of heat by the

mountain waves remains insignificant.

Discussion Transport of kinetic energy from the large scale flow to the mesoscale system implies a resistant force caused by the topography induced flow. There should be a negative feedback between the large scale flow and the mesoscale flow interacting through the topography. Increases in the mesoscale flow result in a stronger resistance to the large scale flow, hence tends to reduce the large scale wind that forces the mesoscale flow induced by the topography.

5.8 Summary

This chapter develops a stochastic linear theory of mountain waves in a non-hydrostatic, rotating, and dissipative atmosphere induced by airflow over a three-dimensional complex topography covering the entire domain of interest. The governing flow equations are formulated as a set of linear stochastic partial differential equations (SPDE's) with random boundary condition at the surface. The transient and the steady-state ensemble solutions of the SPDEs, which link the statistics of mountain waves to that of a complex topography through physical principles, have been derived analytically. The domain-averaged vertical transport of momentum and of heat are computed as explicit functions of background wind, stability, dissipation coefficient of the atmosphere, and the parameters characterizing topography. The results may lead to several conclusions:

- The fundamental feature of the length scale properties of mountain waves induced by complex 3D topography is determined by the statistical property of the line topographic height parallel to the background flow. This result justifies the qualitative behavior of mountain waves predicted by 2D linear theories. Quantitatively, this stochastic linear theory has shown that the mesoscale variability of topography makes a major contribution to the generation of mountain waves and the resultant vertical transport of energy, as found in previous studies.

- This stochastic linear theory demonstrates that the dissipation process plays an important role in determining the spatial-temporal distribution of mountain waves. The presence of dissipation guarantees the existence of a steady-state solution if the atmosphere starts from rest. The established solutions for non-dissipative atmosphere can be retrieved as a limiting case of the general solution of the dissipative atmospheric flow derived herein. We found that dissipation is responsible for the gradient of vertical momentum fluxes and the downward heat flux.

- The momentum fluxes associated with the mountain waves could be more important than the turbulent flux within the depth of the boundary layer. The vertical transport of horizontal momentum in the direction parallel to background flow is more important than that from the perpendicular direction (due to the Coriolis force) for typical value of large scale wind. The large scale flow provides the kinetic energy to the mountain waves.

- The presence of variable topography transfers kinetic energy from the large scale flow to the mesoscale flow. Consequently, topography produces a resistance to the large scale flow. Hence its effects should be taken into account in large scale atmospheric models.

- The heat flux associated with the mountain waves in a typical atmospheric environment is at least one order of magnitude smaller than the turbulent heat flux in the boundary layer. Therefore, wave induced heat flux is in general not important.

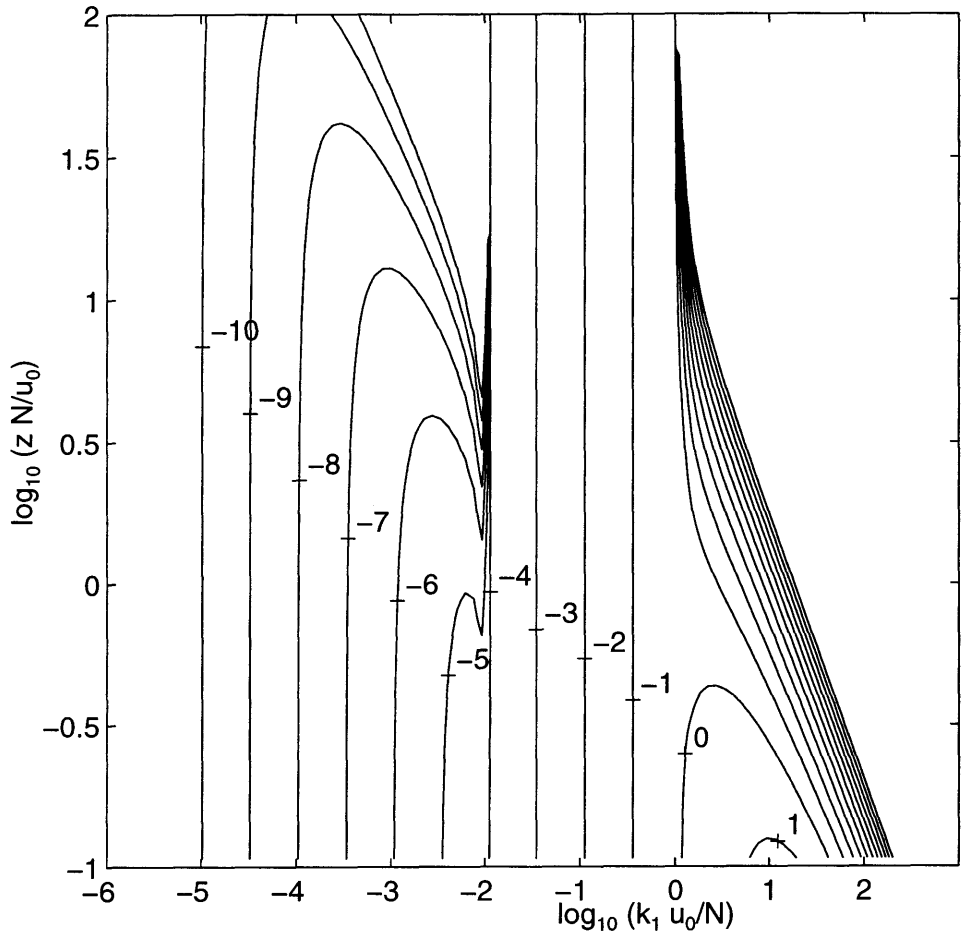

Figure 5-1: $\log_{10} \mid \Pi_w \mid^2$ as a function of normalized wave number k_1 and height z (by u_0/N) for non-dissipative atmosphere ($\alpha = 0$).

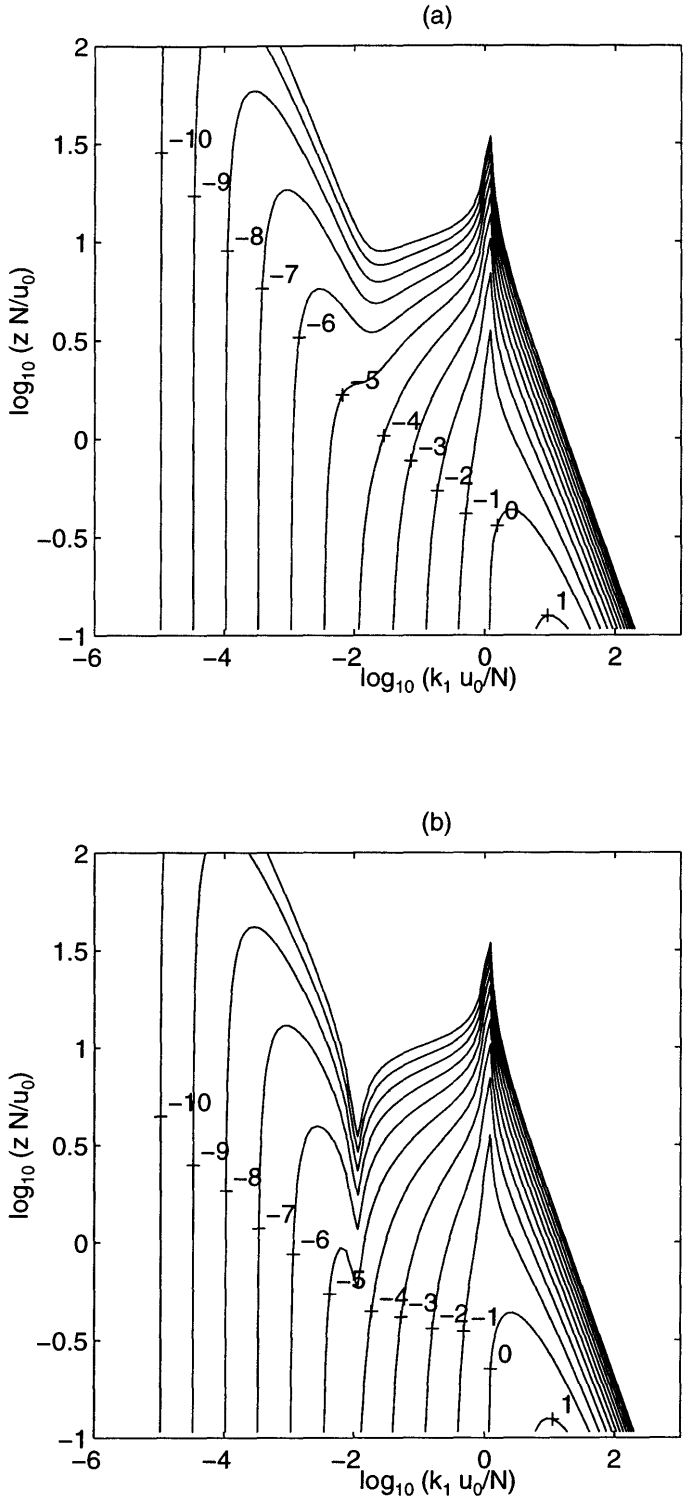

Figure 5-2: $\log_{10} \mid \Pi_w \mid^2$ as a function of normalized k_1 and z (by u_0/N) for dissipative atmosphere. (a) $\alpha = 10^{-4}$ s^{-1}, and (b) $\alpha = 10^{-5}$ s^{-1}.

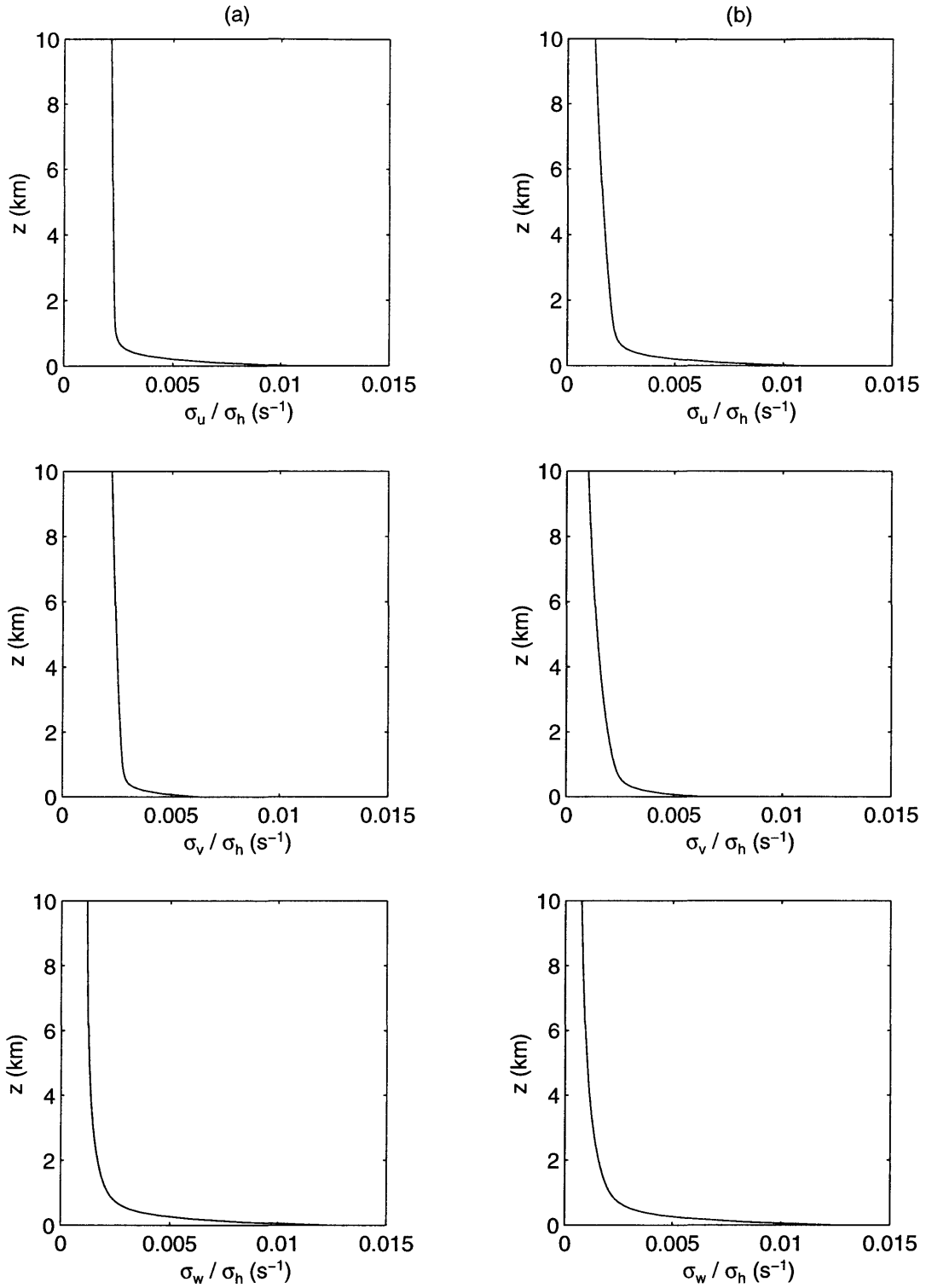

Figure 5-3: Vertical distribution of the standard deviations of wind components, σ_u, σ_v, and σ_w (m s^{-1}), normalized by the standard deviation of topographic height σ_h when $u_0 = 10$ m s^{-1}. (a) $\alpha = 10^{-5}$ s^{-1}, (b) $\alpha = 10^{-4}$ s^{-1}.

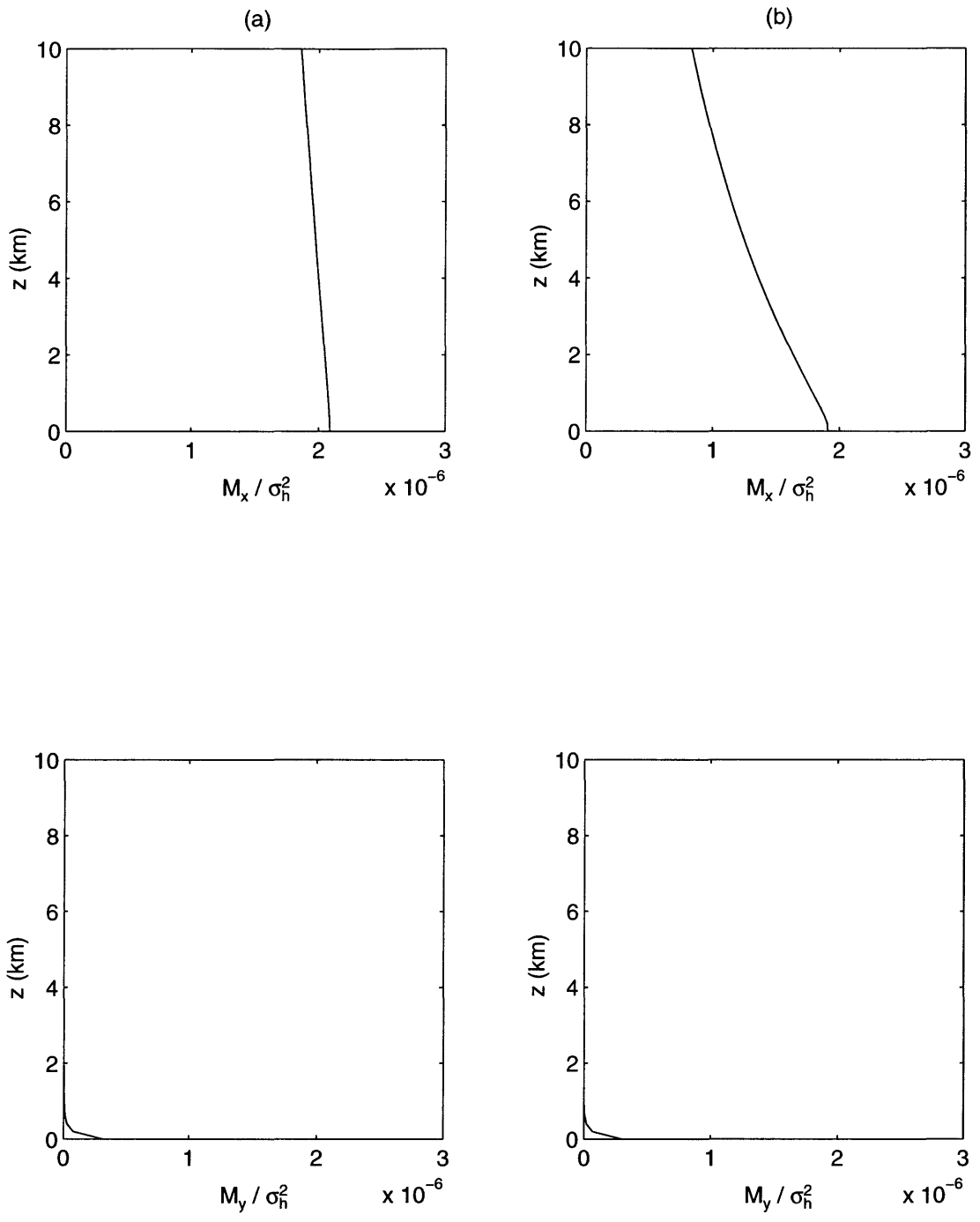

Figure 5-4: Vertical distribution of momentum fluxes, M_x and M_y (m^2 s^{-2}), normalized by the variance of topographic height σ_h^2 when $u_0 = 10$ m s^{-1}. (a) $\alpha = 10^{-5}$ s^{-1}, (b) $\alpha = 10^{-4}$ s^{-1}.

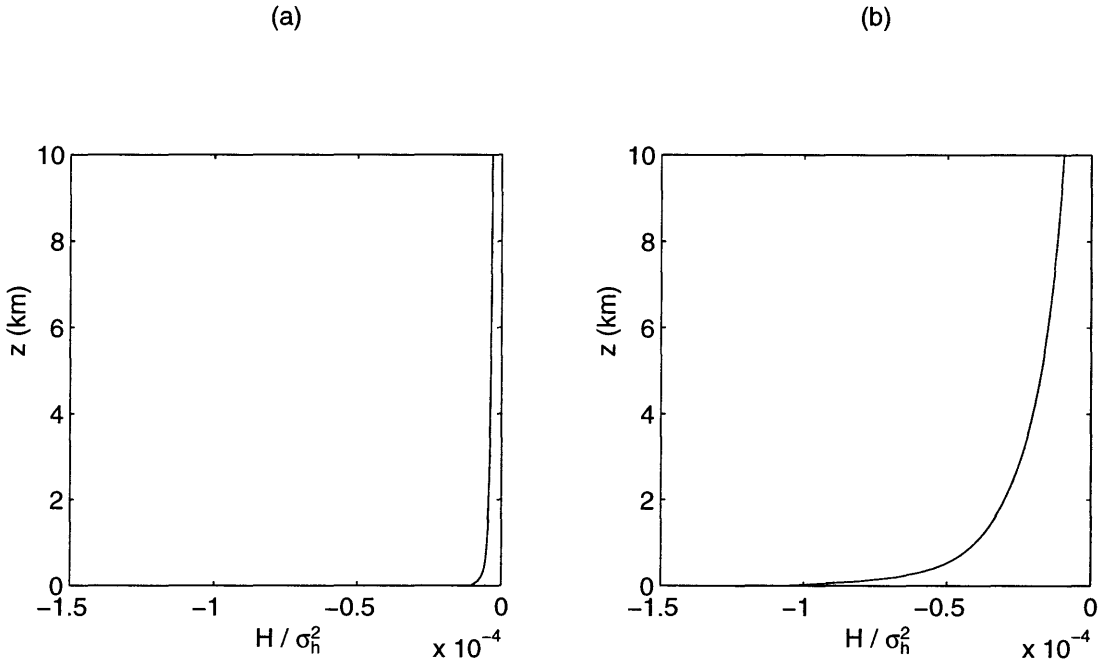

Figure 5-5: Impact of the dissipation α on the vertical distribution of heat flux, H (W m^{-2}), normalized by the variance of topographic height σ_h^2 when $u_0 = 10$ m s^{-1}. (a) $\alpha = 10^{-5}$ s^{-1}, (b) $\alpha = 10^{-4}$ s^{-1}.

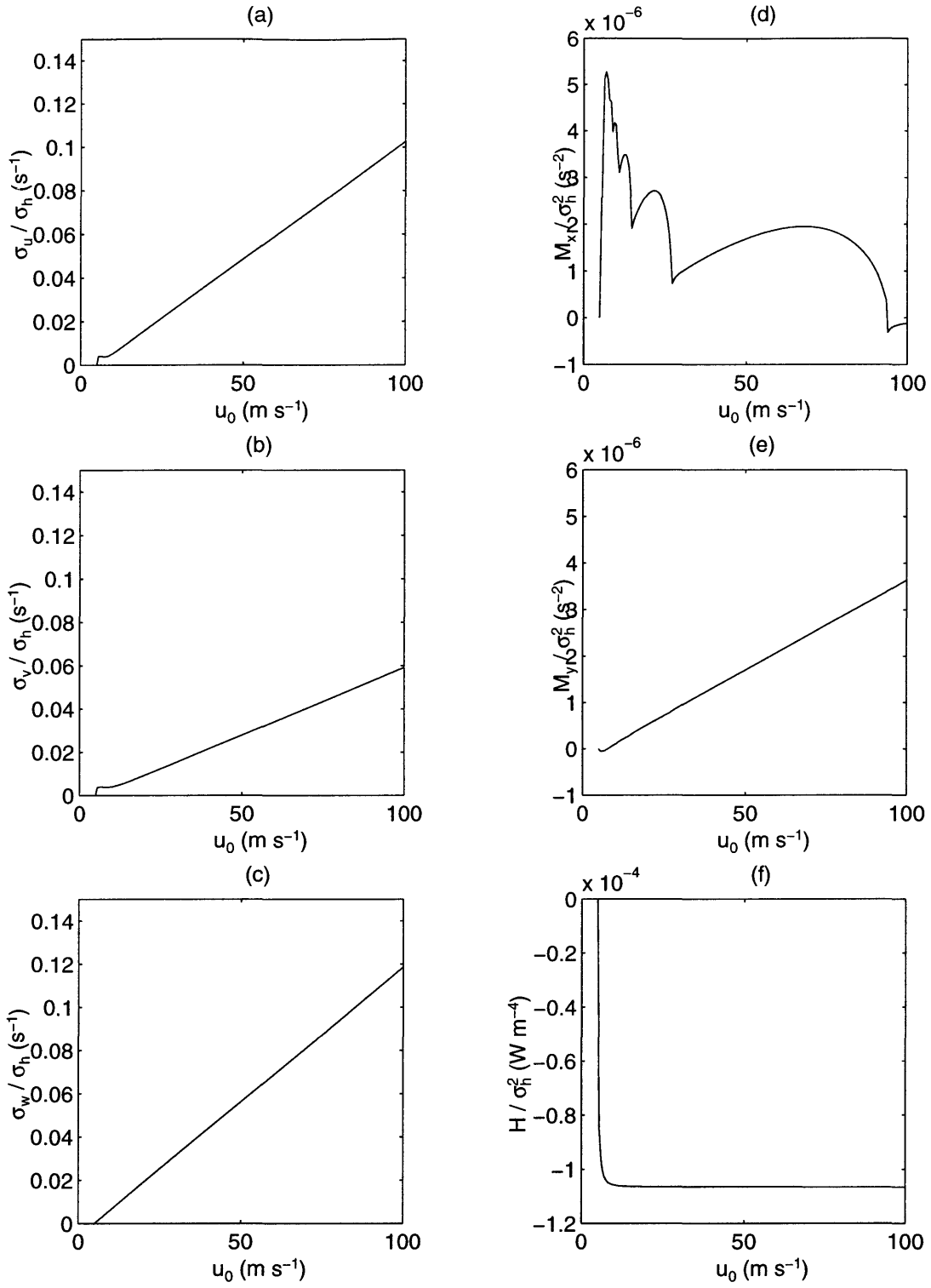

Figure 5-6: Standard deviations of wind components, σ_u, σ_v, and σ_w (m s^{-1}), normalized by the standard deviation of topographic height σ_h (m); momentum fluxes M_x, M_y, and heat flux H, normalized by the variance of topographic height σ_h^2 (m^2) as the functions of large scale u_0 when $\alpha = 10^{-4}$ s^{-1} at the surface.

Chapter 6

Conclusions and Future Research

6.1 Conclusions

Recent studies of the mesoscale circulation induced by land surface heterogeneity have indicated that the vertical transport of mass and energy associated with this type of mesoscale flow could be as important as the turbulent fluxes, hence needs to be included in the subgrid parameterization schemes of large scale atmospheric models. To further assess the importance of mesoscale circulation and mesoscale fluxes under realistic surface forcings, stochastic linear models have been developed to identify the relative importance of the parameters characterizing the surface forcing and synoptic environment. Nonlinear simulations were also carried out to evaluate the performance of the linear theory for the thermally induced mesoscale flow. The assumed statistics characterizing the complex thermal and topographical surface forcings used in the linear theories and the numerical simulations are consistent with those estimated from observations. This is a significant improvement relative to the previously assumed over-simplified land surface heterogeneities in both differential heating and topography.

The obtained analytical ensemble solutions based on the linear mesoscale models directly link spatial-temporal distributions of velocities, pressure and temperature to that of the complex, random, land surface. Analysis of the mesoscale circulation is facilitated by the analytical solutions derived from the linear theories. These analytical solutions are par-

ticularly useful in studying the length scale properties of the mesoscale circulation. The computation of mesoscale fluxes, which are defined in a way similar to the eddy correlation for turbulent fluxes, is obtained by integrating over frequency domain using the ensemble solutions.

The numerical simulations have demonstrated the role of nonlinear advective terms in the surface heating induced mesoscale circulation. These nonlinear terms prove to be important factors in determining the magnitude of the thermally induced flow and the associated fluxes.

The major conclusions drawn from the discussions in the previous chapters are summarized as follows.

1. Thermal heterogeneity of land surface due to variable vegetation cover characterized by **NDVI** has length scale on the order of $10^1 - 10^2$ kilometers. The standard deviation of the corresponding sensible heat flux is on the order of a few tens W m^{-2}. The complex topography over mesoscale regions has a power-law spectrum with exponent ranging from -1 to -5/2. The standard deviation of topography over a mesoscale domain will be on the order of $\sim 10^2$ meters. This land surface heterogeneity could generate significant mesoscale circulation and mesoscale fluxes.

2. Standard deviation and (appropriately defined) length scale are two important parameters that satisfactorily characterize the spectrum of the heterogeneity of land surface. While the functional form of the corresponding spectrum is not critical for the distribution of mesoscale circulation and fluxes.

3. Surface (thermal and topographical) forcing of small length scales has important impact only on the mesoscale atmosphere at lower levels, while surface forcing of relatively large length scale affect the atmosphere at higher levels. The whole body of the atmosphere from the bottom to the top filters out high wave-number components of the disturbances resulting from land surface heterogeneity.

4. The linear analysis predicts that stable stratification and moderate synoptic wind strongly inhibit the development of mesoscale circulation and mesoscale fluxes of momentum, heat and moisture under surface heating of random distribution. The stable

stratification provides a strong resistant force against buoyancy due to the heating forcing from heterogenous land surface so that dry convection can not reach a significant level. Development of dry convection is also vulnerable to synoptic wind that tends to wipe off locally induced circulation cells.

5. Nonlinear numerical simulations suggest that, under the same surface thermal forcing as used in linear analysis, momentum fluxes are at least one order of magnitude greater than (comparable to) turbulent flux in a neutral (stable) atmosphere, and insensitive to the synoptic wind. This result is believed to be mainly due to the momentum transport mechanism provided by the nonlinear advection.

6. Thermally induced mesoscale heat flux has differential vertical distribution from turbulent heat flux. The maximum value of mesoscale heat flux may be one order of magnitude smaller that the turbulent flux at the surface predicted by the nonlinear numerical analysis. It, however, could be the dominant heat transport component at those levels where turbulent heat flux is insignificant. Linear model predicts a much larger mesoscale heat flux which could be of the same order of magnitude as its turbulent counterpart mainly due to the stronger flow.

7. The linear analysis for the topographically induced flow predicts that the fundamental features of 3D mountain waves are determined by the statistical properties of the topographic height in the direction parallel to the uniform synoptic wind. This quasi-two-dimensional behavior is rooted from the topographical forcing determined only by the variable slope of the surface profile that enters the mesoscale system through the boundary condition. The variable topography with length scales on the order of $10^1 \sim 10^2$ km makes a major contribution to the generation of mountain waves and the resultant vertical transport of energy.

8. Topographical barriers effectively transfer kinetic energy from the large scale flow to the mesoscale flow. Consequently, the topographically induced mesoscale momentum flux is more important than turbulent at lower levels under typical atmospheric conditions. The vertical transport of horizontal momentum in the direction parallel to the synoptic

wind is at least one order of magnitude greater than that from the perpendicular direction. On the other hand, mesoscale heat flux (downward if any) is insignificant (about two order of magnitude smaller than typical value of turbulent sensible heat flux at land surface) considering that there is no sensible heat flux into the mesoscale system.

The findings from this study could provide new insight into the physical basis for the use of Rayleigh friction in large scale modeling (e.g. Gill 1980 and Neelin 1988) to represent dissipation. The results of this study suggest that mesoscale circulation gives rise to a mechanical resistance which tends to reduce the large scale flow. The presence of land surface heterogeneity acts to transport the kinetic energy from large scale systems down to the mesoscale systems, which could be regarded as a momentum sink of the large scale system. Therefore, the land surface heterogeneity induced mesoscale circulation could be an important dissipation process that should be taken into account in the large scale flow.

The proposed analytical framework provides a new and powerful methodology for analyzing land surface heterogeneities of complex distribution induced mesoscale circulations. Particularly, the analysis of the length scale properties of mesoscale circulations is facilitated by examining the corresponding frequency response functions derived from the stochastic linear theories. The wave numbers at which the frequency response functions reach maxima correspond to the length scales of the surface forcing that is most effective in inducing atmospheric flow. This explicit relation between the length scales of the forcing and that of the flow is otherwise difficult to obtain.

Linear analysis also elucidate the relative importance of the different elements of mesoscale system and synoptic environment to the mesoscale circulation when comparing with nonlinear numerical model. For example, atmospheric stability has been identified as the most important factor of the synoptic environment that affects the distribution of mesoscale circulation. Nonlinear advective terms are believed to be the primary momentum transport mechanism. This conclusion justifies the need to develop an analytical nonlinear framework to further study the impact of nonlinearity on the mesoscale circulation induced by the land surface heterogeneity.

Besides the above arguments about the differences in the results of the mesoscale circulation from the linear and nonlinear analysis, space resolution of the numerical model could be a factor that needs to be considered. Discretization in numerical models will loss fine flow structures below the grid size, which may have significant contribution to the flow intensity and the associated fluxes. This unavoidable step, however, is not expected to be of major concern in the validity of the results based on the numerical simulation. First, the grid size is selected such that the land surface heterogeneity is sufficiently resolved. Second, there is observational evidence (Atkinson 1981) indicating a relatively wide spectral "gap" between micro- and meso-scale. Therefore, reducing the grid size beyond certain point is unlikely to provide much more information about the mesoscale circulation induced by the land surface heterogeneity.

The results of this study will be potentially useful in designing new generation of subgrid parameterization schemes to improve the performance of current large scale atmospheric models. The analytical solutions of the linear theory help to visualize the basic features of the spatial-temporal distributions of mesoscale circulations and fluxes. The nonlinear numerical simulations provide guidance for making possible correction to the linear approximation. The resolved processes in the large scale models provide the information about the background flow and stratification for the unresolved subgrid processes driven by the surface forcings. The thermal and topographical forcings resulting from heterogeneous land surface are characterized by the standard deviations and length scales of the TSHF and topography. Then the additional contribution to the total transport of energy by subgrid processes due to the land surface heterogeneity can be estimated using the results obtained in this study, and incorporated into the parameterization schemes.

6.2 Future Research

Several issues related to what have been completed in this thesis deserve further exploration, including nonlinear effects on the behavior of mountain waves over complex terrain; impacts of land surface variability such as caused by deforestation on the distribution of convective

rainfalls, and impacts of nonlinearity on the length scale properties of atmospheric system. Continuation of this work should be along three directions.

6.2.1 Numerical Simulation of Topographically Induced Flow

The relative importance of the nonlinear terms needs to be assessed using a nonlinear numerical model considering there is no analytical tool available for this purpose. Nonlinear advective terms are expected to play a significant role in the development of mountain waves over complex terrain. It has been known that the problems such as stagnation point due to flow splitting (e.g. Smith 1989) and flow over large hills require considering the effect of nonlinear terms in the modeling. Besides, investigating the influence of variable wind profile also needs numerical models. A realization of random topography will be generated according to prescribed spectrum estimated from topographical data such as digital elevation map (DEM), and used as an input to a numerical model.

6.2.2 Distribution of Convective Rainfall

The spatial distribution of tropical rainfall over a mesoscale domain is an important issue in hydrological and climatic research. For example, Lüthi et al (1996) found that summertime precipitation totals predicted by a regional climate model were not simulated satisfactorily. They believe this phenomenon due to the fact that the summertime precipitation is more substantially affected by small-scale moist convection and surface hydrological processes. Hence it will be useful to to investigate the influence of randomly variable land surface due to soil moisture or vegetation cover on the convective rainfall.

In the tropical region of Amazon basin, deforestation due to human activities has induced significant land surface heterogeneity compared to the intact areas. Observational studies (e.g. Cutrim *et la* 1995) have shown the enhancement of cumulus clouds over deforested lands in part of Amazon basin. It would be interesting to study the relation between the distribution of the moist convection and the land surface heterogeneity caused by deforestation.

6.2.3 Nonlinear Theory

The nonlinear numerical model has suggested that the nonlinear advective terms play an important role in the land surface heterogeneity induced mesoscale circulation and mesoscale fluxes. It will be very useful to develop a nonlinear theory to further explore quantitatively the impact of nonlinear advective terms. One possible methodology for developing a nonlinear stochastic model is the so-called Wiener-Hermite expansion of non-linear random processes (Schetzen 1980).

The W-H expansion approach is able to deal with random functions with non-Gaussian distribution, an essential property of nonlinear processes. The basic idea of Wiener-Hermite expansion is to express a random process as a hierarchy of Wiener orthorgonal functionals. The kernel functions in these orthogonal functionals will be determined by the governing equations of the flow system. There are many successful application of this approach in a variety of fields in science and engineering, particularly in turbulent flow. It is worthwhile to devote efforts on this promising approach and its applications in hydrometerological research. This approach is potentially useful in many other topics such as boundary layer meteorology, groundwater flow modeling, pollutant transport in random porous media, etc.

Appendix A

List of Symbols

b	buoyancy
C_P	specific heat capacity of the air at constant pressure
E_m	mesoscale moisture flux
f	Coriolis parameter ($=2\Omega \sin \varphi$)
H_m	mesoscale sensible heat flux
H_t	turbulent sensible heat flux
h	vertical scale of diabatic heating (taken to be 1km in this paper)
i	pure imaginary number $\sqrt{-1}$
k	radius wave number $(k_1^2 + k_2^2)^{1/2}$
k_1, k_2	wave number in x and y direction
L	length scale
M_m^x, M_m^y	mesoscale momentum fluxes associated with u and v
N	constant Brunt-Väisälä frequency
q	water content of the air
Q	buoyancy source due to diabatic heating
r	radius distance $(x^2 + y^2)^{1/2}$
$S(k_1, k_2)$	spectral density function
t	time

T_0	length of a day (24 hrs)
u, v, w	wind velocity in x, y, and z direction
u_0	constant synoptic wind in x direction
x, y	horizontal coordinates
z	vertical coordinate (z is normalized by h in all figures.)
α	inverse of linear damping time scale
θ	potential temperature
ρ	density of air
σ^2	variance
ϕ	geopotential
φ	latitude
Ω	rotation rate of the earth ($=2\pi/T_0$)
E[ ]	ensemble average (mathematical expectation)
$\bar{()}$	horizontal domain average
$()^*$	complex conjugate

Appendix B

Approach to the Analytical Solution of Thermally Induced Flow

Denote the Laplace operator by $\mathcal{L}_{t,s}$ where t is the independent variable that the Laplace transform refers to, $\mathcal{L}_{t,s}\{f(t)\} \equiv F(s)$. Then we may express

$$\begin{aligned}
\mathcal{L}_{t,s}\{dZ_u(k_1,k_2;z,t)\} &= \tilde{U}(k_1,k_2;z,s) \\
\mathcal{L}_{t,s}\{dZ_v(k_1,k_2;z,t)\} &= \tilde{V}(k_1,k_2;z,s) \\
\mathcal{L}_{t,s}\{dZ_w(k_1,k_2;z,t)\} &= \tilde{W}(k_1,k_2;z,s) \\
\mathcal{L}_{t,s}\{dZ_b(k_1,k_2;z,t)\} &= \tilde{B}(k_1,k_2;z,s) \\
\mathcal{L}_{t,s}\{dZ_\phi(k_1,k_2;z,t)\} &= \tilde{\Phi}(k_1,k_2;z,s)
\end{aligned}$$

, and

$$\begin{aligned}
\mathcal{L}_{z,p}\{\tilde{U}(k_1,k_2;z,s)\} &= U(k_1,k_2;p,s) \\
\mathcal{L}_{z,p}\{\tilde{V}(k_1,k_2;z,s)\} &= V(k_1,k_2;p,s) \\
\mathcal{L}_{z,p}\{\tilde{W}(k_1,k_2;z,s)\} &= W(k_1,k_2;p,s) \\
\mathcal{L}_{z,p}\{\tilde{B}(k_1,k_2;z,s)\} &= B(k_1,k_2;p,s) \\
\mathcal{L}_{z,p}\{\tilde{\Phi}(k_1,k_2;z,s)\} &= \Phi(k_1,k_2;p,s)
\end{aligned}$$

Laplace transforms of Eqs. (3.33) through (3.37) with respect to t lead to

$$
\begin{aligned}
(s+\alpha+ik_1u_0)\tilde{U} - f\tilde{V} &= -ik_1\tilde{\Phi} && \text{(B.1)}\\
(s+\alpha+ik_1u_0)\tilde{V} + f\tilde{U} &= -ik_2\tilde{\Phi} && \text{(B.2)}\\
(s+\alpha+ik_1u_0)\tilde{W} - \tilde{B} &= -\frac{\partial\tilde{\Phi}}{\partial z} && \text{(B.3)}\\
(s+\alpha+ik_1u_0)\tilde{B} + N^2\tilde{W} &= \tilde{I}(s)\exp(-\frac{z}{h})dZ_Q && \text{(B.4)}\\
ik_1\tilde{U} + ik_2\tilde{V} + \frac{\partial\tilde{W}}{\partial z} &= 0 && \text{(B.5)}
\end{aligned}
$$

where, according to (3.19)

$$
\begin{aligned}
\tilde{I}(s) &= \mathcal{L}_{t,s}\{I(t)\}\\
&= \frac{1}{1-\exp(-\pi s/\Omega)}\frac{\Omega}{s^2+\Omega^2} && \text{(B.6)}
\end{aligned}
$$

Laplace transforms of Eqs. (B.1) through (B.5) with respect to z result in

$$
\begin{aligned}
(s+\alpha+ik_1u_0)U - fV &= -ik_1\Phi && \text{(B.7)}\\
(s+\alpha+ik_1u_0)V + fU &= -ik_2\Phi && \text{(B.8)}\\
(s+\alpha+ik_1u_0)W - B &= -p\Phi + \tilde{\Phi}(0,s) && \text{(B.9)}\\
(s+\alpha+ik_1u_0)B + N^2W &= \tilde{I}(s)\frac{1}{p+1/h}dZ_Q && \text{(B.10)}\\
ik_1U + ik_2V + pW &= \tilde{W}(0,s) && \text{(B.11)}
\end{aligned}
$$

where the boundary conditions $\tilde{W}(0,s)$ and $\tilde{\Phi}(0,s)$ are determined such that all the perturbation terms vanish as the vertical coordinate z goes to infinity, and vertical velocity w is zero at the ground.

$$
\begin{aligned}
\lim_{z\to\infty} u', v', w', b', \phi' &= 0 && \text{(B.12)}\\
w'\,|_{z=0} &= 0 && \text{(B.13)}
\end{aligned}
$$

Performing Laplace transform twice converts the original partial differential Eqs. (3.33) through (3.37) into a set of linear algebraic Eqs. (B.7) - (B.11).

The solution of Eqs. (B.7) through (B.11) is shown as follows

$$U = \frac{-i[k_1(s+\alpha+ik_1u_0)+fk_2]}{(s+\alpha+ik_1u_0)^2+f^2}\Phi \tag{B.14}$$

$$V = \frac{-i[k_2(s+\alpha+ik_1u_0)-fk_1]}{(s+\alpha+ik_1u_0)^2+f^2}\Phi \tag{B.15}$$

$$\begin{aligned} W = & \{\frac{-\tilde{I}(s)}{[(s+\alpha+ik_1u_0)^2+f^2]}\frac{k^2}{(p+1/h)(p^2-k^2T^2)}\}dZ_Q + \\ & \frac{1}{p^2-k^2T^2}\{p\tilde{W}(0,s)-\frac{(s+\alpha+ik_1u_0)k^2}{(s+\alpha+ik_1u_0)^2+f^2}\tilde{\Phi}(0,s)\} \end{aligned} \tag{B.16}$$

$$\begin{aligned} B = & \{\frac{\tilde{I}(s)}{(s+\alpha+ik_1u_0)}\frac{1}{(p+1/h)}[1+\frac{k^2\frac{N^2}{(s+\alpha+ik_1u_0)^2+f^2}}{p^2-k^2T^2}]\}dZ_Q + \\ & \frac{1}{p^2-k^2T^2}\{\frac{k^2N^2}{(s+\alpha+ik_1u_0)^2+f^2}\tilde{\Phi}(0,s)-\frac{N^2}{s+\alpha+ik_1u_0}p\tilde{W}(0,s)\} \end{aligned} \tag{B.17}$$

$$\begin{aligned} \Phi = & \{\frac{\tilde{I}(s)}{(s+\alpha+ik_1u_0)}\frac{p}{(p+1/h)(p^2-k^2T^2)}\}dZ_Q + \\ & \frac{1}{p^2-k^2T^2}\{p\tilde{\Phi}(0,s)-\frac{(s+\alpha+ik_1u_0)^2+N^2}{s+\alpha+ik_1u_0}\tilde{W}(0,s)\} \end{aligned} \tag{B.18}$$

where

$$T = T(s) = [\frac{(s+\alpha+ik_1u_0)^2+N^2}{(s+\alpha+ik_1u_0)^2+f^2}]^{\frac{1}{2}} \tag{B.19}$$

Next we use the inverse Laplace transform twice, $\mathcal{L}_{p,z}^{-1}$ and $\mathcal{L}_{s,t}^{-1}$, on (B.14) - (B.18) to solve for dZ's

$$\begin{aligned} dZ_u(k_1,k_2;z,t) &= \mathcal{L}_{s,t}^{-1}\{\mathcal{L}_{p,z}^{-1}\{U\}\} \\ dZ_v(k_1,k_2;z,t) &= \mathcal{L}_{s,t}^{-1}\{\mathcal{L}_{p,z}^{-1}\{V\}\} \\ dZ_w(k_1,k_2;z,t) &= \mathcal{L}_{s,t}^{-1}\{\mathcal{L}_{p,z}^{-1}\{W\}\} \\ dZ_b(k_1,k_2;z,t) &= \mathcal{L}_{s,t}^{-1}\{\mathcal{L}_{p,z}^{-1}\{B\}\} \end{aligned}$$

$$dZ_\phi(k_1, k_2; z, t) = \mathcal{L}_{s,t}^{-1}\{\mathcal{L}_{p,z}^{-1}\{\Phi\}\}$$

The inverse Laplace transform $\mathcal{L}_{p,z}^{-1}$ on Eq. (B.14) through (B.18) leads to

$$\begin{aligned}
\tilde{U} &= \mathcal{L}_{p,z}^{-1}\{U\} \\
&= \frac{-i[k_1(s+\alpha+ik_1u_0)+fk_2]}{(s+\alpha+ik_1u_0)^2+f^2}\tilde{\Phi}
\end{aligned} \tag{B.20}$$

$$\begin{aligned}
\tilde{V} &= \mathcal{L}_{p,z}^{-1}\{V\} \\
&= \frac{-i[k_2(s+\alpha+ik_1u_0)-fk_1]}{(s+\alpha+ik_1u_0)^2+f^2}\tilde{\Phi}
\end{aligned} \tag{B.21}$$

$$\begin{aligned}
\tilde{W} &= \mathcal{L}_{p,z}^{-1}\{W\} \\
&= \frac{-k^2h^2}{(1-k^2h^2)}\frac{\tilde{I}(s)}{[(s+\alpha+ik_1u_0)^2+\Lambda^2]} \\
&\quad \{\exp(-\frac{z}{h}) - \cosh(zkT) + \frac{1}{hkT}\sinh(zkT)\}dZ_Q + \\
&\quad \cosh(kzT)\tilde{W}(0,s) - \frac{s+\alpha+ik_1u_0}{(s+\alpha+ik_1u_0)^2+f^2}\frac{k}{T}\sinh(kzT)\tilde{\Phi}(0,s)
\end{aligned} \tag{B.22}$$

$$\begin{aligned}
\tilde{B} &= \mathcal{L}_{p,z}^{-1}\{B\} \\
&= \frac{\tilde{I}(s)}{(s+\alpha+ik_1u_0)}\{\exp(-\frac{z}{h}) + \frac{k^2h^2}{1-k^2h^2}\frac{N^2}{[(s+\alpha+ik_1u_0)^2+\Lambda^2]} \\
&\quad [\exp(-\frac{z}{h}) - \cosh(zkT) + \frac{1}{hkT}\sinh(zkT)]\}dZ_Q \\
&\quad + \frac{k^2N^2}{(s+\alpha+ik_1u_0)^2+f^2}\frac{1}{kT}\sinh(kzT)\tilde{\Phi}(0,s) \\
&\quad - \frac{N^2}{s+\alpha+ik_1u_0}\cosh(kzT)\tilde{W}(0,s)
\end{aligned} \tag{B.23}$$

$$\begin{aligned}
\tilde{\Phi} &= \mathcal{L}_{p,z}^{-1}\{\Phi\} \\
&= \frac{-h}{(1-k^2h^2)}\frac{\tilde{I}(s)}{(s+\alpha+ik_1u_0)}\frac{(s+\alpha+ik_1u_0)^2+f^2}{(s+\alpha+ik_1u_0)^2+\Lambda^2} \\
&\quad \{\exp(-\frac{z}{h}) - \cosh(zkT) + hkT\sinh(zkT)\}dZ_Q +
\end{aligned}$$

$$\cosh(kzT)\tilde{\Phi}(0,s) - \frac{(s+\alpha+ik_1u_0)^2+N^2}{s+\alpha+ik_1u_0}\frac{1}{kT}\sinh(kzT)\tilde{W}(0,s) \qquad \text{(B.24)}$$

where

$$\Lambda^2 = \frac{f^2-k^2h^2N^2}{1-k^2h^2} \qquad \text{(B.25)}$$

The boundary conditions (B.12) and (B.13) require

$$\tilde{W}(0,s) = 0 \qquad \text{(B.26)}$$

$$\tilde{\Phi}(0,s) = \frac{h}{(1-k^2h^2)}\frac{\tilde{I}(s)}{(s+\alpha+ik_1u_0)}\frac{(s+\alpha+ik_1u_0)^2+f^2}{(s+\alpha+ik_1u_0)^2+\Lambda^2}(khT-1)dZ_Q \qquad \text{(B.27)}$$

Thus, the solution of Eqs. (B.20) through (B.24) subject to the boundary conditions (B.26) and (B.27) is

$$\tilde{U} = \frac{-i[k_1(s+\alpha+ik_1u_0)+fk_2]}{(s+\alpha+ik_1u_0)^2+f^2}\tilde{\Phi} \qquad \text{(B.28)}$$

$$\tilde{V} = \frac{-i[k_2(s+\alpha+ik_1u_0)-fk_1]}{(s+\alpha+ik_1u_0)^2+f^2}\tilde{\Phi} \qquad \text{(B.29)}$$

$$\tilde{W} = \frac{-k^2h^2}{(1-k^2h^2)}\frac{\tilde{I}(s)}{[(s+\alpha+ik_1u_0)^2+\Lambda^2]}\{\exp(-\frac{z}{h})-\exp(-zkT)\}dZ_Q \qquad \text{(B.30)}$$

$$\tilde{B} = \frac{\tilde{I}(s)}{(s+\alpha+ik_1u_0)}\{\exp(-\frac{z}{h})+\frac{k^2h^2}{1-k^2h^2}\frac{N^2}{[(s+\alpha+ik_1u_0)^2+\Lambda^2]} [\exp(-\frac{z}{h})-\exp(-zkT)]\}dZ_Q \qquad \text{(B.31)}$$

$$\tilde{\Phi} = \frac{-h}{(1-k^2h^2)}\frac{\tilde{I}(s)}{(s+\alpha+ik_1u_0)}\frac{(s+\alpha+ik_1u_0)^2+f^2}{(s+\alpha+ik_1u_0)^2+\Lambda^2} \{\exp(-\frac{z}{h})-khT\exp(-zkT)\}dZ_Q \qquad \text{(B.32)}$$

Using the inverse Laplace transform $\mathcal{L}_{s,t}^{-1}$ on (B.28) - (B.32) results in the functional forms of dZ's shown in section 3.3.3.

Appendix C

Derivation of Eq. (3.63)

We may rewrite Eq.(3.60) using Eq.(3.15) as

$$\frac{\partial q}{\partial t} + u\frac{\partial q}{\partial x} + v\frac{\partial q}{\partial y} + w\frac{\partial q}{\partial z} = 0 \tag{C.1}$$

Linearly superimposing the synoptic wind u_0 on the thermally induced mesoscale flow component u, and substituting Eqs. (3.20) - (3.22) and (3.61) into Eq. (C.1), we have

$$\frac{\partial \bar{q}}{\partial t} + \frac{\partial q'}{\partial t} + u_0\frac{\partial q'}{\partial x} + u'\frac{\partial q'}{\partial x} + v'\frac{\partial q'}{\partial y} + w'\frac{\partial \bar{q}}{\partial z} + w'\frac{\partial q'}{\partial z} = 0 \tag{C.2}$$

where we have used the conditions $\bar{u} = 0$, $\bar{v} = 0$ and $\bar{w} = 0$.

Assuming the domain-average moisture profile $\bar{q}$ to be independent of time, implying $\bar{q} = \bar{q}(z)$, and dropping the cross-products of the perturbation terms in Eq. (C.2) lead to the linearized equation for q',

$$\frac{\partial q'}{\partial t} + u_0\frac{\partial q'}{\partial x} + w'\frac{\partial \bar{q}}{\partial z} = 0 \tag{C.3}$$

Appendix D

Estimation of Dissipation Rate α

The parameter α in the linear theory representing the momentum and heat dissipation processes has no counterpart in the numerical CLARK model. Hence, α needs to be determined in order to make consistent evaluation of the linear theory against the numerical simulation.

Equation (3.14) for buoyancy b in the stochastic linear theory is written as

$$\frac{\partial b}{\partial t} + u_0 \frac{\partial b}{\partial x} + N^2 w = Q(x, y, z, t) - \alpha b \tag{D.1}$$

which reduces to a simpler form for neutral atmosphere ($N = 0$), zero synoptic wind ($u_0 = 0$), and night-time ($Q = 0$),

$$\frac{\partial b}{\partial t} = -\alpha b \tag{D.2}$$

The variance of potential temperature θ, σ_θ^2, satisfies the following equation,

$$\frac{\partial \sigma_\theta^2}{\partial t} = -2\alpha \sigma_\theta^2 \tag{D.3}$$

leading to a solution for α

$$\alpha = \frac{1}{t - t_0} \ln \frac{\sigma_\theta(z, t_0)}{\sigma_\theta(z, t)} \tag{D.4}$$

where t_0 is the starting time when Q vanishes.

Figure 4-15 shows σ_θ vs t at different vertical levels. In general, α decreases upward. The

value of α based on Figure 4-15 ranges from 2 day^{-1} to 4 day^{-1}. This is equivalent to

$$\alpha = (0.32 \sim 0.64)\frac{2\pi}{T_0} = (0.32 \sim 0.64)\Omega_0 \tag{D.5}$$

We found the value of α does not sensitively depend on the distribution of the land surface heating. The estimated α in this case (Figure 4-5) is smaller than that assumed in the linear theory, i.e. $1.2\Omega_0$. In Figure 4-13, α is taken to be $0.6\Omega_0$.

Appendix E

Approach to the Analytical Solution of Topographically Induced Flow

Denote the Laplace operator by $\mathcal{L}_{t,s}$ where t is the independent variable that the Laplace transform refers to, $\mathcal{L}_{t,s}\{f(t)\} \equiv F(s)$. Then we may express

$$\begin{aligned}
\mathcal{L}_{t,s}\{dZ_u(k_1,k_2;z,t)\} &= \tilde{U}(k_1,k_2;z,s) \\
\mathcal{L}_{t,s}\{dZ_v(k_1,k_2;z,t)\} &= \tilde{V}(k_1,k_2;z,s) \\
\mathcal{L}_{t,s}\{dZ_w(k_1,k_2;z,t)\} &= \tilde{W}(k_1,k_2;z,s) \\
\mathcal{L}_{t,s}\{dZ_b(k_1,k_2;z,t)\} &= \tilde{B}(k_1,k_2;z,s) \\
\mathcal{L}_{t,s}\{dZ_\phi(k_1,k_2;z,t)\} &= \tilde{\Phi}(k_1,k_2;z,s)
\end{aligned}$$

and

$$\begin{aligned}
\mathcal{L}_{z,p}\{\tilde{U}(k_1,k_2;z,s)\} &= U(k_1,k_2;p,s) \\
\mathcal{L}_{z,p}\{\tilde{V}(k_1,k_2;z,s)\} &= V(k_1,k_2;p,s) \\
\mathcal{L}_{z,p}\{\tilde{W}(k_1,k_2;z,s)\} &= W(k_1,k_2;p,s) \\
\mathcal{L}_{z,p}\{\tilde{B}(k_1,k_2;z,s)\} &= B(k_1,k_2;p,s) \\
\mathcal{L}_{z,p}\{\tilde{\Phi}(k_1,k_2;z,s)\} &= \Phi(k_1,k_2;p,s)
\end{aligned}$$

Laplace transforms of Eqs. (5.22) through (5.26) with respect to t lead to

$$
\begin{aligned}
(s+\alpha+ik_1u_0)\tilde{U} - f\tilde{V} &= -ik_1\tilde{\Phi} && \text{(E.1)}\\
(s+\alpha+ik_1u_0)\tilde{V} + f\tilde{U} &= -ik_2\tilde{\Phi} && \text{(E.2)}\\
(s+\alpha+ik_1u_0)\tilde{W} - \tilde{B} &= -\frac{\partial\tilde{\Phi}}{\partial z} && \text{(E.3)}\\
(s+\alpha+ik_1u_0)\tilde{B} + N^2\tilde{W} &= 0 && \text{(E.4)}\\
ik_1\tilde{U} + ik_2\tilde{V} + \frac{\partial\tilde{W}}{\partial z} &= 0 && \text{(E.5)}
\end{aligned}
$$

with the boundary condition

$$
\begin{aligned}
\tilde{W}(0,s) &= \mathcal{L}_{t,s}\{w\mid_{z=0}\} = \frac{ik_1u_0}{s}dZ_h(k_1,k_2) && \text{(E.6)}\\
\lim_{z\to\infty} \mid \tilde{U},\tilde{V},\tilde{W},\tilde{B},\tilde{\Phi} \mid &< \infty && \text{(E.7)}
\end{aligned}
$$

Laplace transforms of Eqs. (E.1) through (E.5) with respect to z result in

$$
\begin{aligned}
(s+\alpha+ik_1u_0)U - fV &= -ik_1\Phi && \text{(E.8)}\\
(s+\alpha+ik_1u_0)V + fU &= -ik_2\Phi && \text{(E.9)}\\
(s+\alpha+ik_1u_0)W - B &= -p\Phi + \tilde{\Phi}(0,s) && \text{(E.10)}\\
(s+\alpha+ik_1u_0)B + N^2W &= 0 && \text{(E.11)}\\
ik_1U + ik_2V + pW &= \tilde{W}(0,s) && \text{(E.12)}
\end{aligned}
$$

where the boundary conditions $\tilde{W}(0,s)$ is given in (E.6).

Performing Laplace transform twice converts the original partial differential Eqs. (5.22) through (5.26) into a set of linear algebraic Eqs. (E.8) - (E.12).

The solution of Eqs. (E.8) through (E.12) is shown as follows

$$
U = \frac{-i\{k_1(s+\alpha+ik_1u_0)+fk_2\}}{(s+\alpha+ik_1u_0)^2+f^2}\Phi \qquad \text{(E.13)}
$$

$$V = \frac{-i\{k_2(s+\alpha+ik_1u_0)-fk_1\}}{(s+\alpha+ik_1u_0)^2+f^2}\Phi \tag{E.14}$$

$$W = \frac{1}{p^2-k^2T^2}\{p\tilde{W}(0,s) - \frac{(s+\alpha+ik_1u_0)k^2}{(s+\alpha+ik_1u_0)^2+f^2}\tilde{\Phi}(0,s)\} \tag{E.15}$$

$$B = \frac{1}{p^2-k^2T^2}\{\frac{k^2N^2}{(s+\alpha+ik_1u_0)^2+f^2}\tilde{\Phi}(0,s) - \frac{N^2}{s+\alpha+ik_1u_0}p\tilde{W}(0,s)\} \tag{E.16}$$

$$\Phi = \frac{1}{p^2-k^2T^2}\{p\tilde{\Phi}(0,s) - \frac{(s+\alpha+ik_1u_0)^2+N^2}{s+\alpha+ik_1u_0}\tilde{W}(0,s)\} \tag{E.17}$$

where

$$T = T(s) = \{\frac{(s+\alpha+ik_1u_0)^2+N^2}{(s+\alpha+ik_1u_0)^2+f^2}\}^{\frac{1}{2}} \tag{E.18}$$

Expression for $\tilde{W}(0,s)$ is given in (E.6). The boundary condition (E.7) leads to

$$\tilde{\Phi}(0,s) = \frac{(s+\alpha+ik_1u_0)^2+f^2}{s+\alpha+ik_1u_0}\frac{T}{k}\tilde{W}(0,s) \tag{E.19}$$

Next we use the inverse Laplace transform twice, $\mathcal{L}_{p,z}^{-1}$ and $\mathcal{L}_{s,t}^{-1}$, on (E.13) - (E.17) to solve for dZ's

$$\begin{aligned}
dZ_u(k_1,k_2;z,t) &= \mathcal{L}_{s,t}^{-1}\{\mathcal{L}_{p,z}^{-1}\{U\}\} \\
dZ_v(k_1,k_2;z,t) &= \mathcal{L}_{s,t}^{-1}\{\mathcal{L}_{p,z}^{-1}\{V\}\} \\
dZ_w(k_1,k_2;z,t) &= \mathcal{L}_{s,t}^{-1}\{\mathcal{L}_{p,z}^{-1}\{W\}\} \\
dZ_b(k_1,k_2;z,t) &= \mathcal{L}_{s,t}^{-1}\{\mathcal{L}_{p,z}^{-1}\{B\}\} \\
dZ_\phi(k_1,k_2;z,t) &= \mathcal{L}_{s,t}^{-1}\{\mathcal{L}_{p,z}^{-1}\{\Phi\}\}
\end{aligned}$$

The inverse Laplace transform $\mathcal{L}_{p,z}^{-1}$ on Eq. (E.13) through (E.17) leads to

$$\begin{aligned}
\tilde{U} &= \mathcal{L}_{p,z}^{-1}\{U\} \\
&= \frac{k_1u_0}{k}\{\frac{k_1(s+\alpha+ik_1u_0)+fk_2}{s(s+\alpha+ik_1u_0)}\}T\mathrm{e}^{-zkT}dZ_h
\end{aligned} \tag{E.20}$$

$$\begin{aligned}\tilde{V} &= \mathcal{L}_{p,z}^{-1}\{V\} \\ &= \frac{k_1 u_0}{k}\{\frac{k_2(s+\alpha+ik_1u_0)-fk_1}{s(s+\alpha+ik_1u_0)}\}T\mathrm{e}^{-zkT}dZ_h \end{aligned} \tag{E.21}$$

$$\begin{aligned}\tilde{W} &= \mathcal{L}_{p,z}^{-1}\{W\} \\ &= \frac{ik_1u_0}{s}\mathrm{e}^{-zkT}dZ_h \end{aligned} \tag{E.22}$$

$$\begin{aligned}\tilde{B} &= \mathcal{L}_{p,z}^{-1}\{B\} \\ &= -\frac{ik_1u_0N^2}{s(s+\alpha+ik_1u_0)}T\mathrm{e}^{-zkT}dZ_h \end{aligned} \tag{E.23}$$

$$\begin{aligned}\tilde{\Phi} &= \mathcal{L}_{p,z}^{-1}\{\Phi\} \\ &= \frac{k_1u_0}{k}\frac{(s+\alpha+ik_1u_0)^2+fk_2}{s(s+\alpha+ik_1u_0)}T\mathrm{e}^{-zkT}dZ_h \end{aligned} \tag{E.24}$$

Using the inverse Laplace transform $\mathcal{L}_{s,t}^{-1}$ on (E.20) - (E.24) results in the functional forms of dZ's shown in section 5.3.3.

Appendix F

Integrals of I_S and I_C

$$
\begin{aligned}
I_s(t,\xi;u_0,\alpha) &= \int_0^t \sin(\xi\tau)\mathrm{e}^{-(\alpha+ik_1u_0)\tau}d\tau \\
&= \frac{1}{2}[\frac{(\xi+k_1u_0)-\mathrm{e}^{-\alpha t}\{(\xi+k_1u_0)\cos(\xi+k_1u_0)t+\alpha\sin(\xi+k_1u_0)t\}}{\alpha^2+(\xi+k_1u_0)^2}+ \\
&\quad \frac{(\xi-k_1u_0)-\mathrm{e}^{-\alpha t}\{(\xi-k_1u_0)\cos(\xi-k_1u_0)t+\alpha\sin(\xi-k_1u_0)t\}}{\alpha^2+(\xi-k_1u_0)^2}]+ \\
&\quad \frac{i}{2}[\frac{\alpha+\mathrm{e}^{-\alpha t}\{(\xi+k_1u_0)\sin(\xi+k_1u_0)t-\alpha\cos(\xi+k_1u_0)t\}}{\alpha^2+(\xi+k_1u_0)^2}- \\
&\quad \frac{\alpha+\mathrm{e}^{-\alpha t}\{(\xi-k_1u_0)\sin(\xi-k_1u_0)t-\alpha\cos(\xi-k_1u_0)t\}}{\alpha^2+(\xi-k_1u_0)^2}]
\end{aligned} \tag{F.1}
$$

$$
\begin{aligned}
I_c(t,\xi;u_0,\alpha) &= \int_0^t \cos(\xi\tau)\mathrm{e}^{-(\alpha+ik_1u_0)\tau}d\tau \\
&= \frac{1}{2}[\frac{\alpha+\mathrm{e}^{-\alpha t}\{(\xi+k_1u_0)\sin(\xi+k_1u_0)t-\alpha\cos(\xi+k_1u_0)t\}}{\alpha^2+(\xi+k_1u_0)^2}+ \\
&\quad \frac{\alpha+\mathrm{e}^{-\alpha t}\{(\xi-k_1u_0)\sin(\xi-k_1u_0)t-\alpha\cos(\xi-k_1u_0)t\}}{\alpha^2+(\xi-k_1u_0)^2}]- \\
&\quad \frac{i}{2}[\frac{(\xi+k_1u_0)-\mathrm{e}^{-\alpha t}\{(\xi+k_1u_0)\cos(\xi+k_1u_0)t+\alpha\sin(\xi+k_1u_0)t\}}{\alpha^2+(\xi+k_1u_0)^2}- \\
&\quad \frac{(\xi-k_1u_0)-\mathrm{e}^{-\alpha t}\{(\xi-k_1u_0)\cos(\xi-k_1u_0)t+\alpha\sin(\xi-k_1u_0)t\}}{\alpha^2+(\xi-k_1u_0)^2}]
\end{aligned} \tag{F.2}
$$

Appendix G

Alternative Expression for $\hat{T}$

Rewrite $\hat{T}^2$ as

$$\hat{T}^2 \equiv \frac{Z_1 Z_2}{Z_3 Z_4} = \frac{\{\alpha + i(k_1 u_0 + N)\}\{\alpha + i(k_1 u_0 - N)\}}{\{\alpha + i(k_1 u_0 + f)\}\{\alpha + i(k_1 u_0 - f)\}} = r\mathrm{e}^{i\beta} \tag{G.1}$$

where

$$Z_1 = \alpha + i(k_1 u_0 + N) \equiv r_1 \mathrm{e}^{i\theta_1} \tag{G.2}$$

$$Z_2 = \alpha + i(k_1 u_0 - N) \equiv r_2 \mathrm{e}^{i\theta_2} \tag{G.3}$$

$$Z_3 = \alpha + i(k_1 u_0 + f) \equiv r_3 \mathrm{e}^{i\theta_3} \tag{G.4}$$

$$Z_4 = \alpha + i(k_1 u_0 - f) \equiv r_4 \mathrm{e}^{i\theta_4} \tag{G.5}$$

In polar coordinate system, r_i and θ_i can be written as, for $k_1 > 0$

$$r_1 = \sqrt{\alpha^2 + (k_1 u_0 + N)^2} \tag{G.6}$$

$$r_2 = \sqrt{\alpha^2 + (k_1 u_0 - N)^2} \tag{G.7}$$

$$r_3 = \sqrt{\alpha^2 + (k_1 u_0 + f)^2} \tag{G.8}$$

$$r_4 = \sqrt{\alpha^2 + (k_1 u_0 - f)^2} \tag{G.9}$$

$$\theta_1 = \arctan\left(\frac{k_1 u_0 + N}{\alpha}\right) \tag{G.10}$$

$$\theta_2 = \arctan(\frac{k_1 u_0 - N}{\alpha}) + \pi\{1 - H(k_1 u_0 - N)\} \quad \text{(G.11)}$$

$$\theta_3 = \arctan(\frac{k_1 u_0 + f}{\alpha}) \quad \text{(G.12)}$$

$$\theta_4 = \arctan(\frac{k_1 u_0 - f}{\alpha}) + \pi\{1 - H(k_1 u_0 - f)\} \quad \text{(G.13)}$$

where $H(x)$ is the Heaveside function whose value is $+1$ for non-negative argument, and -1 for negative argument. Hence, we have

$$\beta = (\theta_1 + \theta_2) - (\theta_3 + \theta_4) \quad \text{(G.14)}$$

$$r = \sqrt{\frac{r_1 r_2}{r_3 r_4}} \quad \text{(G.15)}$$

Bibliography

[1] André, J.-C., P. Bougeault, and J.-P. Goutorbe, 1990: Regional estimates of heat and evaporation fluxes over nonhomogeneous terrain: Examples from the HAPEX-MOBILHY Programme. *Bound.-Layer Meteor.*, **50**, 77 - 108.

[2] Atkinson, B. W., 1981: *Meso-scale Atmospheric Circulations*, Academic Press, 495pp.

[3] Avissar, R., and F. Chen, 1993: Development and analysis of prognostic equations for mesoscale kinetic energy and mesoscale (subgrid-scale) fluxes for large scale atmospheric models. *J. Atmos. Sci.*, **50**, 3751 - 3774.

[4] Avissar, R., and R. A. Pielke, 1989: A parameterization of heterogeneous land-surface for atmospheric numerical models and its impact on regional meteorology. *Mon. Wea. Rev.*, **117**, 2113-2136.

[5] Bannon, P. R., and J. A. Yuhas, 1980: On Mountain Wave Drag over Complex Terrain. *Meteorol. Atmos. Phys.*, **43**, 155 - 162.

[6] Blumen, W., 1965a: A Random Model of Momentum Flux by Mountain Waves. *Geofysiske Publikasjoner*, **XXVI**, No. 2, 1 - 33.

[7] Blumen, W., 1965b: Momentum Flux by Mountain Waves in a Stratified, Rotating Atmosphere. *J. Atmos. Sci.*, **22**, 529 - 534.

[8] Blumen, W., and C. D. McGregor, 1976: Wave Drag by Three-dimensional Mountain Lee-waves in Nonplanar Shear Flow. *Tellus*, **XXVIII**, 287 - 298.

[9] Bretherton, F. P., 1969: Momentum transport by Gravity Waves. *Quart. J. Royal Meteor. Soc.*, **95**, 213 - 243.

[10] Broad, A., 1995: Linear Theory of Momentum Fluxes in 3-D Flows with Turning of the Mean Wind with Height. *Quart. J. Royal Meteor. Soc.*, **121**, 1891 - 1902.

[11] Christakos, G., 1992: *Random Field MOdels in earth Sciences*, Academic Press, 474pp.

[12] Clark, T. L., 1977: A small-scale dynamic model using a terrain-following coordinate transformation. *J. Computational Phys.*, **24**, 186 - 215.

[13] Clark, T. L., and W. D. Hall, 1995: Documentation of the CLARK Anelastic Model Version G2TC36. NCAR, Boulder, Colorado 80307

[14] Conover, J. H., 1964: The Identification and Significance of Orographically Induced Clouds Observed by TIROS Satellits. *J. Appl. Meteor.*, **3**, 226 - 234.

[15] Dalu, G.A., and R. A. Pielke, 1989: An Analytical Study of the Sea Breeze. *J. Atmos. Sci.*, **46**, 1815-1825.

[16] Dalu, G.A., and R. A. Pielke, 1993: Vertical heat fluxes generated by mesoscale atmospheric flow induced by thermal inhomogeneities in the PBL. *J. Atmos. Sci.*, **50**, 919-926.

[17] Dalu, G.A., R. A. Pielke, R. Avissar, M. Baldi, and A. Guerrini, 1991: Linear Impact of Thermal Inhomogeneities on Mesoscale Atmospheric Flow with Zero Synoptic Wind. *Ann. Geophys.*, **9**, 641-647.

[18] Desjardins, R. L., P. H. Schuepp, J. I. MacPherson, and D. J. Buckley, 1984: Land surface measurements from the split window channels of the NOAA 7 Advanced Very High Resolution Radiometer. *J. Geophys. Res.*, **97**, 18,467 - 18475.

[19] Doran, J. C., W J. Shaw, and J. M. Hubbe, 1995: Boundaru Layer Characteristics over Areas of Inhomogeneous Surface Fluxes. *J. Appl. Meteor.*, **34**, 559 - 571.

[20] Eidenshink, J. C., 1992: The 1990 conterminous U.S. AVHRR data set. *Photogrammetric Engineering and Remote Sensing*, **58**, 809 - 813.

[21] Eliassen, A., 1968: On Meso-scale Mountain Waves on the Rotating Earth. *Geofysiske Publikasjoner*, **XXVII**, No.6, 1 - 15.

[22] Eliassen, A., and E. Palm, 1960: On the Transfer of Energy in Stationary Mountain Waves. *Geofysiske Publikasjoner*, **XXII**, No.3, 1 - 23.

[23] Flasse, S., and M. M. Verstraete, 1994: Monitoring the Environment with Vegetation Indices: Comparison of NDVI and GEMI Using AVHRR Data over Africa. in *Vegetation, Modelling and Climate Change Effects*, edited by F. Veroustraete and R. Ceulemans, 107 - 135.

[24] Gill, A. E., 1980: Some simple solutions for heating-induced tropical circulation. *Quart. J. Royal Meteor. Soc.*, **106**, 447 - 462.

[25] Hsu, H. M., 1987: Study of Linear Atmospheric Flow above a Finite Surface Heating. *J. Atmos. Sci.*, **44**, 186 - 199.

[26] Huss, A., and Y. Feliks, 1981: A mesometeorological numerical model of the sea and land breeze involving sea-atmospheric interactions. *Cont. Atmos. Phys.*, **54**, 238 -257.

[27] Jones, W. L., 1967: Propagation of Internal Gravity Waves in Fluids with Shear Flow and Rotation. *J. Fluid Mech.*, **30**, 439 - 448.

[28] Klemp, J. B., and D. K. Lilly, 1980: Mountain waves and momentum fluxes. *Orographic effects in planetary flows*, GARP publication series; no.**23**, 115 - 141.

[29] Li, B. and R. Avissar, 1994: The impact of spatial variability of land-surface characteristics on land-surface heat fluxes. *J. Climate*, **7**, 527 - 537.

[30] Lüthi, D., A. Cress, H. C. Davies, C. Frei, and C. Schär, 1996, *Interannual Variability and Regional Climate Simulations, Theor. Appl. Climatol.*, **53**, 185 - 209.

[31] Lynn, B.H., F. Abramopoulos, and R. Avissar, 1995: Using similarity theory to parameterize mesoscale heat fluxes generated by subgrid-scale landscape discontinuities in GCMs. *J. Climate*, **8**, 932 - 951.

[32] Lynn, B.H., D. Rind, and R. Avissar, 1995: The importance of mesoscale circulations generated by subgrid-scale landscape heterogeneities in general circulation models. *J. Climate*, **8**, 191 - 205.

[33] Mahfouf, J.-F., E. Richard, and P. Mascart, 1987: The influence of soil and vegetation on the development of mesoscale circulations. *J. Climate Appl. Meteor.*, **26**, 1483 - 1495.

[34] Mahrt, L., and M. Ek, 1993: Spatial Variability of Turbulent Fluxes and Roughness Lengths in HAPEX-MOBILHY. *Boundary-Layer Meteorol.*, **65**, 381 - 400.

[35] Mahrer, Y., and R. A. Pielke, 1977: A numerical study of the airflow over irregular terrain. *Cont. Atmos. Phys.*, **50**, 98 -113.

[36] Neelin, J. D., 1988: A simple model for surface stress and low-level flow in the tropical atmosphere driven by prescribed heating. *Quart. J. Royal Meteor. Soc.*, **114**, 747 - 770.

[37] Ookouchi, Y., M. Segal, R. C. Kessler, and R. A. Pielke, 1984: Evaluation of soil moisture effects on the generation and modification of mesoscale circulations. *Mon. Wea. Rev.*, **112**, 2281-2292.

[38] Palmer, T. N., G. J. Shutts, and R. Swinbank, 1986: Alleviation of a Systematic Westerly Bias in General Circulation and Numerical Weather Prediction models through an Orographic Gravity Wave Drag Parameterization. *Quart. J. Royal Meteor. Soc.*, **112**, 1001 - 1039.

[39] Pielke, R. A., 1974: A three-dimensional numerical model of sea breeze over south Florida. *Mon. Wea. Rev.*, **102**, 115-139.

[40] Pielke, R. A., 1984: *Mesoscale Meteorological Modeling*, Academic Press, 612pp.

[41] Pielke, R.A., G. A. Dalu, J. S. Snook, T. J. Lee, and T. G. F. Kittel, 1991: Nonlinear Influence of Mesoscale Land Use on Weather and Climate. *J. Climate*, **4**, 1053 - 1069.

[42] Queney, P., 1948: The Problem of Air Flow over Mountains: a Summary of Theoretical Studies. *Bull. Amer. Meteor. Soc.*, **29**, 16 - 26.

[43] Rabin, R.M., S. Stadler, P. Wetzel, D. J. Stensrud, and M. Gregory, 1990: Observed effects of landscape variability on convective clouds. *Bull. Amer. Meteor. Soc.*, **71**, 272 - 280.

[44] Rotunno, R., 1983: On the Linear Theory of the Land Sea Breeze. *J. Atmos. Sci.*, **40**, 1999-2009.

[45] Sawyer, J. S., 1959: The Introduction of the Effects of Topography into Methods of Numerical Forecasting. *Quart. J. Royal Meteor. Soc.*, **85**, 31 - 43.

[46] Schetzen, M., 1980: *The Volterra and Wiener Theories of Nonlinear Systems*, Krieger, 573pp.

[47] Segal, M., J. F. W. Purdom, J. L. Song, R. A. Pielke, and Y. Mahrer, 1986: Evaluation of cloud shading effects on the generation and modification of mesoscale circulations. *Mon. Wea. Rev.*, **114**, 1201-1212.

[48] Segal, M., R. Avissar, M. C. McCumber, and R. A. Pielke, 1988: Evaluation of Vegetation Effects on the Generation and Modification of Mesoscale Circulations. *J. Atmos. Sci.*, **45**, 2268 - 2286.

[49] Segal, M., W. E. Schreiber, G. Kallos, J. R. Garratt, A. Rodi, J. Weaver, and R. A. Pielke, 1989: The impact of crop areas in Northern Colorado on midsummer mesoscale thermal circulations. *Mon. Wea. Rev.*, **117**, 809-825.

[50] Smith, E. A. et al, 1992: Area-Averaged Surface Fluxes and THeir Time-Space Variability Over the FIFE Experimental Domain. *J. Geophys. Res.*, **97**, 18,599-18,622.

[51] Smith, R. B., 1978: A Measurement of Mountain Drag. *J. Atmos. Sci.*, **35**, 1644 - 1654.

[52] Smith, R. B., 1979: The Influence of Mountains on the Atmosphere. *Advances in Geophysics*, **21**, 87 - 230.

[53] Smith, R. B., 1980: Linear Theory of Stratified Hydrostatic Flow Past an Isolated Mountain. *Tellus*, **32**, 348 - 364.

[54] Smith, R. B., 1989: Hydrostatic Airflow over Mountains. *Advances in Geophysics*, **31**, 1 - 41.

[55] Steyn, D. G., and K. W. Ayotte, 1985: Application of Two-Dimensional Terrain Height Variance Spectra to Mesoscale Modeling. *J. Atmos. Sci.*, **42**, 2884 - 2887.

[56] Stull, R. B., 1988: *An Introduction to Boundary Layer Meteorology*, Kluwer Academic Publishers, 666pp.

[57] Sun, J., and L. Mahrt, 1994: Spatial Distribution of Surface Fluxes Estimated from Remotely Sensed Variables. *J. Appl. Meteor.*, **33**, 1341 - 1353.

[58] Wang, J., R. Bras, and E. A. B. Eltahir, 1996: A Stochastic Linear Theory of Mesoscale Circulation Induced by the Thermal Heterogeneity of the Land Surface. *J. Atmos. Sci.*, **53**, 3349 - 3366.

[59] Xian, Z. and R. A. Pielke, 1991: The effects of width of landmasses on the development of sea breezes. *J. Atmos. Sci.*, **30**, 1280 - 1304.

[60] Yaglom, A.M., 1987: *Correlation Theory of Stationary and Related Random Functions I*, Springer-Verlag, 512pp.

[61] Yan, H., and R. A. Anthes, 1988: The effect of variations in the surface moisture on mesoscale circulations. *Mon. Wea. Rev.*, **116**, 192-208.

[62] Young, G. S., and R. A. Pielke, 1983: Application of Terrain Height Variance Spectra to Mesoscale Modeling. *J. Atmos. Sci.*, **40**, 2555 - 2560.

[63] Young, G. S., R. A. Pielke, and R. C. Kessler, 1984: A Comparison of the Terrain Height Variance Spectra of the Front Range with That of a Hypothetical Mountain. *J. Atmos. Sci.*, **41**, 1249 - 1250.